HARVARD UNIVERSITY
Graduate School of Arts and Sciences

DISSERTATION ACCEPTANCE CERTIFICATE

The undersigned, appointed by the

Department of Physics

have examined a dissertation entitled

Search for massive particles producing all hadronic final states in proton-proton collisions at the LHC with the ATLAS detector

presented by Anthony Badea

candidate for the degree of Doctor of Philosophy and hereby certify that it is worthy of acceptance.

Signature ______________________________

Typed name: Professor John Huth, Chair

Signature ______________________________

Typed name: Professor Matthew Reece

Signature ______________________________

Typed name: Professor Carlos Argüelles-Delgado

Date: July 7, 2023

Search for massive particles producing all hadronic final states in proton-proton collisions at the LHC with the ATLAS detector

a dissertation presented
by
Anthony Badea
to
The Department of Physics

in partial fulfillment of the requirements
for the degree of
Doctor of Philosophy
in the subject of
Physics

Harvard University
Cambridge, Massachusetts
July 2023

Thesis advisor: Professor John Huth Anthony Badea

Search for massive particles producing all hadronic final states in proton-proton collisions at the LHC with the ATLAS detector

Abstract

A search for massive particles giving rise to all hadronic decays to many jets is presented. The analysis selects events that pass a trigger based on the total and leading jet transverse momentum. A data sample of $\sqrt{s} = 13$ TeV proton-proton collisions collected by the ATLAS detector between 2015 and 2018, corresponding to a total integrated luminosity of 140 fb^{-1}, is used for this search. The analysis deploys two techniques – a traditional method that searches for an excess number of jets above a transverse momentum threshold and a new first of it's kind machine learning based mass resonance search. The standard model background is estimated for the jet counting method using data with scale factors derived from simulations, while that of the mass resonance method is entirely derived from data. A simplified R-parity-violating supersymmetric model is considered with a baryon number violating coupling λ''. The observed yields are compatible with those expected from background processes. Results are presented as limits at 95% confidence level on the model-independent cross section and interpreted as exclusion limits on scenarios with pair-production of prompt gluinos that decay via λ'' to six (direct) or ten (cascade) quarks in total. Gluinos with masses up to 1.8 and 2.2 TeV are excluded for the direct and cascade decay models, respectively.

Contents

Listing of figures

Listing of tables

Acknowledgments

This thesis would not have been possible without the help and support of many people. Some of them I had the pleasure to work with, while others came before me but were equally as important. To the ATLAS and LHC collaborations, thank you for the successful building and operation of these experiments. I am honored to have worked with all of you even tangentially and it makes me happy to have contributed in a small way to this effort.

To my advisor John Huth, thank you for being there to guide me through the past four years. The many conversations that we had about the standard model sectors, realities of building a detector, and countless other topics were foundational to my development. Your deep physics and scientific intuition always inspired me and the way you treat people is something I continue to look up to. Beyond physics, you have been there for me as a mentor and friend to talk about life as well as crack a joke or two. Your calmness and wisdom has helped me immeasurably. I hope I've made you proud.

To the New Small Wheel (NSW) community thank you for the rare opportunity to help build and commission a detector. In particular, thank you to the Athens NTU, BB5, and trigger groups for taking me in – Theo Alexopoulos, George Iakovidis, Kostas Ntekas, Spyridon Kompogiannis, Stamatios (Stam) Tzanos, Christos Paraskevopoulos, Polyneikis Tzanis, Giannis Messolongitis, Maria Perganti, Olga Zormpa, Lorne Levinson, Theo Geralis, Verena Outschoorn, and Cooper Wagner among many others. Thank you to Stefanie Zimmermann, who I didn't get the chance to speak with much but who's kindness helped me when I arrived. I moved to Geneva full time in September 2020 in the middle of the pandemic. At the time, the NSW commissioners were one of the few groups allowed onto the CERN campus, indicative of the time pressure the project was under. This was a tense two years during which I spent more time with these people than my family or friends. They became both of those. Special thank you to Stam who I was lucky enough to have as a partner for most of the time, Theo A. who became a day-to-day mentor inside as well as outside of the lab, George I. for the countless words of encouragment, and Lorne for his expertise as well as genuine care for us as individuals.

To the analysis team that made this thesis possible, thank you for working through the many technical challenges of creating and deploying a new technique to search for a difficult experimental signature – William James Fawcett, John Kenneth Anders, Jonathan Bossio, Claire Antel, Pantelis Kontaxakis, Teng Jian Khoo, Anna Sfyrla, Stefano Franchellucci, Lea Halser, Aaron Paul O'Neill, Kehang Bai, Laura Jeanty, and Javier Montejo Berlingen. The many conversations with everybody significantly improved my physics knowledge and skillset. Thank you also to our reviewers Lorenzo Feligioni, Vangelis Kourlitis, Yvonne Ng, Federico Meloni, Julia Gonski, and Evelyn Jean Thomson for the helpful comments. Special thank you to Javier and John Anders who stood tirelessly with me as we developed the methodology, were eager to teach even when I'd message them at 2am, and helped me through some of the hardest times of the degree. Shout out to Stefano Franchelluci for being right there with me as we got over the finish line. Once again, thank you to John Anders for proof reading this thesis.

To the Harvard group of past and present, thank you. Melissa Franklin, Masahiro Morii, Carlos Arguelles, and Matthew Reece thank you for important feedback throughout graduate school that helped guide my decisions. Those of Harvard past include Larry Lee, Brendon Bullard, Ann Wang, Alex Tuna, Anne Fortman, Alexandra Asbah, and Karri DiPetrillo all of whom played significant roles in my study at different points in time. Special thank you to Larry who originally came up with the idea for this thesis and significantly deepend my physics knowledge and Alex for being my onsite technical advisor while working on the NSW. To those of Harvard present including Gustavs Kheris, Simone Francescato, Nathan Felt, Aaron White, Rongkun Wang, Knut Zoch, Alexis Mulski, Kees Benkendorfer, Jerry Ling, Gabe Rabanal, Laura Bruce, Michael Farrington, Xiaohe Jia, and Yao Yin thank you for the many invaluable physics and non-physics conversations.

To my friends and families across the world, thank you for being there with me throughout the last few years it has really meant a lot to me. Hope to see many of you soon.

List of Acronyms and Abbreviations

ATLAS A Toroidal LHC Apparatus

AB Attention Block

BSM Beyond the Standard Model

BEH Brout-Englert-Higgs

CKM Cabibbo-Kobayashi-Maskawa

CSC Cathode Strip Chamber

CTP Central Trigger Processor

CP Charge-Parity

CL Confidence Limit

CERN Conseil Européen pour la Recherche Nucléaire

CR Control Region

CMS Compact Muon Solenoid

CMB Cosmic Microwave Background

DM Dark Matter

DIS deep inelastic scattering

DLL difference log likelihood

DGLAP Dikshitzer-Gribov-Lopatov-Altarelli-Parisi

EM Electromagnetic

ECAL Electromagnetic Calorimeter

EW Electroweak

EWSB Electroweak Symmetry Breaking

EB Embedding Block

FSR Final State Radiation

FCal Forward Calorimeter

GR General Relativity

GSW Glashow-Salam-Weinberg

GRL Good Run List

HEC Hadronic End-cap Calorimeter

HCAL Hadronic Calorimeter

HLT High Level Trigger

HL-LHC High Luminosity Large Hadron Collider

IRC infra-red and collinear

ISR Initial State Radiation

ID Inner Detector

IBL Insertable B-Layer

IP Interaction Point

JCM Jet Counting Method

JER Jet Energy Resolution

JES Jet Energy Scale

JVT Jet Vertex Tagging

LHC Large Hadron Collider

LO Leading Order

lr learning rate

L1 Level-1

L2 Level-2

LAr Liquid Argon

LCW Local Cell Weighting

ML Machine Learning

ME Matrix Element

MM Micromegas

MMTP Micromegas Trigger Processor

MET Missing Transverse Momentum

MDT Monitored Drift Tube

MC Monte Carlo

MS Muon Spectrometer

NN Neural Network

NSW New Small Wheel

NLO Next-to-Leading Order

NNLO Next-to-Next-to-Leading Order

NNLL next-to-next-to-leading-logarithmic

NR Normalization Region

NP Nuissance Parameter

NPV Number of Primary Vertices

PFlow Particle Flow

PDF Parton Distribution Function

pQCD Perturbative-QCD

PD Pixel Detector

PMNS Pontecorvo–Maki–Nakagawa–Sakata

PV Primary Vertices

pp proton-proton

PS Proton Synchrotron

PSB Proton Synchrotron Booster

QED Quantum Electrodynamics

QCD Quantum Chromodynamics

QFT Quantum Field Theory

RF Radio Frequency

RoI Region of Interest

RPC Resistive Plate Chamber

RPV R-parity-violating

SCT Semiconductor Tracker

SR Signal Region

STGC small-strip Thin Gap Chamber

SM Standard Model

SPS Super Proton Synchrotron

SUSY Supersymmetry

TGC Thin Gap Chamber

TileCal Tile Calorimeter

TRT Transition Radiation Tracker

UV Ultraviolet

UE Underlying Event

vev vacuum expectation value

VR Validation Region

1

Introduction

This is a challenging time for particle physics that necessitates new experiments, technologies, and methods to propel us forward. Forty years ago, new discoveries were found every few years and even just five years ago it felt as though breakthroughs were right around the corner. Now a decade after the Higgs was found and hundreds of searches without discovery at the LHC, we find ourselves wondering what the road forward is. There are of course many questions that remain unanswered, the nature of dark matter, matter-antimatter asymmetry, and gauge-hierarchy problem, to name a few, which serve as ongoing motivation. The challenge we face is that so much of model space has already been probed via direct searches that any signal will necessarily be difficult to find.

In light of this, there are several options depending on what scale one believes new physics exists at. Should there be no new physics at any reachable scale, then the right course of action may be to work on interesting properties of known physics, such as the phase transition from free to confined partons, or simply change field altogether to something like cosmology which has become a motivation for many Large Hadron Collider (LHC) searches. More optimistic is that there is new physics that has been missed in the large dataset, in which case exploring hard regions of phase space with new methods is the right line of approach. It could also be the case that with more data, rarer processes may become accessible. If one believes this, then working on detector upgrades to prepare for the High Luminosity LHC makes sense. Lastly, it is also possible that there is new physics that is just outside of the energy range accessible at the LHC, meaning that working on future colliders is the best route to discovery.

Throughout graduate school I've worked on two of these options, focusing on the upgrade to A Toroidal LHC Apparatus (ATLAS)'s muon spectrometer and deploying a new search technique on the already collected data. The later is the focus of this thesis, which presents a search for pair production of massive particles that each decay to all-hadronic final states with many jets. Historically, this was not a major target for the search program because of the focus on signatures with significant amount of Missing Transverse Momentum (MET), which would be indicative of non-interacting particles being produced such as dark matter candidates. Moreover, this signature is notoriously challenging because of the large multijet background and high multiplicity. The specific simplified signal model under consideration is R-parity-violating (RPV) Supersymmetry (SUSY), which challenges a basic assumption of most of the search program that only baryon (B) and lepton (L) number conserving terms should exist. The B violating models are the main focus here, while other analyses target the L violating models. Theoretically, these models also provide remedies for the heirarchy problem depending on the mass spectrum and satisfy one of the Sakharov conditions for baryogenisis that can help answer questions about matter-antimatter asymmetry. For these reasons, the models have progressively become of greater interest, leading to this work.

The dissertation is structured as follows. First, a brief overview of the theoretical motivation for particle physics at large and this thesis in particular is discussed in Chapter 2. Then, the experimental aspects of the LHC, ATLAS, and physics object reconstruction are discussed in Chapters 3-5. Next, Chapters 6-8 describe the analysis performed to search for the experimental signature described in the previous paragraph. Two approaches are utilized, a traditional jet counting method and a new mass resonance method. The later is of great interest since it is the first time on data that a Machine Learning (ML) algorithm is used to perform the previously impossible task of event reconstruction in high multiplicity final states, leading to significantly stronger limits. Moreover, the technique appears to be general enough that the core technology can be used in other scenarios as well. Finally, the analysis results and outlook are discussed in Chapter 9.

Part I

Theory and Motivation

2

Theory

Particle physics has been formulated through theoretical predictions and experimental measurements, yielding an effective theory of nature called the Standard Model (SM). This chapter provides an overview of the SM in Section 2.1 and Beyond the Standard Model (BSM) physics in Section 2.2.

2.1 The Standard Model of Particle Physics

The SM is described in the framework of Quantum Field Theory (QFT), which combines quantum mechanics, special relativity, and classical field theory. The fundamental objects are quantum fields that are defined at all points of spacetime. In contrast to classical fields, these quantum objects take on operator values which can give rise to nontrivial properties.

Much of the theory is based on the ideas of symmetries, or a feature that remains unchanged under some transformation. The SM contains reference frame, gauge invariance, and discrete symmetries. The former is a statement that the laws of physics should be invariant under any choice of reference frame in spacetime. This is encapsulated in the global Poincare symmetry, consisting of translations, rotations, and boosts. The gauge invariance is a statement that the theory contains redundant degrees of freedom. This is manifested as a local internal symmetry from the group

$$\mathrm{SU}(3)_\mathrm{C} \otimes \mathrm{SU}(2)_\mathrm{L} \otimes \mathrm{U}(1)_\mathrm{Y}, \tag{2.1}$$

where C, L, and Y reference the colour, left-handed weak, and hypercharge quantum numbers, respectively. This symmetry group is spontaneously broken via the Higgs mechanism to $\mathrm{SU}(3)_\mathrm{C} \otimes \mathrm{SU}(2)_\mathrm{L} \otimes \mathrm{U}(1)_\mathrm{EM}$, producing the isospin and electric charges in the process. Lastly, discrete symmetries describe non-continous changes such as parity inversion or conservation of particle number.

The gauge symmetries are the fundamental principals that determine the form of the Lagrangian describing the dynamics and kinematics of the quantum fields. For example, a $\mathrm{U}(1)$ symmetry dic-

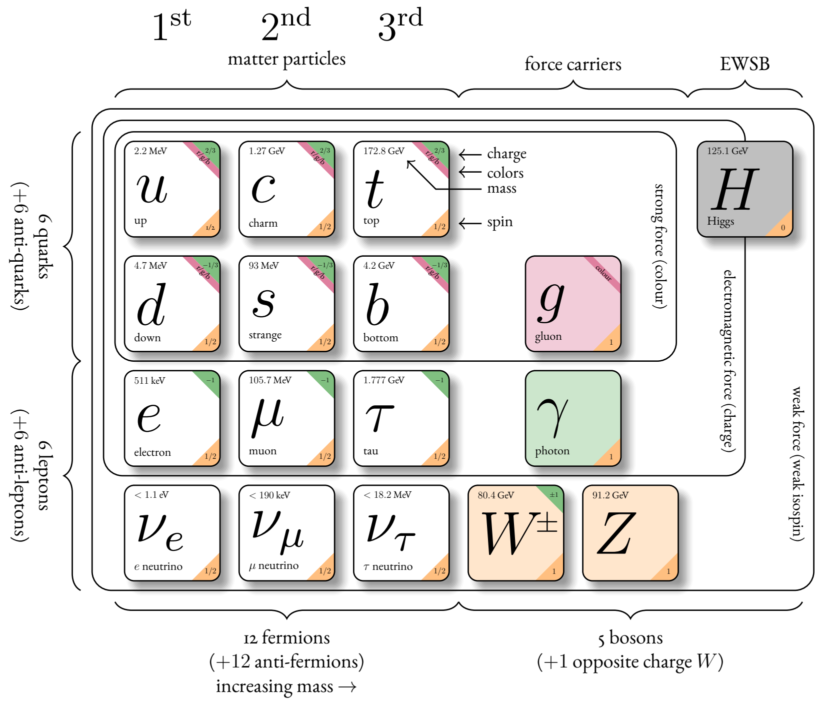

Figure 2.1: The SM particle content comprised of matter particles and force carriers. Template taken from [1] and numbers from [2].

tates that a complex Dirac field should be invariant under the transformation $\psi(x) \to e^{i\alpha(x)}\psi(x)$, where $\alpha(x)$ is an angle that varies point to point in spacetime. The possible products of ψ and its derivatives that are invariant under this transformation gives rise to Langrangian operators of varying mass dimensions. Additional constraints such as renormalizability (mass dimension of four) or discrete symmetries restrict the operators that remain present in the theory.

2.1.1 Particle Content

The SM is comprised of fundamental half and full integer spin particles known as fermions and bosons, respectively, as summarized in Figure 2.1. The particles arise as excitations of the quantum fields underpinning the theory. The fermions interact through the fundamental forces by exchanging or producing integer spin objects known as gauge bosons. These charges arise with conservation laws as dictated by Noether's theorem [3] applied to the gauge symmetries.

Fermions Currently, quarks and leptons exist in three families or generations. The generations have identical quantum numbers except for the later ones are more massive. There are antiparticle copies with opposite electric charge. There are three quarks with electric charge of $+2/3$ known as the up [4, 5], charm [6–8], top [9, 10] and three with $-1/3$ known as the down [4, 5], strange [4, 5], and bottom [11]. The leptons include the electron [12, 13], muon [14], and tau [15] with electric charge of -1 as well as the associated neutrally charged neutrinos [16–18].

Gauge Bosons Gauge bosons mediate the three forces described by the SM and arise from broken continous symmetries as Nambu-Goldstone Bosons [19–21]. The photon mediates the Electromagnetic (EM) force for electrically charged objects. The eight gluons mediate the strong force for objects carrying the colour charge [22]. The $W^{\pm}$ [23, 24] and Z bosons mediate the weak interaction [25, 26].

Higgs Boson The only spin 0 particle in the SM is the Higgs boson, which serves a fundamental role is Electroweak Symmetry Breaking (EWSB) [27–31]. It has no electric or colour charge but is charged under the weak interaction with a hypercharge of 1 and isospin of $-1/2$.

2.1.2 Quantum Electrodynamics

Quantum Electrodynamics (QED) is the relativistic quantum theory of electromagnetism. It describes a collection of electrically charged fermions propagating in free space via a kinematic term and interacting by exchanging a gauge boson, the photon, via a Dirac term. The Langrangian built from gauge invariant terms under the $\mathrm{U}(1)$ symmetry group is

$$\mathcal{L}_{\mathrm{QED}} = \mathcal{L}_{\mathrm{Dirac}} + \mathcal{L}_{\mathrm{Kin.}} = \sum_{f} \bar{\psi}_f \left(i\gamma_\mu D^\mu - m_f \right) \psi_f - \frac{1}{4} F_{\mu\nu} F^{\mu\nu}, \tag{2.2}$$

where the sum over f runs over the generations with mass m_f and spinor ψ_f, $D_\mu = \partial_\mu + ieA_\mu$ is the covariant derivative, $F_{\mu\nu} = \partial_\mu A_\nu - \partial_\nu A_\mu$ is the electromagnetic field strength, and A_μ is the photon field. It can be checked that under the $\mathrm{U}(1)$ symmetry transforming $\psi \to e^{i\alpha}\psi$, the photon field must transform as $A_\mu \to A_\mu - \frac{1}{e}\partial_\mu \alpha$ for the langragian to be invariant. The $\mathrm{U}(1)_{\mathrm{QED}}$ symmetry is not inherent in the SM but rather arises from partial breaking of the SM symmetry group during EWSB.

2.1.3 Quantum Chromodynamics

The strong force or Quantum Chromodynamics (QCD), describes the interactions between colour charged quarks and gluons. QCD is a non-Abelian gauge theory, or a Yang-Mills theory [32], with the symmetry group $\mathrm{SU}(3)_{\mathrm{C}}$. Similar to QED, the lagrangian is composed of Dirac and kinematic terms

$$\mathcal{L}_{\mathrm{QCD}} = \sum_{f} \bar{\psi}_f \left(i\gamma_\mu D^\mu - m_f \right) \psi_f - \frac{1}{4} G^a_{\mu\nu} G_a^{\mu\nu}. \tag{2.3}$$

The sum over f includes the quark fields and ψ_f is a spinor triplet. The colour charges values are referred to as red (r), green (g), or blue (b). Quarks carry colour charge and antiquarks carry anticolour. The covariant derivative

$$D_\mu = \partial_\mu + ig_s T_a A^a_\mu, \tag{2.4}$$

couples the quark field with a coupling strength g via the infinitesimal $\mathrm{SU}(3)$ generators T_a in the fundamental representation via the eight gluon fields $A^a_\mu(x)$. The representation with $T_a = \lambda_a/2$ is often used, where λ_a $(a = 1...8)$ are the Gell-Mann matrices. The gauge invariant gluon field strength, similar to the electromagnetic field strength $F^{\mu\nu}$, is given by

$$G^a_{\mu\nu} = \partial_\mu A^a_\nu - \partial_\nu A^a_\mu + g f^{abc} A^b_\mu A^c_\nu \tag{2.5}$$

where f^{abc} are the structure constants of $\mathrm{SU}(3)$. The non-Abelian nature of $\mathrm{SU}(3)$ corresponding to non-zero values of f^{abc} leads to the characteristic properties of QCD. The m_f and g correspond to quark masses and couplings, which are modified during renormalization. QCD exhibits a few important properties listed below arising from the non-Abelian structure.

Colour confinement [33] The force between two colour charged objects grows linearly with the distance between the objects. Therefore, as the objects are moved further apart the energy needed to maintain the colour connection, or flux tube, grows. At some point it becomes energetically favorable to spontaneously produced a $q\bar{q}$ pair from the vacuum rather than extend the flux tube further. This processes is known as hadronization, where colour objects combine to form colour neutral particles called mesons and baryons. This happens at around a length scale of 1 fm or the QCD scale of $\Lambda_{\mathrm{QCD}} \approx 200$ MeV. In contrast, the electric force of QED drops off like $1/r^2$.

Asymptotic freedom [34, 35] The coupling strength decreases as the energy scale rises

$$\alpha_s\left(Q^2\right) = \frac{12\pi}{\left(22 - 2n_f\right)\ln\left(Q^2/\Lambda_{\mathrm{QCD}}\right)}, \tag{2.6}$$

where $n_f = 6$ is the number of quark flavours, $\Lambda_{\mathrm{QCD}} \sim 0.22$ GeV is a QCD parameter often used as the infrared cutoff scale, and Q^2 is the 4-momentum transfer of the interaction. In contrast, the coupling constant of QED increases with energy since virtual photons and e^+e^- pairs are spontaneously produced by the vacuum. The virtual positrons align closer with the electron since opposite charges attract, *screening* the electric charge. This results in α_{EM} increasing at shorter distances or higher energies, often described as a positive *beta function*

$$\beta(r) = -\frac{de(r)}{d\ln(r)}. \tag{2.7}$$

In QCD, not only are $q\bar{q}$ spontaneously pairs produced but also virtual gluon pairs because of their self coupling. The gluon pairs have the opposite effect known as *antiscreening* and contribute negatively to the beta function. The negative gluon contribution overwhelms the positive $q\bar{q}$ contribution, making the beta function negative and the coupling strength small at short distances or high energies.

Chiral symmetry breaking [20] The spontaneous symmetry breaking of QCD's chiral symmetry which results in hadron masses far above the quark masses.

2.1.4 Electroweak Theory

The weak and electromagnetic interactions are described collectively by the Glashow-Salam-Weinberg (GSW) electroweak model [36–38] with the local gauge-invariant symmetry group

$$\mathrm{SU}(2)_{\mathrm{L}} \otimes \mathrm{U}(1)_{\mathrm{Y}}. \tag{2.8}$$

The weak interactions only couple to left-handed fermions via a vector-axial (V-A) coupling [39–41] with associated charge called the weak isospin I. The third component of the isospin is defined as the conserved charge I_3. The interacting spinors are split into their left and right handed components via projection operators, transforming as an isospin doublet with $I_3 = \pm 1/2$ and single with $I_3 = 0$, respectively. The generator of the $\mathrm{U}(1)_Y$ is the hypercharge Y. The Electroweak (EW) langrangian is

$$\mathcal{L}_{\mathrm{EW}} = \sum_f \bar{\psi}_f \gamma^\mu i D_\mu \psi_f - \frac{1}{4} W_a^{\mu\nu} W_{\mu\nu}^a - \frac{1}{4} B^{\mu\nu} B_{\mu\nu}, \tag{2.9}$$

where the sum over f includes the 2-component Weyl spinors for quarks and leptons, B_μ is the massless gauge field of the $\mathrm{U}(1)_Y$ gauge field, and $W_\mu = \left(W_\mu^0, W_\mu^1, W_\mu^2\right)$ are the massless $\mathrm{SU}(2)_L$ gauge fields. The covariant derivative

$$D_\mu = \partial_\mu + ig^{'}\frac{1}{2}Y_W B_\mu + ig\frac{1}{2}\tau_i^L W_\mu^i \tag{2.10}$$

couples the Weyl fields with a coupling Y_W for the weak hypercharge of the $\mathrm{U}(1)$ and τ_i^L for the pauli matrices of the $\mathrm{SU}(2)$.

2.1.5 Electroweak Symmetry Breaking

The weak interaction predicted the three spin-1 W bosons and was able to regain Fermi's low energy effective theory when the W mass was nonzero. However, this lead to a non-renormalizable theory as can be seen by the low energy limiting behavior of the propagators

- massive propagator $D_{\mu\nu}^{(M)}\left(q^2\right) = -\frac{g_{\mu\nu} - \frac{q_\mu q_\nu}{M_W^2}}{q^2 - M_W^2} \rightarrow \frac{q_\mu q_\nu}{q^2 M_W^2} \rightarrow \frac{\text{const}}{M_W^2} \quad (q^2 \rightarrow \infty)$
- massless propagator $D_{\mu\nu}^{(M=0)}\left(q^2\right) = -\frac{g_{\mu\nu} - \frac{q_\mu q_\nu}{q^2}}{q^2} \rightarrow \frac{\text{const}}{q^2} \quad (q^2 \rightarrow \infty)$

Since the massless propagator asymptotically vanishes, the theory can be renormalized. This problem can be seen a diverent way as a problem with unitarity violating Feynman diagrams. A similar issue with violations of unitarity in $e^+e^- \rightarrow W^+W^-$ was resolved by introducing the Z boson. In this case, $W^+W^- \rightarrow W^+W^-$ violated unitarity at a center-of-mass energy around 1 TeV. The unitarity violating diagrams correspond to the longitudinally polarized W bosons in $W_L W_L \rightarrow W_L W_L$ scattering. The longitudinal polarisation (3rd degree of freedom) only exists for massive particles, whereas massless particles only have two transverse degrees of freedom. These diagrams can be canceled by diagrams involving a scalar particle, which is the Higgs boson. These problems necessitated a solution that could dynamically generate the mass terms for the vector bosons, while preserving the gauge invariance. At the time, spontaneous symmetry breaking had already been used in condensed matter physics to describe the theory of superconductivity. The Higgs mechanism was proposed as an analogous mechanism to break the electroweak symmetry groups, dynamically generate massive vector bosons, and create the low energy behavior of electromagnetism [27–31].

The Higgs component of the SM lagrangian is

$$\mathcal{L}_{\text{Higgs}} = (D_\mu\phi)^\dagger(D^\mu\phi) - V(\phi) = (D_\mu\phi)^\dagger(D^\mu\phi) - \mu^2(\phi^\dagger\phi) - \lambda(\phi^\dagger\phi)^2, \tag{2.11}$$

where ϕ is a $\text{SU}(2)$ doublet of complex scalar fields with $Y = 1$

$$\phi = \begin{pmatrix} \phi^+ \\ \phi^0 \end{pmatrix} = \frac{1}{\sqrt{2}} \begin{pmatrix} \phi_1 + i\phi_2 \\ \phi^3 + i\phi_4 \end{pmatrix}. \tag{2.12}$$

The free parameters μ and λ of the potential $V(\phi)$ are chosen such that $\mu^2 < 0$ and $\lambda > 0$, which creates a potential with infinitely many ground states in the valley satisfying

$$\phi^\dagger\phi = \frac{1}{2}\left(\phi_1^2 + \phi_2^2 + \phi_3^2 + \phi_4^2\right) = -\frac{\mu^2}{\lambda}. \tag{2.13}$$

The field spontaneously chooses a ground state by fixing one of the components. Without loss of generality, that choice is assumed to be $\phi_1 = \phi_2 = \phi_3 = 0$ and $\phi_4 = v$ where $v = \sqrt{-2\mu^2/\lambda}$ is the vacuum expectation value (vev) of the Higgs field. A nonzero vev is consequential for generating masses of all other particles. The Higgs field can then be expanded around this minimum for small deviations $H, \theta_1, \theta_2, \theta_3$ giving

$$\phi(x) = \frac{1}{\sqrt{2}} \begin{pmatrix} \theta_1(x) + i\theta_2(x) \\ v + H(x) + i\theta_3(x) \end{pmatrix} = \frac{1}{\sqrt{2}} \begin{pmatrix} 0 \\ v + H(x) \end{pmatrix} e^{i\frac{\sigma^j \theta_j(x)}{2v}}, \tag{2.14}$$

where the Nambu-Goldstone fields θ_j arising from the broken symmetry are absorbed into the phase factors and then gauged away. Reinserting into the Higgs Lagrangian yields

$$\mathcal{L}_{\text{Higgs}} = \frac{1}{2} (\partial_\mu H)(\partial^\mu H) + \frac{g^2}{4} (v + H)^2 W_\mu^+ W^{\mu -} \tag{2.15}$$

$$+ \frac{1}{8} \frac{g^2}{cos(\theta_W)^2} (v + H)^2 Z_\mu Z^\mu + A_\mu A^\mu \tag{2.16}$$

$$+ \frac{\mu^2}{2} (v + H)^2 - \frac{\lambda}{4} (v + H)^4, \tag{2.17}$$

where many steps have been skipped to show the final result of creating the physical fields $W_\mu^\pm$, Z_μ, H, and A_μ. The W's are created from the fundamental fields via

$$W_\mu^\pm = \frac{1}{\sqrt{2}} \left(W_\mu^1 \mp i W_\mu^2 \right), \tag{2.18}$$

while those of the Z and photon A_μ are created via

$$\begin{pmatrix} Z_\mu \\ A_\mu \end{pmatrix} = \begin{pmatrix} \cos\theta_W & -\sin\theta_W \\ \sin\theta_W & \cos\theta_W \end{pmatrix} \begin{pmatrix} W_\mu^3 \\ B_\mu \end{pmatrix}. \tag{2.19}$$

The generated masses of the gauge bosons are

$$m_W = \frac{vg}{2},\ m_Z = \frac{m_W}{\cos\theta_W},\ m_\gamma = 0,\ m_H = \sqrt{-2\mu^2}. \tag{2.20}$$

Thus, the $\mathrm{SU}(2)$ symmetry that is spontaneously broken by the choice of a vacuum expectation value generates a field excitation that manifests as the Higgs boson with a mass dependent on the kinetic parameter μ. This process allows the guage bosons to start as masssless objects then dynamically acquire mass, protecting renormalizability and correcting the divergent longitudinally polarized diagrams.

The Higgs field also gives rise to the fermion masses through Yukawa mass terms of the kind

$$g_f\bar{\psi}_L\phi\psi_R, \tag{2.21}$$

where g_f is the Yukawa coupling of fermion f and ψ is the corresponding wavefunction. After spontaneous symmetry breaking the ψ field changes such that the term becomes

$$\frac{g_f v}{\sqrt{2}}\bar{\psi}_L\psi_R, \tag{2.22}$$

so that a mass term is generated per fermion as $m_f = \frac{g_f v}{\sqrt{2}}$.

2.1.6 Free SM Lagrangian Parameters

The full SM lagrangian has 26 free parameters already or to be determined experimentally:

- 3 coupling constants of $\mathrm{SU}(3)_C$, $\mathrm{SU}(2)_L$, and $\mathrm{U}(1)_Y$ written as g_s, g, and $g^{'}$

- 12 Yukawa coupling the Higgs boson with the 6 leptons and 6 quarks
- $3+3$ mixing angles and $1+1$ Charge-Parity (CP) violating phase of the Cabibbo-Kobayashi-Maskawa (CKM) and Pontecorvo–Maki–Nakagawa–Sakata (PMNS) matrices
- 2 Higgs potential parameters μ and λ
- 1 QCD vacuum angle θ_{QCD}

Often alternative parameters are used that describe the same physics but in more experimentally accessible ways such as α_{EM}, α_S, the Higgs mass, and the Higgs vacuum expectation value (vev). Putting all of the terms together gives the full lagrangian

$$\mathcal{L}_{\mathrm{SM}} = \mathcal{L}_{\mathrm{QCD}} + \mathcal{L}_{\mathrm{EW}} + \mathcal{L}_{\mathrm{Higgs}} + \mathcal{L}_{\mathrm{Yukawa}} \tag{2.23}$$

$$= -\frac{1}{4}F_{\mu\nu}F^{\mu\nu} + i\bar{\psi}\gamma^{\mu}D_{\mu}\psi + \psi_i y_{ij}\psi_j + |D_{\mu}\psi|^2 - V(\phi) + h.c. \tag{2.24}$$

The first term represents the field strength tensors $W^j_{\mu\nu}$, $B_{\mu\nu}$, and $G^a_{\mu\nu}$. The second term includes the Dirac terms summing over all fermions with the covariant derivative given by

$$D_{\mu} = \partial_{\mu} + igI^j_w W^j_{\mu} + ig^{'}\frac{Y}{2}B_{\mu} + ig_s T^a_C G^a_{\mu}. \tag{2.25}$$

The third term is the Yukawa couplings between the Higgs field and the fermions. The fourth term is the Higgs field kinetic term, followed by the Higgs potential. Finally, the last term includes all of the hermitian conjugates (h.c.) of the earlier terms.

2.2 Beyond the Standard Model

Though the SM is the most complete physical theory in existance, it has shortcomings. There are a number of theoretical questions with the SM itself and observations, mostly astrophysical or cosmological in origin, that are unexplained.

2.2.1 Unexplained Experimental Observations

Dark matter: Astrophysical and cosmological evidence from gravitational effects indicates that about 85% of the matter in the universe and 26% of the energy density is Dark Matter (DM) [42–44]. The SM does not contain a DM candidate and searches for production, scattering, or annihilation processes have come up null [45].

Dark energy: Observations of supernovae, the Cosmic Microwave Background (CMB), large-scale structure, integrated Sachs-Wolfe effects, and observational Hubble constant data indicate that the expansion of the universe is accelerating. From the Friedmann and Einstein field equations, this additional source of energy is necessary to reproduce the experimental observations. This corresponds to roughly 68% of the total energy in the universe being dark energy. Calculations of the SM vacuum fluctuations indicate that they are not large enough to be dark energy [46–50].

Matter-antimatter asymmetry: We observe more matter than anti-matter in the universe. The prominent theoretical explanation is called baryogenesis. The Sakharov conditions posit that for electroweak baryogenesis to have occured in the early universe that there must be baryon number violation, C and

CP violation, and interactions out of thermal equilibrium [51]. The SM does not appear to have enough CP violation to explain the asymmetry [52]. The third condition requires a first order phase transition whereas the SM only contains the smooth EW phase transition [53].

Neutrino masses: The SM only contains massless left handed neutrinos. Oscillation experiments, however, showed that they are nonzero and the absolute mass scale is constrained to < 1.1 eV at 90% Confidence Limit (CL) [54–57]. Neutrino masses can be accomodated in extensions of the SM but the correct additions are not yet known. Furthermore, it is still unknown if they are Majorana or Dirac.

2.2.2 Theoretical Issues

Heirarchy problem (Naturalness): There is a large scale difference between the EW and graviational forces. The Higgs boson is not protected by custodial symmetries in the SM so it receives large quantum corrections proporitional to the square of the Ultraviolet (UV) cutoff scale. If there is no new physics up until the Plank scale of 10^{19} GeV then the Higgs bare mass must be set to cancel many of magnitudes $m_H^2 = m_{H,\mathrm{bare}}^2 + \Delta m_{\mathrm{corr}}^2 - \Delta m_{\mathrm{other}}^2$. This may be only asthetically unpleasant or hint at the need for a deeper theory that explains the scales through dynamical processes [58, 59].

Higgs potential and stability of the universe: The Higgs potential has two free parameters μ and λ. The stability of the vacuum requires that $\lambda > 0$ but μ is not constrained. Furthermore, the shape of the potential is subject to quantum effects that can change its shape at the edges. The most important contributions to these corrections are from the top quark. If the quantum effects are large enough relative to the self-interactions of the Higgs field then the edge of the potential could curl downwards, creating an infinite negative well. The universe may then quantum tunnel to this state, making the overall system unstable [60].

Gravity: The SM cannot make predictions about arbitrarily high energies or curved spacetime geometries. If one posits a massless spin-2 particle then the structure of General Relativity (GR) can be derived from QFT and gravity's universal coupling to matter is apparent [61]. The approach breaks when trying to make predictions about extreme quantum gravitational phenomena, especially at high energies where an infinite number of counterterms are needed to renormalize the theory to all orders.

Strong CP Problem: The QCD lagrangian can contain a CP violating θ term

$$\mathcal{L}_\theta = \frac{\theta_{\mathrm{QCD}} g^2}{32\pi^2} \epsilon^{\mu\nu\alpha\beta} G_{\alpha\beta,a} G^a_{\mu\nu}, \tag{2.26}$$

where $\epsilon^{\mu\nu\alpha\beta}$ is the antisymmetric tensor of rank 4. This term is an example of a Chern-Simons term which has nonperturbative effects depending on the topology of the principal bundle, similar in spirit to the Aharonov-Bohm effect in quantum mechanics. This term leads to a neutron electric dipole moment that depends on the value of the angle and current experimental results require $\theta < O(10^{-10})$. The most prominent solution by Peccei-Quinn introduces a global anomalous symmetry that is spontaneously broken at low energies [62]. This creates a Nambu-Goldstone boson called the axion that forces $\theta = 0$ and thus the theory to be CP-symmetric. The axion has not been observed yet.

SM flavour structure: The Higgs mechanism allows fermion mass terms and the CKM matrix relates the quark masses to the flavor basis. However, neither provide an explanation for the fermion mass heirarchy, the number of generations, the values of the CKM mixing angles or violating phase [63].

2.2.3 R-parity-violating Supersymmetry

SUSY is an extension to the Standard Model (SM) in which a new symmetry between bosons and fermions is introduced, resulting in a new set of particles with masses that could be in reach of LHC energies [64–70]. This additional symmetry and associated particles can help solve problems such as the particle nature of DM, the hierarchy problem related to the mass of the Higgs boson, and others. The new particles, collectively known as sparticles differ in spin by half a unit from their SM counterparts. In exact SUSY the other sparticle quantum numbers are identical to the SM partners, including noteably their masses. However, if SUSY exists then since the sparticles have not been seen, it must be a broken symmetry at the EW scale meaning that the masses m_{SUSY} need not equal m_{SM}.

The gluino $\tilde{g}$ is a fermion and interacts via the strong force as a colour octet. It is a Majorana rather than a Dirac fermion because it is electrically neutral and built from combinations of color-anticolor charges, meaning that it is self-conjugate. There are two primary motivations to search for the $\tilde{g}$. First, the $\tilde{g}$ is predicted to have the largest production cross-section of any SUSY particle at the LHC. Second, naturalness arguments constrain the mass of the $\tilde{g}$, favouring a light $\tilde{g}$ from its two-loop correction to the Higgs boson mass.

The general form of the SUSY Lagrangian leads to processes that violate both baryon number (B) and lepton number (L), leading to rapid proton decay and lepton-number-violating processes, such as unseen decays of $\mu \to e\gamma$ that are in conflict with experimental results. To resolve this the concept

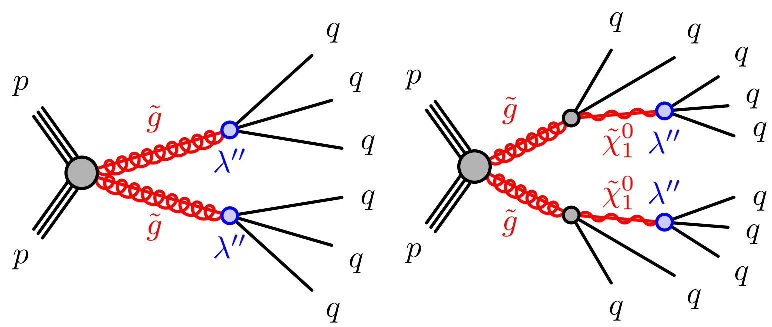

Figure 2.2: Feynman diagrams for pair-produced gluino's decaying to (left) six quarks via RPV $\lambda^{''}$ coupling with an intermediate offshell squark $(\tilde{q})$ and (right) ten quarks through an intermediate neutralino ($\tilde{\chi}_1^0$) which then decays to three quarks via RPV $\lambda^{''}$ coupling.

of R-parity is introduced and defined as $R = (-1)^{3(B-L)+2s}$, where s is the spin of the particle [71–74] . All SM particles have $R = +1$ whereas SUSY particles have $R = -1$. In R-parity-conserving scenarios, this leads to the pair production of SUSY particles (from SM collisions), and ultimately the production of a stable, lightest SUSY particle from the subsequent decays of those initially produced. ATLAS and Compact Muon Solenoid (CMS) have placed stringent limits on these scenarious.

R-parity, however, remains an ad-hoc addition to SUSY and need not be applied as long as the resulting phenomenology does not conflict with experimental results. The RPV component of a generic superpotential can be written as [75, 76]:

$$W_{\text{RPV}} = \frac{1}{2}\lambda_{ijk}L_iL_j\bar{E}_k + \lambda'_{ijk}L_iQ_j\bar{D}_k + \frac{1}{2}\lambda''_{ijk}\bar{U}_i\bar{D}_j\bar{D}_k + \kappa_iL_iH_2, \tag{2.27}$$

where $i, j, k = 1, 2, 3$ are generation indices. The generation indices are omitted in the discussions that follow if the statement being made is not specific to any generation. The first three terms above are often referred to as the trilinear couplings, whereas the last term is referred to as bilinear. The L_i

and Q_i represent the lepton and quark $\mathrm{SU}(2)_\mathrm{L}$ doublet superfields, whereas H_2 represents the Higgs superfield. The $\bar{E}_j$, $\bar{D}_j$, and $\bar{U}_j$ are the charged lepton, down-type quark, and up-type quark $\mathrm{SU}(2)_\mathrm{L}$ singlet superfields, respectively. The couplings for each term are given by λ, λ', and λ'', while κ is a mass parameter.

In the models considered in this thesis, the couplings λ and λ' are set to zero, and only the baryon-number violating coupling λ''_{ijk} is non-zero. The case where only $\lambda''_{ijk} \neq 0$ is often referred to as the "UDD" scenario, as this couples the up-type quark superfield with two down-type quark superfields and gives rise to a two types of scenarios:

- squark decays to two quarks,
- gluino, neutralino, chargino decays to 3 quarks via an off-shell squark.

This thesis is interested in two cases starting with gluino pair production: where the gluino decays to three quarks via an off-shell squark as shown in the left side of Figure 6.1, and where the gluino decays into a pair of quarks and a neutralino, and that neutralino decays via an off-shell squark to three quarks as shown in the right side of Figure 6.1.

In the diagrams above, the off-shell squark is hidden inside of the blue coupling blob. In a full supersymmetric theory the squarks could be offshell but in the simplified model the squarks are decoupled by setting their masses arbitrarily high. This decoupling means that in the phenomological modeling the gluino or neutralino decay directly to quarks, without mention of an intermediate squark. This is important so that the model is sensitive to generic pair-produced heavy particle decay modes. Nevertheless, the squark to quarks decay is interesting from the view of QCD colour flow as shown in

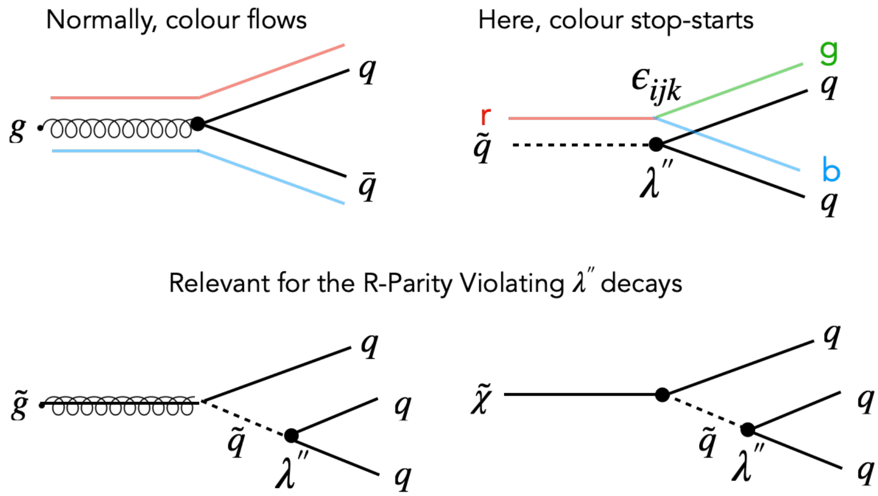

Figure 2.3: Typically colour flows as in the case of a gluon decaying to a $q\bar{q}$ pair (upper left). With the RPV λ'' decay vertex of $\tilde{q} \to qq$, the colour stops and starts via a levi-cevita epsilon symbol (upper right). This is the mediating interaction for both the direct and cascade decays $\tilde{g}/\tilde{\chi} \to q\tilde{q} \to qqq$ of the considered models.

Figure 2.3. The squark and quark are both color triplets, so the decay involves a single colour triplet going to two colour triplets. This means that the colour structure of the vertex is a levi-civita epsilon tensor where colour does not flow but rather stops and starts. This is allowed in QCD but not seen in the SM and can give rise to peculiar decay behavior in the Monte Carlo (MC) generation.

These scenarios are particularly interesting as existing limits from the previous $36.1\ \text{fb}^{-1}$ATLAS search in this channel [77] only limit the cascade model to a gluino mass from 1.0–1.9 TeV while the direct decay model analysis was unable to set limits on the gluino mass beyond the Run 1 limit of around 0.9 TeV. This is in contrast to limits on the gluino mass from R-parity-conserving analyses, which can be as high as 2.3 TeV. Since gluinos are strongly produced, this means that there could be a large number of yet-undiscovered gluinos with mass as light as 1 TeV in the existing ATLAS dataset if they decay as shown in Figure 6.1. For a gluino of mass 1 TeV, the pair-production cross-section at

13 TeV is about 0.385 pb (assuming decoupled squarks), and so with 139 fb^{-1} of data there could be approximately $50,000$ gluinos.

2.2.4 Simplified Models

A model of new physics is defined by a TeV scale effective Langrangian that describes additional particle content and interactions. A simplified model is designed to include only a few new particles and interactions [78]. Often a simplified model is a limiting case of a broader theory, where only one or two particles are accessible at LHC energy scales while the rest are too heavy and thus can be integrated out. Effective field theories offer an alternative but similar probe for new physics where only SM particles are accessible at the LHC energy scale. This introduces effective contact interactions sensitive to new physics, similar to Fermi's 4 point interaction. This thesis uses simplified models so Effective Field Theories are not discussed but Refs. [79–81] provide more details.

2.3 Modelling of proton-proton collisions

The proton is a composite particle known as a baryon that is made of three valence quarks (u, u, d) and a sea of virtual particles, including quarks and gluons, created by vacuum fluctuations. Though its electric and colour charge are produced by the valence quarks, other properties such as its mass are derived from the energy of QCD interactions via gluon exchanges. Since α_S is large at low energies, the proton is a highly nonperturbative object in most regimes of everyday life. The LHC, however, provides high energy proton beams such that the momentum transfer q^2 of the hard scatter is large enough that the system can be treated perturbatively as collisions of the partons.

2.3.1 Factorization

The factorization theorem states that at high energies the proton-proton cross section to a final state f can be decomposed into non-perturbative low energy and high energy hard scatter components [82]

$$d\sigma_{pp\to f}\left(s,\mu_R^2,\mu_F^2\right)=\sum_{i,j}\int_0^1 dx_1\int_0^1 dx_2 f_i\left(x_1,\mu_F^2\right)f_j\left(x_2,\mu_F^2\right)d\hat{\sigma}_{ij\to f}\left(\hat{s},\mu_R^2,\mu_F^2\right). \tag{2.28}$$

The non-perturbative low-energy components of the cross section are described by the Parton Distribution Function (PDF) $f_i\left(x_i,\mu_F^2\right)$. At leading order (LO) the PDF is the probability to find a parton (i) with a fraction x_i, called Bjorken x, of the proton's longitudinal momentum at a given factorization scale μ_F.

The factorization scale is used to separate the soft and hard physics by protecting against divergent IR contributions to the cross section. This factorizes the soft contribution from the PDFs from the hard scatter partonic cross section $d\hat{\sigma}$ that is calculated using Perturbative-QCD (pQCD). The partonic cross section sums over contributions from all partons i and j in the proton. The variable s is the center of mass energy of the collision and $\hat{s}=x_1x_2s$ is the fraction used in the hard scatter. The cross section also depends on the renormalization scale μ_R, which is the scale at which the coupling constants are evaluated at. Often $\mu_R=\mu_F$ is chosen.

The PDFs cannot be calculated from perturbation theory because at low energies α_S is large so they are extracted from measurements. They are assumed to be universal, meaning that once determined

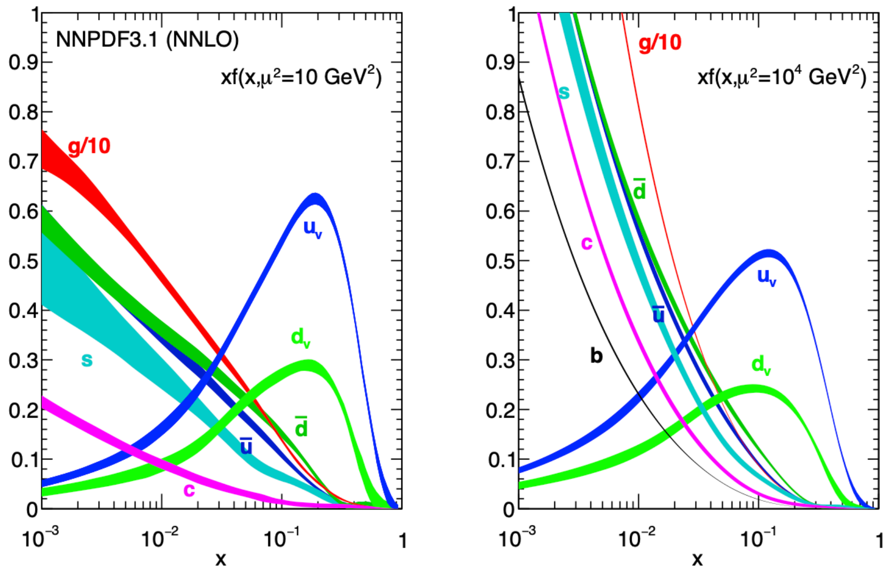

Figure 2.4: Comparison between the NNPDF3.1 NNLO PDFs, evaluated to $\mu^2 = 10$ GeV^2 (left) and $\mu^2 = 10^4$ GeV^2 (right). The individual contributions from the quarks and gluons are shown as differenc colored lines. The valence quark contributions are labeled u_V and d_V [83].

they can be applied to any process. The relevant data for the Bjorken x range for the LHC is taken from deep inelastic scattering (DIS), ep data collected by the H1 and ZEUS collaborations at HERA as well as jet, $t\bar{t}$, and electroweak boson production [83]. An example is shown in Figure 2.4 at two different values of the energy scale q^2. The low q^2 measurements are evolved using the Dikshitzer-Gribov-Lopatov-Altarelli-Parisi (DGLAP) equations to match the high q^2 measurements [83].

2.3.2 Hard Scattering Process

The factorization in Eq. 2.28 can be further understood by expanding the partonic cross section

$$d\sigma_{pp\to f}\left(s,\mu_R^2,\mu_F^2\right)=\sum_{i,j}\int dx_1 dx_2 d\Phi_f f_i\left(x_1,\mu_F^2\right) f_j\left(x_2,\mu_F^2\right)\times\frac{1}{2\hat{s}}\left|M_{ij\to f}\right|^2\left(d\Phi;\mu_F,\mu_R\right), \tag{2.29}$$

where $d\hat{\sigma}$ has been replaced by the associated Matrix Element (ME) and integral over phase space with measure $d\Phi_n$. Similar to the sum of states in Fermi's golden rule, the ME is equal to a sum over of Feynman diagrams $\mathcal{F}_{ij\to f}$

$$M_{ij\to f}=\sum\mathcal{F}_{ij\to f}. \tag{2.30}$$

The ME calculation can be done at various levels of accuracy depending on the order of α_S diagrams included in the sum. Calculations at Leading Order (LO), with a single power of α_S, are readily available by automated generators. Next-to-Leading Order (NLO) are also readily available and used by most analyses. Next-to-Next-to-Leading Order (NNLO) calculations are increasingly available but require significant computational time. Often in analyses, uncertainties are derived from calculating the ME and cross section using different generators as well as varying the μ_R and μ_F scales.

2.3.3 Event Generation

The modeling of proton-proton (pp) collisions is sketched in Figure 2.5. From the incoming protons, partons hard scatter with momentum transfer dictated by the PDFs. The hardest scattering is typically called the primary interaction while others, as well as remenants from the protons, make up

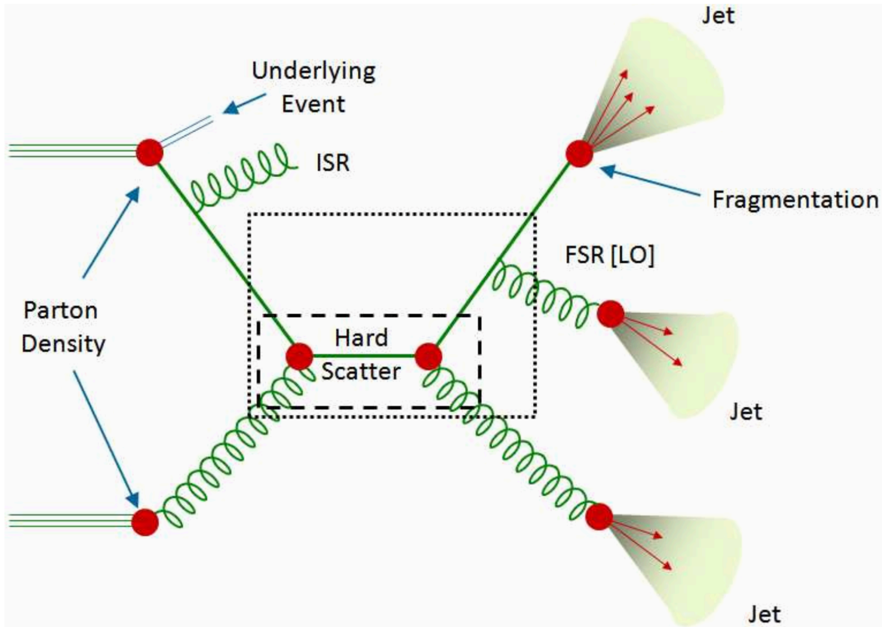

Figure 2.5: Visual representation of a proton-proton collision [84].

the underlying event. The incoming and outgoing partons can radiate addition partons which are called Initial State Radiation (ISR) and Final State Radiation (FSR), respectively. These emissions may be included in the matrix element depending on the order of calculation and factorization scale.

After the hard scatter process, the evolution of the event is modeled by parton shower algorithms. The showering is modeled by energy and angular ordering, with the most energetic emissions happening first. As the showering proceeds, the energy scale drops and α_S grows. Once α_S grows large enough then the perturbative showering stops and hadronization converts the coloured objects into colour neutral hadrons. The hadronization process is modeled using universal fragmentation functions that represent the probability for a parton to hadronize for a given Bjorken x [85]. The fragmentation functions are constrained using data since the process cannot be analytically calculated.

Part II

The Experiment

3

The Large Hadron Collider

The LHC is a 27 km long circular particle accelerator located 100 m underground on the border of Switzerland and France near Geneva. With the LHC, protons are brought to over 99.99% the speed of light and collide at four different points with a peak luminosity of 10^{34} cm^{-2}s^{-1}. This disseration utilizes data from the second data taking period, referred to as Run 2, during which the LHC was operated at a center of mass energy of $\sqrt{s} = 13$ TeV. The peak instantaneous luminosity was 2.1×10^{34} cm^{-2}s^{-1}, delivering 156 fb^{-1} of integrated luminosity to the ATLAS experiment. This chapter begins with a refresher on important aspects of particle colliders in Section 3.1. The LHC design is discussed in Section 3.2 and the operating parameters during Run 2 are given in Section 3.3.

3.1 Accelerator Basics

Accelerators are used to produce ultra-relativistic particle beams and high energy collisions. Using this technology small scale structure can be probed with a spatial resolution given by the De Broglie wavelength $\lambda = \hbar/p$, where $\hbar$ is the Plank constant, and p is the incoming particle momentum. As the collision energy increases, λ decreases and thus smaller lengths can be probed. New high energy physics can also be accessed, such as resonances of hypothetical particles with rest mass ($E = mc^2$) below the collision energy.

In choosing the beam type and collider schematics, the most important consideration is how many events one needs to study the targeted physics. This is given by the product of the integrated luminosity L_{int} and cross section of interest σ_{proc}

$$N_{events} = L_{\text{int}} \times \sigma_{\text{proc}} = \sigma \int L dt, \tag{3.1}$$

where the integrated luminosity is the time integral of the instantaneous luminosity. The cross section has dimensions of area often expressed in units of barn (b) with $1\text{b} = 10^{-24}$ cm^2 and is a measure of the probability a specific type of physical interaction will occur, such as two gluons colliding to produce a Higgs boson. The integrated luminosity has dimensions of inverse area and the instantaneous luminosity is the number of interactions per unit area per second given by

$$L = \frac{N_b^2 n_b f_{ev} \gamma}{4\pi \sigma_x \sigma_y} F, \tag{3.2}$$

where N_b is the number of protons per bunch, n_b is the number of bunches per beam, f_{ev} is the beam revolution frequency, $\sigma_{x(y)} = \sqrt{\epsilon_x \beta_x}$ is the root mean square of the beam width in the x(y) direction for a given emittance ϵ and transverse displacement β, and F is a correction factor from the geometry of the beam crossing. The β, often referred to as the amplitude function, changes throughout the beam and is denoted as β^* at the interaction point where the beams are the most focused. The major goal of LHC physicists and engineers is to deliver the maximum luminosity to each collision point by changing parameters in this equation and maintaining stable collisions for the longest time possible (typically around 10 hours).

For example, the total production cross section of the Higgs boson at the LHC was measured to be around 50 pb. The peak instantaneous luminosity reached by the LHC in Run 2 was 2.1×10^{34} cm^{2}s^{-1} or 0.021 pb^{-1}s^{-1}. So one expects on average 0.021 pb^{-1}s^{-1} $\times$ 50 pb ~ 1 Higgs boson per second. To increase the Higgs boson rate the luminosity must be driven up or a new machine designed with a higher cross section using perhaps lepton-lepton collisions.

Once the physics objective is understood there are two options for colliding particles – hit two beams head on or a single beam into a fixed target. In the case of beam-beam collisions, the center of mass energy is $\sqrt{s} = 2E_b$, where E_b is the energy of each beam. For fixed target, $\sqrt{s} = \sqrt{2E_b m}$, where m the mass of the target particle. There are use cases for both types of experiments, but to produce the highest energy collisions a beam-beam scheme is ideal.

There are two ways to create head-on collisions, using a linear or circular collider. A first consideration in choosing the design is how large the accelerator would need to be, which is dictated by the acceleration technique. The simplest way to accelerate particles is to use a strong electric field aligned with the particle's direction of motion. The maximum accessible energy is limited by the voltage that can be applied but modern Radio Frequency (RF) cavities help alleviate this problem. In light of new technology, to increase the $\sqrt{s}$ of a linear collider it must be made longer and thus more expensive. Circular colliders, on the other hand, reach high energies by circulating the beam many times within the accelerator. This is accomplished with smaller acceleration regions coupled with powerful magnetic fields to keep the particles in orbit. For example, a linear collider with comparable technology would need to be around 280 km long to reach the same $\sqrt{s}$ as the 27 km circular LHC.

The second consideration is how to control the beam, which is more problematic for circular colliders where magnets are used to keep an accelerating beam at constant radius. The difficulty can be seen from classic equations. The force on a particle of charge q and velocity $\vec{v}$ under a magnetic field $\vec{B}$ is given classically by relating the centripetal force and magnetic component of the Lorentz force

$$\vec{f} = q\vec{v} \times B = m\frac{v^2}{r}. \tag{3.3}$$

When the magnetic field is perpendicular to the particles direction of motion, as is the case with the LHC's dipole magnets, the equation reduces to

$$p = qrB, \tag{3.4}$$

where p is the particle momentum perpendicular to the magnetic field, r is the orbital radius, B is the magnetic field strength, and q is the particle's charge. If one takes the charge $q = q_e = 1$ as for protons and electrons, then the equation can be reformulated to give the beam energy in GeV as a function of the field strength in T and the accelerator radius in km

$$E_{\text{beam}} = 0.3BR. \tag{3.5}$$

If the particle's momentum increases and the orbital radius is to remain fixed, then the magnetic field must increase. This requires ramping the field strength as the particles accelerate. Thus, there is a tradeoff between the desired energy, accelerator radius, and necessary field strength. For the LHC, the radius is roughly 27 km and in Run 2 the single beam energy was increased to 6.5 TeV, requiring roughly 7.5 T magnetic fields.

The third consideration is how much energy a charged particle loses when it accelerates. The total radiated power is given by the Lamor formula in its relativistic form

$$P = \frac{q^2\gamma^4}{6\pi\epsilon_0 c}\left(\dot{\beta}^2 + \frac{\left(\beta \cdot \dot{\beta}\right)^2}{1-\beta^2}\right), \tag{3.6}$$

where $\beta = \frac{v}{c}$ is the ratio of the particle velocity to the speed of light, $\gamma = 1/\sqrt{1-\beta^2}$ is the Lorentz factor, ϵ_0 is the vacuum permittivity, and q is the charge of the particle. The two important limiting cases are for acceleration parallel and perpendicular ($\beta \cdot \dot{\beta} = 0$) to the particles velocity

$$P_{a\|v} = \frac{q^2 a^2}{6\pi\epsilon_0 c^3}\gamma^6 \tag{3.7}$$

$$P_{a\perp v} = \frac{q^2 a^2}{6\pi\epsilon_0 c^3}\gamma^4, \tag{3.8}$$

where $a = \dot{v} = \dot{\beta}c$. The dependence on γ is important as it is related to the particle's mass by $E = \gamma mc^2$. Therefore, in the presence of constant nonzero acceleration the power radiation goes as either m^{-4} or m^{-6}, meaning lighter particles lose more energy. While a linear collider can circumvent this problem by not using constant acceleration, a circular collider cannot because the beam undergoes centripetal acceleration as it traverses the circular path. This means that accelerating electrons inside of a circular collider, where the acceleration is perpendicular, creates more radiation than protons because the bremsstrahlung rate is $(m_p/m_e)^4 \approx 10^{13}$ times greater. This consideration was important for building the LHC and will be for any future collider.

The compositness of the accelerated particles is also important for the available production modes and certainty about the incoming state. Since leptons are fundamental point-like particles, the collision energy is known and there is momentum balance in the longitudinal plane (along the beamline). In contrast, hadrons such as a proton are composite objects made of a sea of quarks and gluons. In high energy collisions, where the DeBroglie wavelength is less than the proton radius of 1 fm, the inner structure of the proton is revealed and these partonic constituents collide head on. The momentum distribution of the partons as a fraction of the proton momentum follows a probability distribution modeling the likelihood of finding a parton with a given momentum known as the PDF. As a result, the incoming momentum and center of mass energy of the hard scatter is not known per collision. Therefore, within some precision, only momentum conservation in the transverse plane is guaranteed since the incoming beams are produced at ultra-relativistic speeds along the beam line. There is also an extensive program for colliding nuclei which has similar considerations as hadron colliders.

The final important point to note is a feature of high luminosity colliders with bunch beam structure and electronics with finite readout latency, such as the LHC and its experiments. It is inevitable that there will be multiple collisions per beam (bunch) crossing and any collision that is not the primary most energetic inelastic collision is known as *pileup*. These processes can appear to the detector to be *in-time* meaning they are from within a single bunch crossing or *out-of-time* when the detector is read out over a time scale longer than the bunch spacing. There are two important quantities characterizing this effect. First is the Number of Primary Vertices (NPV), which is a count of how many hard scattering processes there are in a bunch crossing. The second is the average number of interactions per bunch crossing $\langle\mu\rangle$

$$\langle\mu\rangle = \frac{L\sigma_{\text{inelastic}}}{N_{\text{bunch}} f_{\text{LHC}}}, \tag{3.9}$$

which gives an estimate of how much pileup to expect on average per crossing. The mean number of interactions per bunch crossing, or pileup profile, weighted by the luminosity is shown in Figure 3.1. The average and peak $\langle\mu\rangle$ are 33.7 and 70 interactions per bunch crossing, respectively. Pileup is an extreme challenge for high luminosity collider experiments and often is a driving force for detector

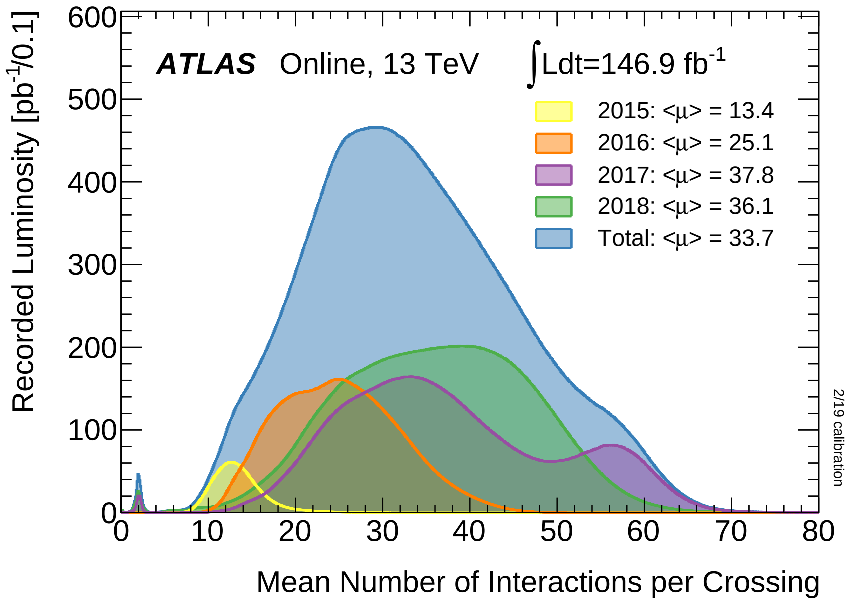

Figure 3.1: The luminosity-weighted distribution of the mean number of interactions per crossing for the 2015 - 2018 pp collision data at 13 TeV centre-of-mass-energy. All data recorded by ATLAS during stable beams is shown and the integrated luminosity and the mean $\langle \mu \rangle$ values are given in the legend [86].

upgrades, such as the New Small Wheel (NSW). To mitigate it, one needs to correctly identify the primary vertex and have strong background rejection from particles originating from pileup.

3.2 Design

The injection chain of the LHC is shown in Figure 3.2, beginning with a bottle of hydrogen located just before Linac 2. First, the hydrogen is exposed to an electric field that strips its electrons, producing protons. Linac 2 then accelerates the protons up to 50 MeV using a sequence of RF cavities. The protons are then transferred into the Proton Synchrotron Booster (PSB), that uses four stacked synchrotron rings to further accelerate the protons to 1.4 GeV before injection into the Proton Syn-

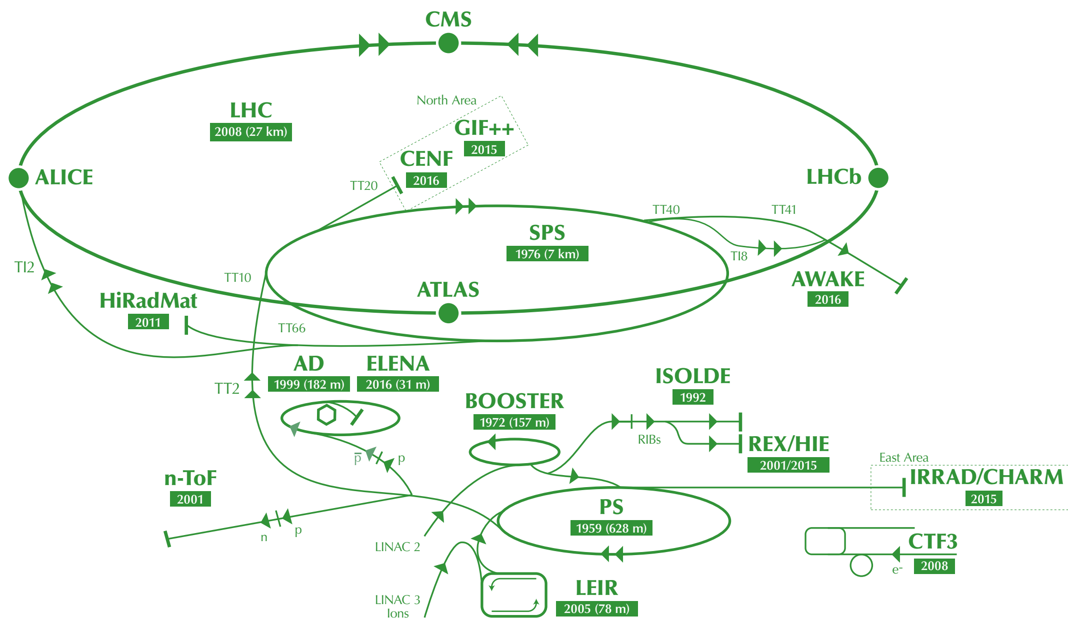

Figure 3.2: The Conseil Européen pour la Recherche Nucléaire (CERN) accelerator complex [87].

chrotron (PS). The PS is composed of 277 iron electromagnets along a 628 m circular path and accelerates the protons up to 25 GeV. The protons are then injected into the Super Proton Synchrotron (SPS), a 7 km long ring that accelerates them up to 450 GeV. Finally, the protons are injected into the 27 km long LHC that accelerates them to 6.5 TeV.

The LHC uses 8 RF cavities to accelerate the beam and 8000 superconducting magnets to control it. Each RF oscillates at 400 MHz and can reach a maximum voltage of 2 Megavolts (MV) with an acceleration gradient of 5 MV/m. With eight RF cavities this corresponds to a maxmium of 16 MV total, thus each circulation around the LHC increases a proton's energy by roughly 16 MeV. The cavities are also able to compensate for the 7 keV of energy lost from synchrotron radiation per beam per revolution. The maximum is achieved after more than 10 million circulations, which is around 20

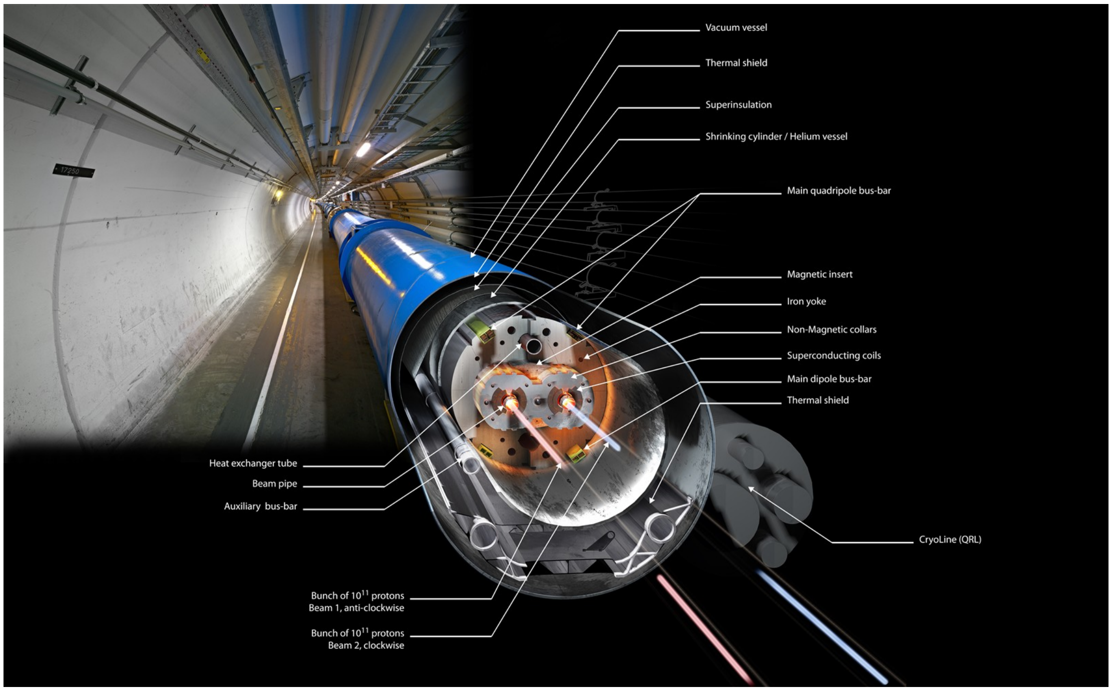

Figure 3.3: A cross section of the LHC dipole magnet within the tunnel [88].

minutes. This processes is known as *ramping*.

The LHC's superconducting magnets are used for focusing and squeezing the beams, correcting trajectories, and damping oscillations in the beam position. They are built from niobium and titanium (NbTi) and cooled to 1.9K by liquid helium based cryogenics systems. Out of the 8000 superconducting magnets, 1232 are dipoles with 8 T fields (12000 Amps of current) that are used to bend the beams and 392 are quadrupoles used to focus them. The remaining roughly 6000 magnets are correctors used to preserve the beam quality. As the energy of the beam increases, the magnets are progressively ramped up in order to keep the orbital radius fixed (as seen in Equation 3.4).

The LHC beam pipe is housed inside a tunnel with diameter 3.7 m. Under this space constraint, the LHC circulates both beams using the same cryostat but seperate magnetic fields and vacuum pipes

Parameter	Design	2015	2016	2017	2018
Energy [TeV]	7.0	6.5	6.5	6.5	6.5
No. of Bunches	2808	2244	2220	$2556 - 1868$	2556
No. of Bunches per Train	288	144	96	$128 - 144$	144
Max. Stored Energy per beam [MJ]	362	280	280	315	312
β^* [cm]	55	80	40	$40 \rightarrow 30$	$30 \rightarrow 27 \rightarrow 25$
Bunch Population N_b [10^{11}p]	1.2	1.1	1.25	1.25	1.1
Typical Normalized Emittance [μm]	3.75	$2.6 - 3.5$	$1.8 - 2$	$1.8 - 2.2$	$1.8 - 2.2$
Peak Luminosity [10^{34}cm^{-2}s-1]	1.0	< 0.6	1.5	2	2.1
Half Crossing Angle [μrad]	142.5	185	$185 \rightarrow 140$	$150 \rightarrow 120$	$150 \rightarrow 130$

Table 3.1: Summary of Run 2 LHC parameters by year compared to the design parameters [90]

per beam. A cross section of a LHC dipole inside of the tunnel is shown in Figure 3.3. A full description can be found in the LHC technical design [89].

The beam itself is not a continuous beam but rather a series of *bunches*, known as *bunch trains* that are tuned using the RF cavities. A single bunch contains roughly 10^{11} protons. The bunches are spaced in time by 25 ns (frequency of 40 MHz), which in meters for a particle traveling at roughly the speed of light is $c \times 25$ ns $= 7.495$ m. Therefore, the the maximum number of bunches in the LHC is roughly 27 km $/7.495$ m ~ 3600. The exact number is slightly larger at 3654 bunches. In practice this number of not achieved and the LHC sets the maximum number of filled bunches to be 2808. During Run 2 the maximum number of filled bunches in was 2556.

3.3 Run 2 Configuration

The LHC configuration parameters most relevant for physics analysis are listed in Table 3.1. Following the first long shutdown prior to 2015, the beam energy was increased from 4 to 6.5 TeV and the bunch spacing was decreased from 50 to 25 ns. To achieve this, the dipole magnets undergo a

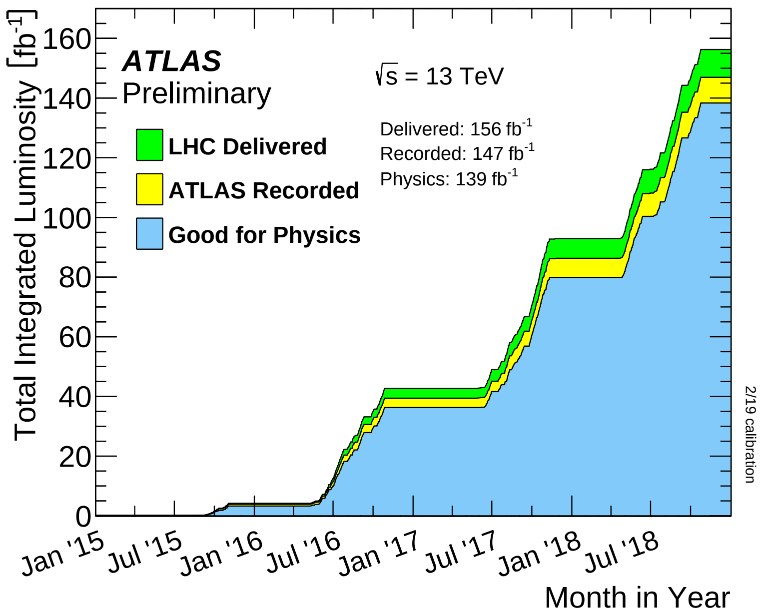

Figure 3.4: Cumulative luminosity versus time delivered to ATLAS (green), recorded by ATLAS (yellow), and certified to be good quality data (blue) during stable beams for pp collisions at 13 TeV centre-of-mass energy in 2015 - 2018 [86].

process known as *training*. During this operation, the current fed to the magnets is ramped up until they quench, then ramped down, and repeated until the desired current is achieved. A by-product of the more extreme beam conditions is that there is more noise in the beam pipe. This happens because negatively charged electrons become more readily liberated from the accelerator walls and attracted to the positively charged beam. In order to reduce this electron cloud a method known as *scrubbing* was used, in which the LHC circulated intense beams with lower energy but more bunches. This removes electrons with high potential to be liberated prior to the primary beam injections.

The total integrated luminosity in units of fb^{-1} per month during Run 2 is show in Figure 3.4. Due to the commissioning challenges from increasing the energy and reducing the bunch spacing, in 2015 only 3.2 fb^{-1} of data was collected. From 2016 - 2018, however, the LHC performance was systematically improved and even surpased design parameters as shown in the yearly columns of Table 3.1. Most notably, the peak instantaneous luminosity was over twice the design value as result of a reduction in β^* and increase in the number of protons per bunch as well as bunches per beam. In fact, the LHC was so performant that ATLAS and CMS had to perform *luminosity leveling* in which the beam crossing angle and space between the beams was altered to reduce the effective cross section, which results in a lower luminosity. The primary hurdle that drove ATLAS to do this was the limited computing power for the High Level Trigger.

The integrated luminosity is measured by ATLAS in two steps. First, the number of pp inelastic collisions is measured online during data taking and offline in reconstruction. This provides a relative measure of the luminosity during data taking. Then, the observed rate is calibrated to an absolute luminosity measurement using Van der Meer scans, in which the beams are systematically moved away from eachother in the x and y directions until the collision rate is zero. Further details of the calibration and measurement can be found in Reference [91]. As shown in Figure 3.4, during Run 2 the LHC delivered 156 fb^{-1} of pp collisions to ATLAS, of which 147 fb^{-1} was recorded and 139 fb^{-1} passed data quality checks for reliable physics data (later re-evaluated to be 140 fb^{-1}).

4

The ATLAS Experiment

The ATLAS experiment is a general purpose cylindrical detector with nearly 4π steradian coverage in solid angle around the Interaction Point (IP). The detector was designed to study proton-proton collisions from the LHC and in particular to find the Higgs boson as well as search for signatures of new physics at the TeV energy scale. The layout is similar to other general purpose detectors with three concentric sub-detector systems. The Inner Detector (ID) sits closest to the IP and makes up

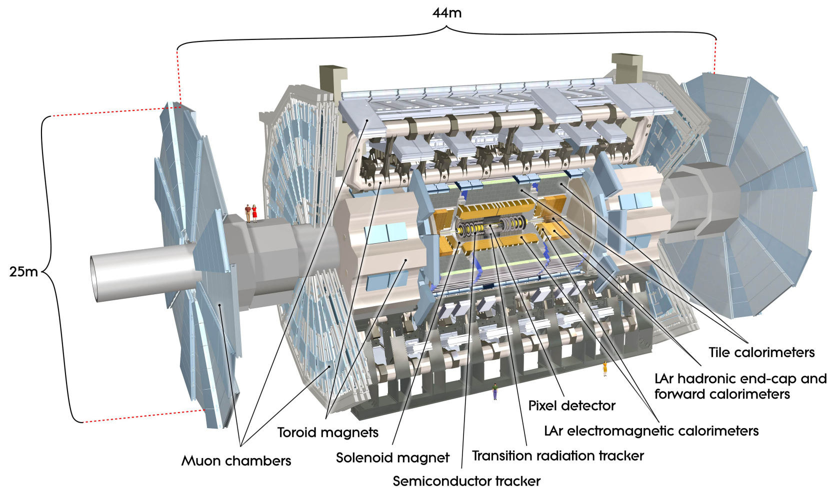

Figure 4.1: The ATLAS detector and its subsystems [92].

part of the tracking subsystem. Then, there is an Electromagnetic Calorimeter (ECAL) and a Hadronic Calorimeter (HCAL), which are used to measure the energy of particles. A solenoid magnet sits within the calorimeters to bend charged particles, enabling precision momentum measurements with the ID. Finally, the Muon Spectrometer (MS) sits on the outermost edges and is the second part of the tracking system, providing an additional precision momentum measurement for muons bent by a dedicated toroidal magnet system. A schematic of ATLAS is shown in Figure 4.3.

This chapter begins by outlining the ATLAS coordinate system in Section 4.1, followed by the physics motivations for the detector design in Section 4.2. The ID is described in Section 4.3, the magnetic field in Section 4.4, the calorimeters in Section 4.5, and the MS in Section 4.6. Further details about ATLAS can be found in Reference [93].

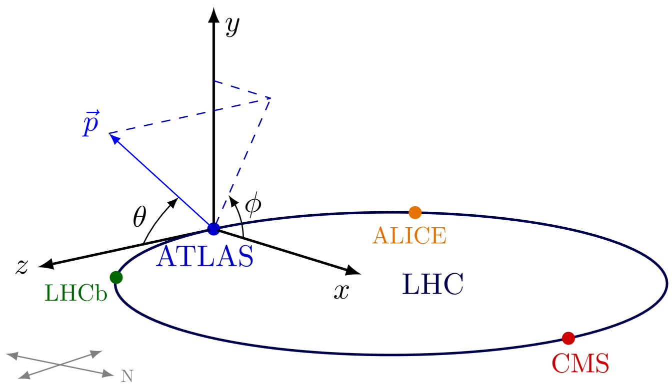

Figure 4.2: The ATLAS coordinate system [94].

4.1 Coordinate System

The nominal IP is defined as the origin of the coordinate system with the beam direction along the z-axis as shown in Figure 4.2. The x-axis is defined to point towards the LHC ring while the y-axis points towards the sky. The A-side of the detector is defined with positive z (closer to the Geneva airport) and the C-side is with negative z (closer to Charlie's Pub in Saint-Genis-Pouilly). The azimuthal angle ϕ is measured around the beam axis and the polar angle θ is the angle from the beam axis. The radial distance R is defined as $R = \sqrt{x^2 + y^2}$.

At a hadron collider the center of mass of the colliding partons is not known. Therefore, transverse variables are used that are invariant under boosts along the z-axis. The rapidity is defined as

$$Y = \frac{1}{2} \ln \frac{E + p_z}{E - pz}, \tag{4.1}$$

where E and p_z are the particle's energy and momentum in the z direction, respectively. 2 key features of rapidity are that differences are lorentz invariant under boosts and particle production is roughly constant as a function of rapidity. At high energies where a massless approximation $E \gg m$ is applicable, the pseudorapidity is often preferred

$$\eta = -\frac{1}{2}\ln\tan\left(\frac{\theta}{2}\right). \tag{4.2}$$

An $\eta = 0$ is equivalent to $\theta = 90^{\circ}$ and $\eta = \infty$ is equivalent to $\theta = 0$. The *barrel* region of ATLAS corresponds to smaller, typically $|\eta| \sim 1 - 1.8$ depending on the subsystem. The *endcap* region measures forward physics at large η values, typically around 1–1.8 to 2.5–3.2 with the exception of the calorimeters which have a forward section from $3.1 < |\eta| < 4.9$. The transverse momentum and energy that are defined as $p_{\mathrm{T}} = \sqrt{p_x^2 + p_y^2}$ and $E_{\mathrm{T}} = E\sin\theta$, respectively, are also often used since the initial transverse distributions are close to zero.

4.2 Physics Motivation

The ATLAS detector was designed with a wide range of physics objectives, but most prominently observing new physics at the TeV scale. In this quest, the Higgs boson had not yet been found and was a major target for the LHC. Consequently, many of the important ATLAS sub-systems were designed to optimize discovery potential over a range of possible production and decay mechanisms depending on the Higgs mass. Furthermore, the detector was designed with the forethought of precisely measuring other SM parameters, such as those relating to the top quark, and searching for BSM physics, such as those arising from SUSY. These objectives were translated into a set of requirements.

- Fast, high granularity, radiation hard electronics and sensors to cope with the experimental conditions of the LHC, involving high particle fluxes from primary interactions and pileup.
- Large acceptance in pseudorapidity and nearly full azimuthal angle coverage.
- Sufficient charged-particle momentum resolution and reconstruction efficiency.
- Vertex detectors close to the IP able to observe secondary vertices of τ-leptons and b-jets.
- ECAL for electron and photon measurements.
- HCAL for jet and MET measurements.
- Muon identification and resolution over a wide range of momentum.
- Strong low p_T trigger efficiency and background rejection.

4.3 Inner Detector

The ID is a tracking detector designed to reconstruct the trajectories of charged particles. It is surrounded by a superconducting solenoid that generates a 2 T magnetic field uniform in the z-direction that bends charged particle trajectories in ϕ. The resulting track's sagitta can be measured, thus giving access to the p_{T}. The system is composed of three sub-detector technologies as shown in Figure 4.4: the Pixel Detector (PD), the Semiconductor Tracker (SCT), and the Transition Radiation Tracker (TRT). The PD is built out of many O(100 μm) pixels and is closest to the IP between $R = 33.25$ – 122.5 mm. Next, the SCT is made from many layers of silicon strips and spans $R = 299$ – 514 mm. Finally, the TRT is composed of straw (drift) tubes and sits from $R = 554$ – 1082 mm.

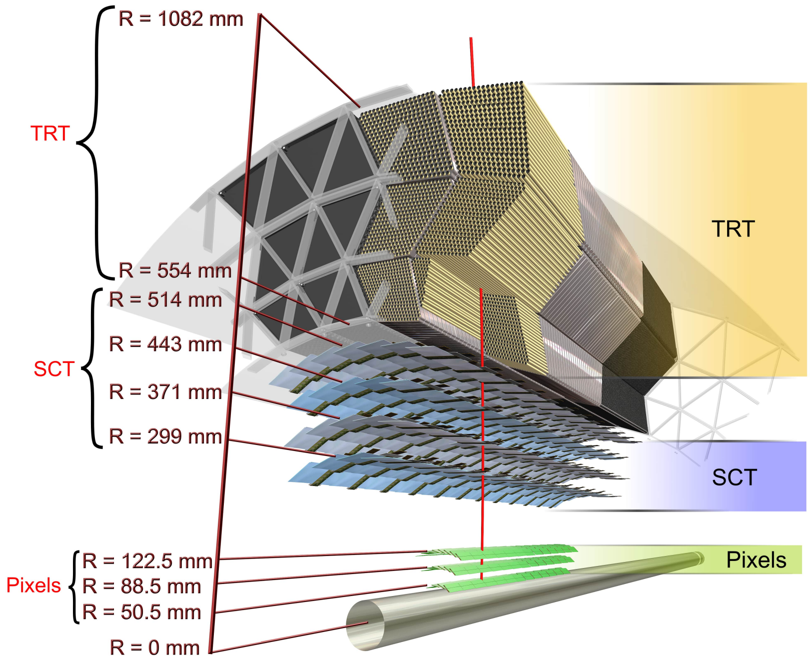

Figure 4.3: A cross-section of the ATLAS Inner Detector [95].

4.3.1 Pixel Detector

In the PD, a minimum ionizing charged particle will traverse and ionize active material to produce around 80 primary electron-hole pairs per micron of silicon [97–99]. If a voltage is applied to the sensor, then the electrons and holes will drift to induce a signal on the electrode. The produced current is read out, amplified, and shaped by front-end electronics, which then extract time and charge measurements of the signal. The basic detector unit is a rectangular pixel module. A module is built out of a sensor (active material) bump-bonded to readout electronics. Each sensor is 250 μm and

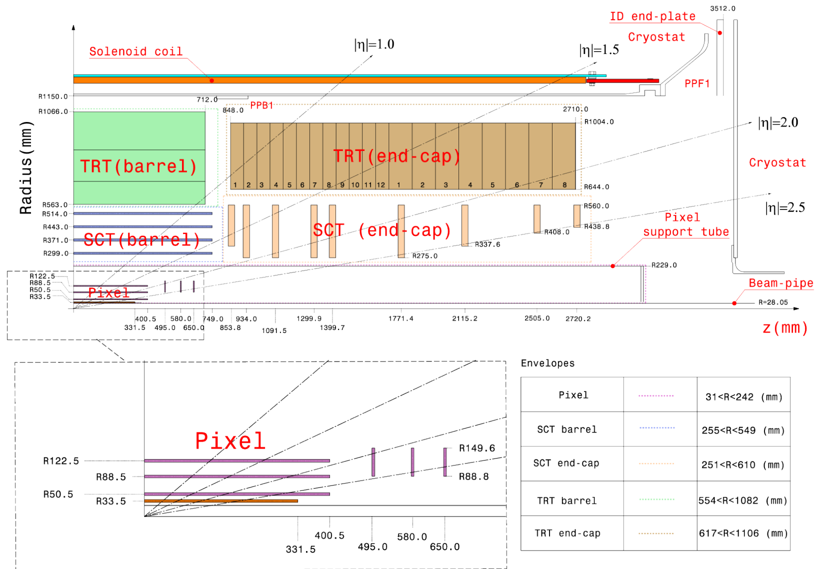

Figure 4.4: A R-z cross-section view of the layout of a quadrant of the ATLAS inner detector for Run 2. The top panel shows the whole inner detector, whereas the bottom-left panel shows a magnified view of the pixel detector region [96].

uses oxygenated n-type bulk. The readout pixels have n^+ implants with p–n junction on the other side. Almost all individual pixels span only 50 μm in r–ϕ and 400 μm in r–z, providing precise three-dimensional spatial measurements.

A schematic drawing of the PD is shown in Figure 4.5. The detector is built from three concentric barrel layers and 2 end-caps with three discs each. The single detector modules are mounted on carbon fiber support structures with incorporated cooling circuits. There are four concentric layers of pixels in the barrel. The Insertable B-Layer (IBL) is the innermost layer and was installed just before the start of Run 2. The remaining three layers are original from Run 1 – the B-Layer or Layer-0, Layer-1, and Layer-2. The endcap consists of three disks. The three original layers have 1774 pixel modelules spread out over roughly 67 million electronic readout channels in the barrel and 13 million in the

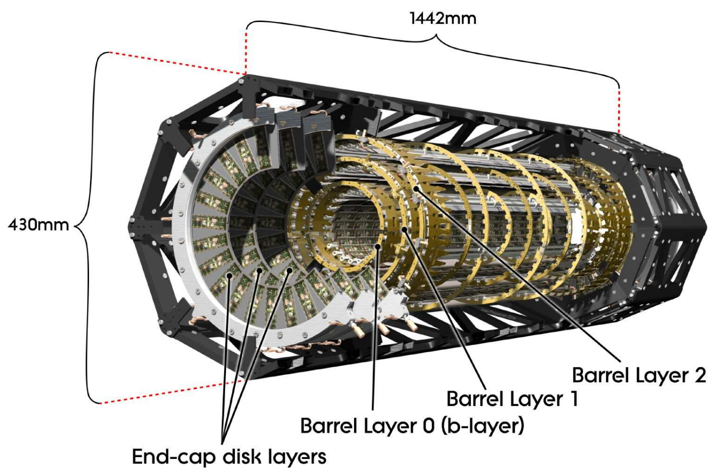

Figure 4.5: A schematic drawing of the ATLAS Pixel Detector. The detector is built out of three concentric barrel layers and three end-cap disks per side [99].

endcap. The pixel spatial resolution is roughly 10 μm in r–ϕ and 115 μm in r–z. The active area is around $1.73\,\mathrm{m}^2$ with coverage up to $|\eta| = 2.5$. There are approximately 67 million electrical channels in the barrel and 13 million in the endcap regions of the detector.

The IBL consists of around 12 million pixels with converage up to $|\eta| = 3$ and active area of 0.15 m^2. In the ϕ direction the system consists of fourteen identical units known as staves, which are each individually composed of 12 planar silicon sensor modules. At the end of each stave there are 3D sensors. The IBL planar pixels have a resolution of 10 μm in r–ϕ and 60 μm in r–z. The detector was installed before Run 2 around a new beam pipe. The new pipe was smaller and thinner than the previously used one, which reduced the amount of material that particles would traverse before reaching the pixel detector. This also allowed the IBL to be positioned closer to the IP, reducing the extrapolation length between the first hit measurement and the impact parameter of a track. These upgrades led to a factor 2 improvement in the impact parameter resolution of tracks. Additionally, the IBL provides radiation shielding for the B-Layer which considerably prolongs its lifetime [100, 101].

4.3.2 Semiconductor Tracker

The SCT is a silicon strip detector consisting of 4 layers in the barrel and 9 disks in each endcap, providing a coverage up to $|\eta| = 2.5$ [102, 103]. Each layer makes a 3d measurement of particles traversing the detector. In total the SCT has roughly 6.3 million readout channels spread out across individual modules and there are 4088 modules per layer.

A SCT module is composed of 2 6.36×6.40 cm^2 silicon sensors. Each sensor is covered with 768 readout strips separated by a pitch size of 80 μm. The sensors are made of 285 μm thick p-in-n type semiconductors and capacitively coupled to the readout strips. Pairs of sensors are wire bonded together to form longer strips. 2 pairs of strips are offset to eachother at an angle of 40 mrad to provide a measure of the precision and non-precision coordinates (a 3d measurement). Each sensor is read out by 6 front-end $ABCD$ chips with 128 binary signal output channels. The endcap r and barrel z resolutions are roughly 580 μm and 17 μm, respecitvely.

4.3.3 Transition Radiation Tracker

The TRT is composed of straw drift tubes and designed to improve charged particle p_{T} resolution up to $|\eta| = 2$ [104, 105]. There are $52,544$ straws in the barrel and $245,760$ in the endcap regions. In the barell the straws point parallel to the beam, while in the endcap they point in the radial direction. The straws are surround by polypropylene and polyethlene fibers that serve as radiator material.

Each straw tube is 4 mm in diameter and made from kapton as well as carbon fiber with a 31 μm diameter gold plated tungsten wire running through the center. The straw wall is a cathode held at 1530 V and the wire is the anode. There is a gas mixture within the tube of 70% xenon or argon, 27% CO_2, and 3% O_2; xenon was replaced by argon in some regions with significant gas leaks for Run 2. As a charged particle traverses the straw, it ionizes the gas within to produces 5 – 6 primary electron-ion pairs. The electrons drift towards the wire while the ions drift away. The electric field grows stronger near the wire so the electrons initiate an avalanche of ionization. This avalanche is characterized by a gas gain, the charge multiplicative factor due to the avalanche, of 2.5×10^4.

Furthermore, a charged particle traversing the TRT also produces transition radiation as it moves across the boundary of the radiation material. Since the radiation spectra depends on the particle's Lorentz factor γ, it can be used to distinguish electrons from other particles.

The straw R–ϕ resolution is 130 μm. There is no information about the η coordinate so the z position is assumed as the center of the straw with a resolution of roughly 42 cm. This corresponds to an R resolution of roughly 10 cm in the endcap. The maximum drift time for electrons is roughly 48 ns, meaning that charge must be integrated over at least 2 bunch crossings to fully capture the ionization radiation. In combination with high pile-up and rate conditions in Run 2, this lead to occupany as high as roughly 90% and significantly lower efficiency. Nevertheless, the TRT is instrumental for fine track momentum resolution by supplying roughly 30 measurements.

4.4 Magnetic Field

The magnetic field is critical to measure the momentum of charged particles [106]. The magnet system is built out of 4 superconducting magnets, including a solenoid, a barrel toroid, and 2 endcap toroids. The solenoid surrounds the ID to bend particles in ϕ and the toroids sit within the MS to bend particles in η. In the ID, the axial magnetic field is roughly 2 T at $z = 0$ and decreases towards the tails of z. In the MS, the field strength varies from 0.15 to 2.5 T in the barrel and 0.2 to 3.5 T in the endcaps. Consequentially, the integrated field strength has considerable $\eta - \phi$ variability.

4.5 Calorimeter

The sampling calorimetry system is divided into an ECAL and HCAL as shown in Figure 4.6, covering a variety of physics and radiation regimes in the range $|\eta| < 4.9$. The calorimeters contain alternating absorber (shower producing) and active material (energy measuring) layers. The name sampling comes from the feature that in the absorber-active alternating scheme some of the particle energy is lost to the absorber and hence only part of the true energy is measured. The ECAL spans $|\eta| < 2.5$ to match the coverage of the ID and is designed with finer granularity for precise electron and photon measurements. The HCAL is designed for jet reconstruction and E_T^{miss} measurements.

In addition to providing coverage for electromagnetic and hadronic showers, the calorimetry system must also limit punch-through to the muon system, i.e. be thick enough that primarily muons make it through to the muon system. The ECAL is > 22 radiation lengths (X_0) thick in the barrel and > 24 in the end-caps. The ECAL, HCAL, and outer support combine to provide over 10 interaction

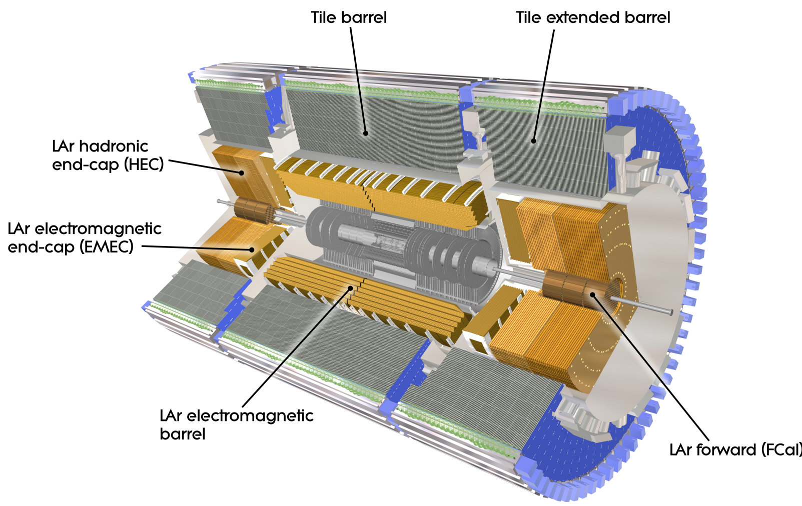

Figure 4.6: A schematic drawing of the ATLAS Calorimeters. The components of the calorimetry system are the Liquid Argon (LAr) Calorimeter and the Tile Hadronic Calorimeter [107].

lengths (λ) of material across the full η range. This is sufficient to reduce punch-through of jets into the muon system and provide a good E_T^{miss} measurement.

The energy resolution of a calorimeter can be parametrized as

$$\frac{\sigma(E)}{E} = \frac{a}{\sqrt{E}} \oplus \frac{b}{E} \oplus c\%, \tag{4.3}$$

where E is the cluster energy, $\sigma(E)$ is the cluster resolution, $\oplus$ indicates a sum in quadrature, a is a stochastic term, b is a electronic noise term, and c is a constant term which includes effects from detector instabilities and mis-calibration. The stochastic term includes fluctuations from the shower detection and larger for sampling calorimeters than homogenous ones.

4.5.1 Liquid Argon Electromagnetic Calorimeter

The Liquid Argon (LAr) ECAL is split into a barrel part $|\eta| < 1.475$ and 2 end-cap pieces $1.375 < |\eta| < 3.2$ [108, 109]. The barrel is built out of 2 identical half-barrels seperated by a gap of 4 mm at $z = 0$. Each end-cap consists of 2 coaxial wheels covering $1.375 < |\eta| < 2.5$ (outer) and $2.5 < |\eta| < 3.2$ (inner). The active material is liquid Argon and the absorbing layers are Lead plates. The plates are arranged in an accordion geometry to provide full coverage in ϕ.

The ECAL is split into regions based on the physics requirements. In the region devoted to precision physics $|\eta| < 2.5$, the detector is split in three sections of varying depth. Meanwhile for $2.5 < |\eta| < 3.2$ corresponding to the end-cap inner wheel, the calorimeter is divided in 2 sections in depth with coarser granularity. There is also a presampler in the region $|\eta| < 1.8$ that helps correct the energy lost by electrons and photons prior to the calorimeter.

The ECAL operates at a nominal voltage of 2000 V, resulting in an average electron drift time of roughly 450 ns to traverse the 2.1 mm gap between the copper electrodes and lead absorber plates. Signals are created by summing adjacent electrodes in a cell or cluster and sampled 5 times every 25 ns. The energy resolution of the ECAL is

$$\frac{\sigma(E)}{E} = \frac{10\%}{\sqrt{E}} \oplus \frac{170\text{ MeV}}{E} \oplus 0.7\%. \tag{4.4}$$

4.5.2 Hadronic Calorimeter

The HCAL is composed of the Tile Calorimeter (TileCal), LAr Hadronic End-cap Calorimeter (HEC), and LAr Forward Calorimeter (FCal). The technologies were chosen to provide adequate energy resolution for the physics objectives as well as cope with the η dependent radiation environment.

The TileCal sits directly outside the ECAL providing barrel coverage up to $|\eta| < 1.7$ and $R = 2.28$ – 4.25m [110]. The detector is built from steel absorbers and scintillating tile active material. The light signals produced by the scintillators are transmitted to 2 photomultiplier tubes via optical fibers.

The LAr HEC consists of 2 wheels per end-cap and sits directly behind the ECAL end-caps. It provides coverage in the range $1.5 < |\eta| < 3.2$, which extents slightly into the TileCal and FCal ranges to increase the material density. Unlike the LAr ECAL, the HEC uses a copper absorber.

The LAr FCal provides coverage from $3.1 < |\eta| < 4.9$ and begins at roughly $z = 4.7$ m. The detector consists of three modules in each end cap, a single copper one that is optimized for electromagnetic measurements and 2 tungsten absorbers designed for hadronic measurements.

The design energy resolutions are given below with the electronic noise term found to be negligble.

$$\text{Barrel} \quad \frac{\sigma(E)}{E} = \frac{50\%}{\sqrt{E}} \oplus 3\% \tag{4.5}$$

$$\text{Endcap} \quad \frac{\sigma(E)}{E} = \frac{100\%}{\sqrt{E}} \oplus 10\% \tag{4.6}$$

4.6 Muon Spectrometer

The MS is designed to provide an additional precision momentum measurement for muons at $|\eta| < 2.7$ that traverse the ID and calorimeters without losing significant energy [111, 112]. The layout is shown in Figure 4.7. Specifically, the calorimeters were designed to stop primary neutral hadrons, photons, charged particles except for muons with $p_{\mathrm{T}} > 3$ GeV and neutrinos. Since muons are produced frequently at the LHC, the MS is an important detector component for precision physics as well as BSM searches. Additionally, it provides a trigger for charged particles up to $|\eta| < 2.4$. The MS is submersed in a toroidal magnetic field and consists of four gaseous detectors built upon distinct technologies – the Monitored Drift Tube (MDT), Cathode Strip Chamber (CSC), Resistive Plate Chamber (RPC), and Thin Gap Chamber (TGC). The MS just underwent an upgrade for Run 3 to replace the Small Wheel with the NSW which deploys small thin gap chambers and micromegas. The MS schematic used for Run 2 is described below.

4.6.1 Monitored Drift Tubes

The MDTs are the primary precision tracking technology in the barrel and large regions of the end-caps. The chambers are built out of pressurized drift tubes. The tubes are filled with Ar/Co_2 gas which causes ionization when a charged particle moves through the chamber. A 50 μm tungsten-rhenium wire runs through the center of each tube with an operating voltage of 3080 V. This wire collects the electrons produced when the gas is ionized. Since the electric field produced by the wire drops off like $1/r^2$, as the electrons drift closer they experience a stronger field which causes an electron avalanche.

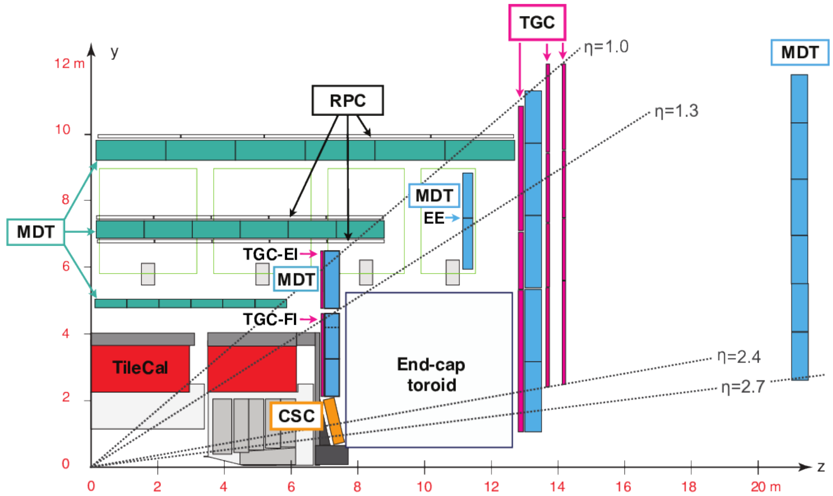

Figure 4.7: A schematic drawing of the ATLAS Muon Spectrometer. A quarter sectino of the muon system is shown in the plane containing the beam axis (y-z plane) [113].

This multiplies the primary charge and amplifies the signal.

4.6.2 Cathode Strip Chambers

The CSCs are multiwire proportional chambers that are able to track at higher particle rates ($\sim$ 1000 Hz/cm^2) than the MDTs ($\sim$ 150 Hz/cm^2). They are used in the high η region where the particle rate is largest.

4.6.3 Resistive Plate Chambers

The RPCs are gaseous electrode-plate detectors (no wires) and make up the trigger system in the barrel region. When an ionizing track traverses the detector, an avalanche is formed from its interaction with the the electric field between the resistive plates. This avalanche then drifts towards capacitively coupled metallic readout strips. The detector could be operated in avalanche mode (described) or an alternative streamer mode. The avalanche mode is used since it is better at handling higher particle rates and rate-independent time resolution.

4.6.4 Thin Gap Chambers

The TGCs are responsible in the end-cap for the muon trigger and determination of the azimuthal coordinate that complements that of the MDTs. The detector is a multi-wire proportional chamber with a shorter wire-to-cathode distance of 1.4 mm than the wire-to-wire distance of 1.8 mm. In combination with a highly quenching gas mixture of CO_2 and n-C_5H_{12}, the TGC was able to provide good time resolution for a majority of the tracks.

4.7 Trigger

In particle physics experiments, a trigger is a system that decides when an interesting event has happened that should be recorded. These systems range in complexity from a simple coincidence between photomultiplier tubes as used in many cosmic ray experiments, to highly sophisticated software and hardware filters utilizing data from many subdectors such as in ATLAS. The need for such a system is directly related to the physics objective. The production modes of particles produced in *pp*collisions follow probability distributions where the most interesting events are often the rarest. To sample this probability distribution, the LHC collides large amounts of protons and produces copeous amounts of data. However, there is not enough storage to save all of the data nor is the collection rate fast enough so the system must decide which events to keep and throw out, eventually saving only around 1% of events. These decisions must happen quickly, in some cases as fast as 2.5 μs, based on the latency

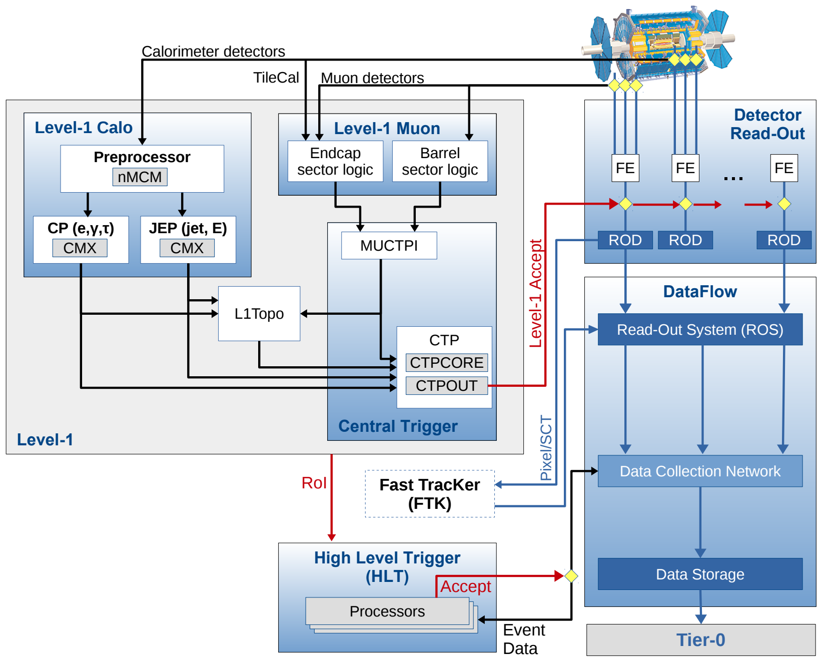

Figure 4.8: The ATLAS TDAQ system in Run 2 showing the components relevant for triggering as well as the detector read-out and data flow [114]. Note that the Fast Tracker (FTK) was not used in Run 2.

of the detector and rate of collisions. There are discussions of how to leverage modern technology to save larger fractions of the data but until then the trigger is a necessary system. The following sections provide an overview of ATLAS's trigger and details about the jet triggers used in this thesis.

The trigger is responsible for processing, selecting, and recording events of interest for physics analysis [114, 115]. The events are selected using a 2-stage system composed of the hardware based Level-1 (L1) trigger and software based High Level Trigger (HLT). These systems reduce the data rate from 40 MHz, or one collision every 25 ns, to a saveable rate of approximately 1 kHz. The primary components and work flow is shown diagramatically in Figure 4.8.

4.7.1 Level-1 Trigger

The L1 trigger is a hardware based filter implemented in custom electronics to use reduced granularity information from the calorimeters and MS. Events are selected based on event-level quantities, multiplicity of objects above thresholds, and topological requirements. The system is composed of the L1 calorimeter (L1Calo) and L1 muon (L1Muon) triggers. Starting at the upper left of Figure 4.8, the L1Calo uses signals from the calorimeters [116]. These signals are first digitized and calibrated by the preprocessor. The processed signals are then sent in parallel to the Cluster Processor (CP) which identifies electrons, photons, and τ-leptons as well as the Jet/Energy-sum Processor (JEP) which identifies jets and calculates sums of total and missing transverse energy. The information from both the CP and JEP are fed into an additional L1 topological (L1Topo) trigger which is able to make decisions based on topological requirements such as invariant masses or angular distances.

The L1Muon trigger uses information from the RPCs in the barrel and TGCs in the endcaps to determine if a candidate track is from a muon produced at the IP [117]. The trigger applies coincidences between the inner and outer TGC stations as well as between the tile calorimeter and the TGCs.

The final L1 trigger decision is made by the Central Trigger Processor (CTP) using signals from the all of the L1Calo, L1Topo and L1Muon (through the L1Muon Central Trigger Processor Interface) triggers. Additional signals are used from other subsystems as well including the Minimum Bias Trigger Scintillators, the LUCID Cherenkov counter, and the zero-degree calorimeter. The CTP is also responsible for limiting the amount of L1 triggers within constraints from the detector read-out latency, known as simple and complex dead time.

The L1 reads data at 40 MHz, accepts events up to a maximum read-out rate of 100 kHz, and makes decisions within a latency of 2.5 μs. Once an event is deemed interesting, the L1 trigger issues a L1 Accept. This signals the ReadOut Drivers (RODs) to perform processing and formatting as well as the ReadOut System (ROS) to buffer the data. This data can then be sent to the HLT if it requests it. The L1 trigger also produces Region of Interest (RoI)'s in η and ϕ to seed the HLT.

4.7.2 High Level Trigger

The HLT is a software based filter that runs on mostly commerically available computers and ne2rk devices. It uses the full granularity data from the calorimeters and MS. First, the Level-2 (L2) trigger is seeded by RoIs, which are detector regions that the L1 trigger has identified as possible trigger objects. The RoI information consists of coordinates, energy, and signature types. The L2 reduces the event rate further down to 3.5 kHz and takes 40 ms per event. Then, the event filter utilizes fully reconstructed events to further refine the trigger selection. In combination, the data rate is reduced down to 1 kHz which amounts to a data write rate of 1.2 GB/s.

Though there are many specialized triggers, this thesis only uses jet triggers and so the remainder of this chapter is devoted to those. More information on the trigger system can be found in [114, 115].

4.7.3 Jet Triggers

A jet trigger is designed to identify events with some interesting number, feature, or characteristic of jets. The types of jet triggers currently availabe are: single-jet that require at least one jet above a p_{T} threshold, multi-jet that requires at least N jets above a p_{T} threshold, H_{T} that require the scalar sum of all jet p_{T} above a threshold, and analysis specific based on individual signatures. This thesis relies on data passing a single-jet L1 trigger and an H_{T} trigger built in the HLT.

4.7.4 Single-Jet L1 Trigger

The L1 trigger uses jets built with a sliding window algorithm on the calorimeter cells. The algorithm identifies RoI's as towers of calorimeter cells whose summed energy exceed a threshold. The energy is calibrated to the EM scale which leads to accurate energy measurements in the ECAL but underestimated deposits in the HCAL. After the calibration, then the triggers place requirements on individual jets. More details can be found in [118].

4.7.5 H_{T} High Level Trigger

The HLT jet triggers are based on jets reconstructed by the anti-k$_t$ algorithm with a radius of $R = 0.4$. These jets are built from calorimeter topo-clusters without any additional information from the tracker. They are then calibrated using a similar method to those used for offline physics analysis. First, a per event pileup subtraction is applied based on jet area and energy density within $|\eta| < 2$. Then, the calorimeter response is corrected via p_{T} and η calibration factors derived from simulation. Finally, the H_{T}, the scale sum of jet p_{T}, is computed and used.

4.8 Phase-1 Upgrade: New Small Wheels

The ATLAS detector is undergoing two phases of upgrades to prepare for the High Luminosity Large Hadron Collider (HL-LHC), where the expected instantaneous luminosity will be roughly 5 –

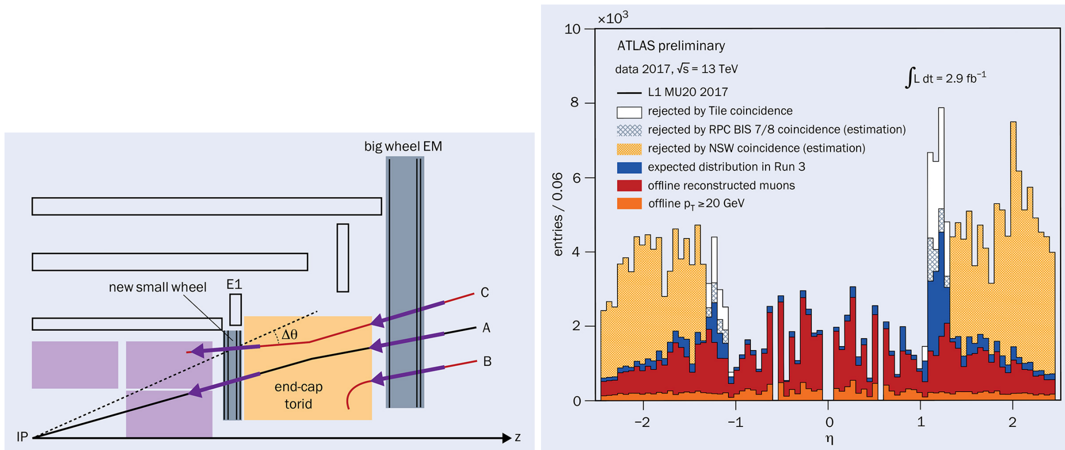

(a) (b)

Figure 4.9: (left) Sketch of a quarter section of ATLAS showing different muon trajectories. Only trajectory A corresponds to a muon produced at the LHC interaction point (IP), while trajectories B and C are from the fake signals that dominate the Level-1 trigger rate. (right) The pseudorapidity distribution of muon candidates passing the level-1 ATLAS trigger with $p_{\mathrm{T}} > 20$ GeV from 2017 Run-2 data, showing the regions expected to be rejected using the NSW in Run 3 and beyond (orange). Almost all triggered muons (blue histogram) are good muons (red). Figures taken from [119].

7 times larger than it is currently. The most significant Phase-1 upgrade is the complete replacement of the MS small wheels with the NSW, a two technology detector comprised of roughly 2.45 million electrical channels. The NSW provides an additional track segment to the L1 trigger from coincidence with the Big Wheels. The segment has roughly 100 μm spatial resolution, 1 mrad polar angle resolution, 15% p_{T} resoluion at 1 TeV, and 1.1 μs trigger latency. This help reject muons that arise from other sources such as cavern backgrounds or the halo of the LHC beam as shown in Figure 4.9a, allowing low p_{T} thresholds to be maintained for the end-cap muons even at the HL-LHC luminosity. The expected rejection regions from including the NSW based on 2017 data taking is shown in Figure 4.9b, making clear the significant impact.

The two technologies used are called the Micromegas (MM) and small-strip Thin Gap Chamber

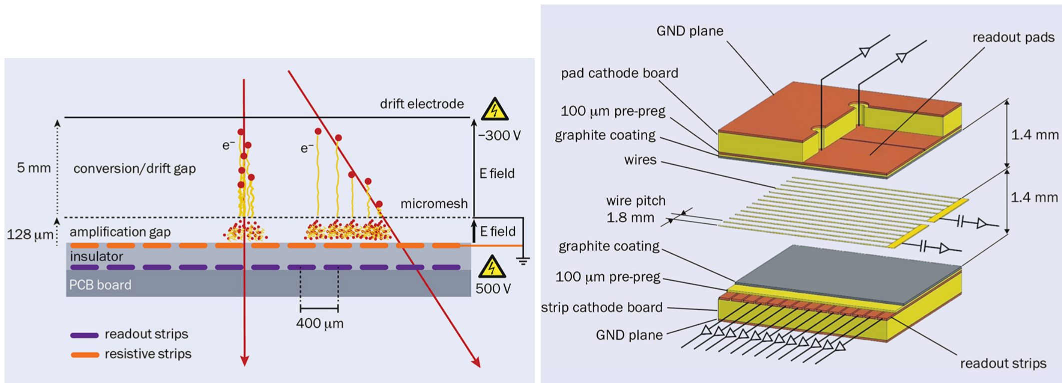

(a) **(b)**

Figure 4.10: Schematic diagrams of the (left) Micromegas and (right) small-strip Thin Gap Chambers that are used within the New Small Wheel. Figures taken from [119].

(STGC). The MM is a parallel plate gaseous detector where gas ionization creates free drift electrons that move in an electric field, pass through a mesh, create an avalanche in the amplification region, and then induce a signal on readout strips. It is primarily used for tracking. Meanwhile, the STGC is a multiwire chamber and the primary trigger detector. The chamber is build with an anode plane located between 2 parallel cathode planes as well as perpendicular strips to wires and pads for triggering. Schematics of both technologies are shown in Figure 4.12. The technologies are stacked together to form sectors, with 32 sectors across the 2 wheels. For futher details see References [119–121].

Though the NSW is not the subject of this thesis, I worked for roughly 2 years on its construction, commissioning, and data taking with a focus on the MM triggering system. My major contributions were validating the electrical and optical connectivity of both wheels with so-called connectivity tests, measuring cosmic ray muons with the Micromegas Trigger Processor (MMTP), and testing the MMTP firmware. The connectivity tests involved using the internal pulser of a front end-chip called the VMM to send test signals to each channel which were then read out through electrical and opti-

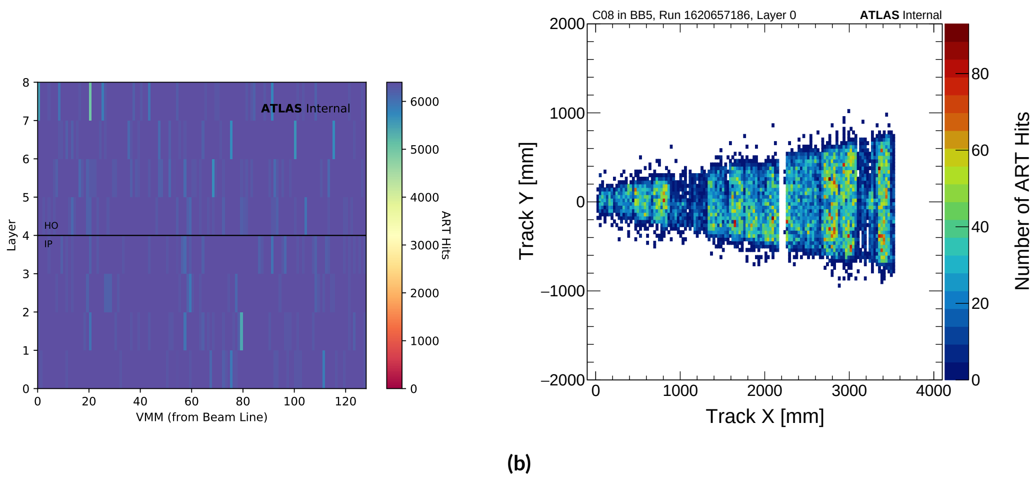

Figure 4.11: (left) Number of track segments recorded by the Micromegas trigger processor after test pulsing, validating the electrical and optical connectivity of a layer. (right) Number of muon candidates recorded by the Micromegas trigger processor while collecting cosmic ray muons in BB5.

cal connections to other boards, ultimately ending at the MMTP. Figure 4.11a shows an example test where 6400 pulses per channel were expected to be read out. The majority of VMM channels were highly efficient and problematic ones were fixed manually. After the connectivity tests, the sectors were used to trigger on cosmic ray muons, enabling real world testing of the MMTP firmware and logic for the first time. Internal coincidence logic within the MMTP decided which track candidates were of interest and sent L1-accepts to record the data. The resulting track profile helped understand the detector and trigger algorithm characteristics as well as its behavior in noisy environments. An example data run is shown Figure 4.11b.

Importantly, the cosmic tests enabled a measurement of the trigger time resolution with the final detector components. The resolution had previously been measured to be roughly 35 ns using a dedicated test stand with pre-production electronics and triggering at threshold as shown in Figure 4.12a.

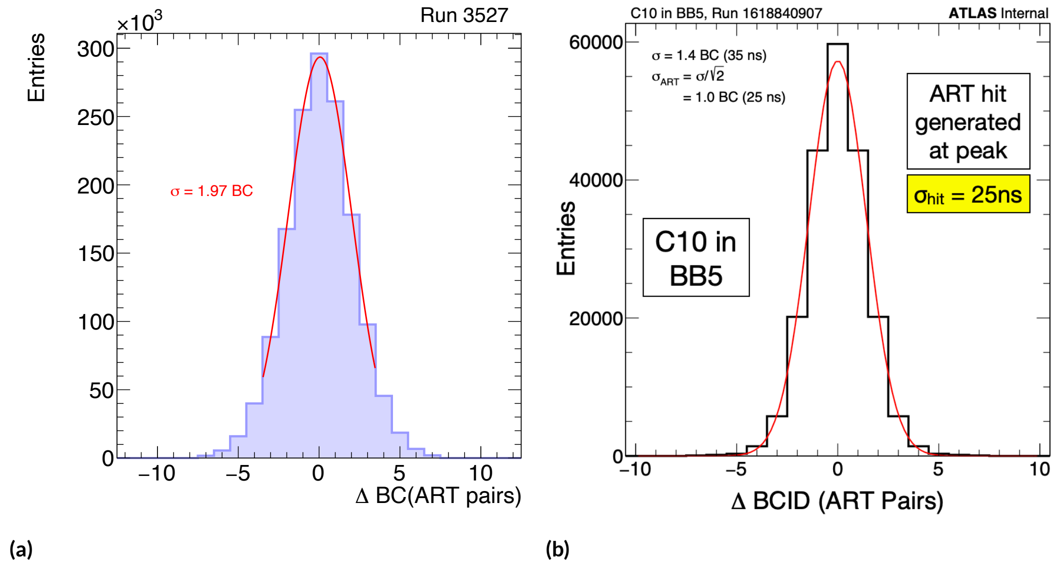

Figure 4.12: (left) Number of track segments recorded by the Micromegas trigger processor after test pulsing, validating the electrical and optical connectivity of a layer. (right) Number of muon candidates recorded by the Micromegas trigger processor while collecting cosmic ray muons in BB5.

The x-axis is the time difference in bunch crossings (BC), or 25 ns intervals, between the first and last hits, referred to as ART pairs for technical reasons not necessary here. Using the delta time resolution extracted from the standard deviation of the gaussian peak, the single hit resolution was measured by summing in quadrature the individual resolutions. The 35 ns resolution was validated using the actual detector, then different configurations were tested to reduce the latency. Most noteably, triggering at peak reduced the resolution to roughly 25 ns as shown in Figure 4.12b, helping reduce the overall trigger latency budget. Reducing the peaking time from 200 to 100 ns also had an impact in narrowing the distribution but those studies are ommitted here. Beyond only the figures shown, the cosmic tests were foundational to understanding the optimal detector configurations that are now used for pp data taking. More details can be found in References [122–125].

5

Reconstruction of Physics Objects

Reconstruction is the procedure of processing raw detector signals to create objects for physics analysis. Though this thesis relies primarily on the reconstruction of jets, it also uses leptons (electrons and muons) and $E_{\mathrm{T}}^{\mathrm{miss}}$ reconstruction in order to veto events. These objects are built and calibrated using measurements from many of ATLAS's subdetectors as discussed below.

5.1 Tracks and Primary Vertices

Track reconstruction converts hits of energy deposits to trajectories of charged particles, referred to as tracks. This section focuses on reconstruction in the ID [126]. This is a complex task because of the high numbers of charged particles produced per event (about 600 in Run 2), large pileup, and quantity of detector readout channels (about 100 million). The input to the reconstruction is 3d points built from clusters in the PD and SCT as well as drift circles in the TRT. Two algorithms are used.

The inside-out algorithm reconstructs charged particles originating from the hard scatter or from the decay of short lived particles. The algorithm is seeded by three hits in the PD and SCT. This seed is combined with information about the magnetic field and detector material within a combinatorial Kalman filter to extrapolate the track to the end of the SCT. At this stage, there may be multiple track candidates arising from ambiguities in the extrapolation. An ambiguity solver then applies quality requirements on the track candidates and ranks them in terms of the quality of the track. Lastly, the remaining tracks are further extended to the TRT and combined with hit measurements.

The outside-in algorithm serves two roles. First, it mitigates lost tracks due to detector inefficiencies, fake tracks, and other ambiguities. Second, it reconstruct tracks originating from decay chains of long lived particles such as b and c hadrons, photon conversions, or other hadronic processes with insufficient hits for the inside-out algorithm. The algorithm works in the opposite direction by first seeding tracks with TRT measurements and then adding hits from the silicon detectors.

The tracks that are used for physics analysis must be within the ID acceptance of $|\eta| < 2.5$, have

$p_{\mathrm{T}} > 0.5$ GeV, and pass additional quality criteria. These criteria include a check of the number of hits in the silicon detectors and the track consistency with the Primary Vertices (PV), the position of the primary pp interaction per bunch-crossing.

The PV is reconstructed using an iterative vertex finding and fitting procedure [127, 128]. The most important quantities entering the algorithm are the longitudinal (z_0) and transverse (d_0) impact parameters. The initial position of the vertex fit is seeded by the beam spot in the transverse plane. Then the tracks and seed are used to iteratively fit the best vertex position using a χ^2 minimization. After each iteration the tracks are reweighted based on their compatibility with the fit. After the final iteration, the final weight of each track is evaluated. Then, any tracks deemed incompatible with the vertex position are removed from the track candidate list and placed back in the pool of unused tracks. The remaining candidates are then used as input to a new vertex finding iteration. The steps are repeated until all of the tracks in an event are used or no more vertices can be found. The PV is the one with the highest $\sum p_{\mathrm{T}}^2$ of associated tracks. This is based on the assumption that charged particles produced in hard-scatter interactions have on average higher p_{T} than those produced in pileup. This is an efficient decision in many cases, except for ones where most of the p_{T} is not carried away by charged particles such as in $H \to \gamma\gamma$. For those processes, alternative PV finding algorithms can be run.

5.2 Topological Calorimeter Clusters

Objects such as electrons and jets are reconstructed using information from the calorimeter known as topological clusters or topo-clusters [118]. These are clusters of energy believed to arise from the same particle shower. The algorithm used to build the clusters is based on estimating the signal significance in adjacent calorimeter cells. The significance is calculated as

$$Z = \left| \frac{E_{\text{cell}}^{\text{EM}}}{\sigma_{\text{noise,cell}}^{\text{EM}}} \right|, \tag{5.1}$$

where $E_{\text{cell}}^{\text{EM}}$ and $\sigma_{\text{noise,cell}}^{\text{EM}}$ are the cell energy and noise, respectively. The cell energy is calibrated to the EM scale using calibration constants derived from test beam measurements. The algorithm begins with all cells in the second calorimeter layer outwards with $Z \geq 4$. Adjacent cells with $Z \geq 2$ are added to form multi-cell clusters. If the same cell is added to multiple clusters, then those clusters are merged. Then, adjacent cells with $Z \geq 0$ are added. Finally, the clusters are checked for cells that exceed 500 MeV and if more than one is found then the cluster is split.

Though not used in this analysis, there is an alternative approach to calibrating the topo-clusters called the Local Cell Weighting (LCW) [118]. This procedure uses cluster properties, such as the energy deposit and shower characteristics, to calibrate the cell. This accounts for the calorimeter's different EM and hadronic responses, proclivity to loose signal due to thresholds applied in the clustering procedure, or inactive/dead material. Large-R jets are often reconstructed using this type of calibration.

5.3 Electrons

Electrons leave tracks in the ID and deposit energy in the ECAL. They are reconstructed in the central region $|\eta| < 2.47$ using directional information from the tracker and energy scale from the calorimeter as shown in Figure 5.1. They can also be produced in the forward region outside of the

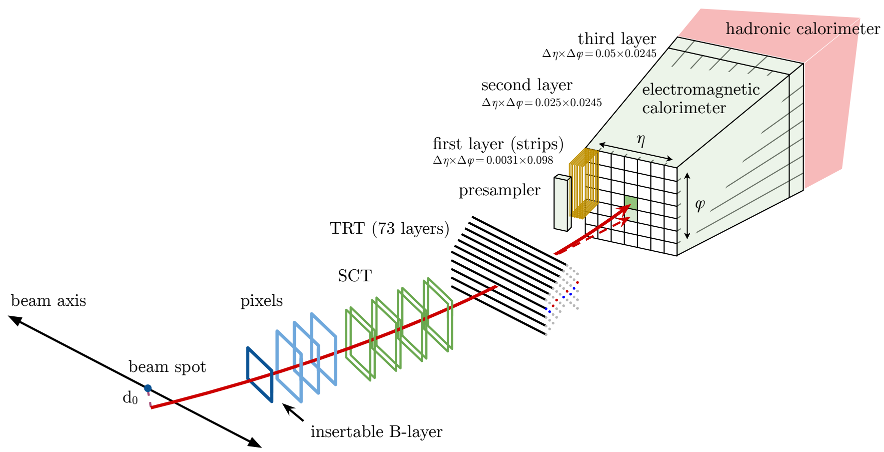

Figure 5.1: An electron passing through the ATLAS detector. The electron path is shown in red as it traverses the tracking system (pixels, SCT, and TRT) and then showers in the ECAL. The dashed red line indicates an example trajectory of a bremsstrahlung photon produced from the electron interacting with the material in the tracker. [129].

detector coverage, but those are not considered in this analysis.

The reconstruction algorithm is seeded with topo-clusters calibrated at the EM scale. Tracks are associated to the topo-clusters and then re-fit using an optimized Gaussian Sum Filter that is designed to account for nonlinear bremsstrahlung effects [130]. The re-fitted, topo-cluster associated tracks are used as seeds to create variable-sized super clusters [131]. These super-clusters also take into account radiation arising from the electron-material interactions.

The energy of the reconstructed electron is determined from the energy deposited within the super-clusters calibrated to the EM scale. The energy is also adjusted by residual corrections that take into account non-uniformity between the ECAL layers and MC-based corrections that calibrate the overall energy scale. The remaining energy scale and resolution differences between data and MC are corrected using measurements from standard processes such as $Z \to ee$ decays. The total electron reconstruction efficiency is measured in data using a tag-and-probe approach. This is used to derive E_{T} and

η correction factors to match the efficiency in simulation and data, ranging from 1–5%. The electron uncertainties are mostly sub-% level.

There are several sources of backgrounds, including electrons from photon-conversions or semi-leptonic heavy-flavour hadron decays and jets with high EM contributions. An identification algorithm is used to maximize the signal versus background acceptance. The algorithm is trained to discriminate $Z \rightarrow ee$ and $J/\Psi \rightarrow ee$ from dijet events, resulting in three working points (Loose, Medium, and Tight) corresponding to the degree of signal acceptance and background rejection. Additionally, electron backgrounds are reduced by requiring that the electron be isolated from other tracks or energy deposits. This is done by rejecting electron candidates for which a cone around the electron contains more energy than a threshold. Events that have electrons are vetoed for this thesis.

5.4 Photons

Photons leave a shower in the ECAL similar to electrons but do not themselves leave a signature in the tracker since they do not have electric charge. There are two types of photons reconstructed, converted and unconverted. Converted photons are those that decay to electron-positron pairs within the tracker volume which then shower in the ECAL. These can be identified by finding a conversion vertex with two tracks of opposite charge. Unconverted photons do not produce a track in the ID. The electron and photon reconstructions are run in parallel, followed by an additional algorithm to distinguish electrons from converted and unconverted photons [129, 132]. Events are not explicitly vetoed with photons for this thesis but any that exist in the dataset are not used in the analysis.

5.5 Muons

Muons produced at TeV energies are minimum ionizing particles that leave tracks in the ID, pass through the calorimeters without depositing significant energy, and leave hits in the MS. Events that have muons are vetoed for this thesis. There are multiple reconstruction schemes that utilize different pieces of subdetector information to enhance efficiency and coverage [133–136].

Muon track candidates in the ID are built as described in Section 5.1. Muon track candidates in the MS are initially built per station with straight lines. The candidates are then extrapolated between stations using parabolic trajectories first relying only on spatial information about the subdetector locations and then information about the magnetic field and energy loss from material interactions. Finally, an ambiguity solver is applied, the final tracks re-fit and compatibility with the IP checked. There are five distinct types of built muons: combined, inside-out, muon-spectrometer extrapolated, segment-tagged, and calorimeter-tagged.

Combined muons are built by matching MS and ID tracks. If two tracks match then the combined hits are re-fit, taking into account the energy loss in the calorimeter. For $|\eta| > 2.5$ the MS tracks may also be combined with hits in the pixel and SCT detectors to produce silicon-associated forward muons. Combined muons are the purest and most commonly used of the reconstruction types.

Inside-out combined muons are reconstructed using an algorithm that extrapolates ID tracks to the MS and searches for at least three loosely-aligned MS hits. The algorithm does not rely on an independently reconstructed MS track. Therefore, the muons recover efficiency in regions of limited MS coverage and at low p_{T}, where they may only reach the early MS stations.

MS extrapolated muons are reconstructed from MS tracks that do not match a ID track. The MS track fit parameters are extrapolated to the beamline, increasing the acceptance outside of the ID to the full MS coverage up to $|\eta| = 2.7$.

Segment-tagged muons are ID tracks that are matched with at least one reconstructed MS track. The muon parameters are taken directly from the ID track.

Calorimeter-tagged muons are reconstructed by extrapolating ID tracks through the calorimeter and searching for energy deposits consistent with a minimum-ionizing particle. If a track is tagged, then the muon parameters are taken directly from the ID track. The p_{T} threshold for ID tracks is raised from 2 GeV to 5 GeV to reduce the large background at low p_{T}.

Muons can also be produced promptly in the hard-scatter *pp* collision or non-promptly from heavy-flavour hadron, kaon, or pion decays. The track of a heavy-flavour decay muons typically agrees with a PV but is less isolated. Kaons and pions, meanwhile, often decay within the detector material and produce tracks with kinks. To discriminate between these types of signal and background muons, a dedicated identification algorithm is used with five working points (Low-p_{T}, Loose, Medium, Tight, High-p_{T}) corresponding to different levels of signal efficiency vs background rejection. The working points are based on the type of muon included and variables used to quantify the agreement between the ID and MS. Muons are further purified using an isolation tagger to remove non-prompt muons from heavy flavour decays.

The energy scale is calibrated to the part-per-million and resolution to the percent level using $Z \to \mu\mu$ and $J/\psi \to \mu\mu$. These processes are also used in tag-and-probe approaches to measure efficiencies as well as apply residual corrections to the simulation.

5.6 τ Leptons

The τ is the heaviest known lepton, decays with a lifetime of about 2.9×10^{-13}s or a proper decay length of roughly 87μm, and has an electric charge of -1. They decay typically before reaching any active regions of ATLAS; 35% of the time leptonically via $\tau \rightarrow l\nu_l\nu\tau$, where l is either an electron or a muon, and 65% of the time hadronically. The leptonic decays produce large amounts of $E_{\mathrm{T}}^{\mathrm{miss}}$. The hadronic decays give rise to narrow jets. Therefore, tau candidates are seeded by jets and the tau vertex is defined as the candidate track vertex with the largest fraction of momentum from tracks with $\Delta R < 0.2$ within the jet. Additional requirements are placed on the position of the vertex using d_0 and z_0. The η and ϕ directions are calculated using topo-clusters within the jet core. A massless approximation is used so that the p_{T} and E_{T} are equal. The tau energy is further calibrated as described in [137]. Though thesis does not expect events with taus, there is no specific tau reconstruction or veto so hadronically decaying taus may be reconstructed as jets but this is a subdominant background.

5.7 Missing Transverse Energy

MET arises when a particle does not interact with ATLAS. Though in the SM this only happens for neutrinos, many BSM theories contain non-interacting particles such dark matter candidates. Information about these particles is inferred by using energy and momentum conservation in the transverse plane (perpendicular to the beamline). This cannot be done in the longitudinal plane (along the beamline) because the incoming longitudinal momentum of the hard-scattering partons is not known as they arise from the PDF's. Since the incoming partons have approximately zero initial transverse momentum, after the collision the transverse momentum of all the produced objects should sum to zero. Therefore, the components of the missing momentum vector are the negative of the sum of all reconstructed objects

$$E^{\text{miss}}_{x(y)} = -1 \times \left(\sum_{i \in \text{hard objects}} p_{x(y),i} + \sum_{j \in \text{soft objects}} p_{x(y),j} \right), \tag{5.2}$$

where the hard objects includ fully reconstructed and calibrated particles (electrons, photons, τ-leptons, muons) and jets. The soft term includes tracks that are not associated to any objects but are compatible with the PV. The set of observables constructed with $E^{\text{miss}}_{x(y)}$ are:

$$\mathbf{E}^{\text{miss}}_{\text{T}} = \left(E^{\text{miss}}_{x}, E^{\text{miss}}_{y} \right), \tag{5.3}$$

$$E^{\text{miss}}_{\text{T}} = |\mathbf{E}^{\text{miss}}_{\text{T}}| = \sqrt{(E^{\text{miss}}_{x})^2 + \left(E^{\text{miss}}_{y}\right)^2}, \tag{5.4}$$

$$\phi^{\text{miss}} = \tan^{-1}\left(E^{\text{miss}}_{x} / E^{\text{miss}}_{y} \right). \tag{5.5}$$

Since experimentally not all objects are reconstructed, $E^{\text{miss}}_{\text{T}}$ is biased towards positive values. The value can also be biased by double counting objects. A dedicated overlap removal is used to mitigate this effect. Systematic uncertainties on $E^{\text{miss}}_{\text{T}}$ are calculated by recomputing the variable for each object uncertainty. The soft term is estimated using events where the $E^{\text{miss}}_{\text{T}}$ recoils off of a reconstructed Z. The uncertainty on the soft term is estimated using SM processes without $E^{\text{miss}}_{\text{T}}$ such as $Z \to ll$. A discussion of the objects, reconstruction, calibration, uncertainties, and resolution is available in [138]. This thesis expects small amounts of $E^{\text{miss}}_{\text{T}}$ but does not explicitly veto it.

5.8 Jets

Quarks and gluons produced in collisions hadronize into color-neutral particles such as pions and neutrons. At high energies, this process leads to collimated sprays of particles known as a jet. These sprays are detected as tracks in the ID and energy deposits in the calorimeter. Experimentally, a jet is built from a set of 4-momentum grouped together by a clustering algorithm, acting as a proxy for the underlying partons. Understanding jets is crucial because they are the most produced objects at the LHC and the main object used in this thesis.

5.8.1 Jet Clustering

A clustering algorithm is used to group objects, such as tracks and calorimeter energy deposits, into jets. There are important considerations for the design and implementation of these algorithms [139, 140]: simple to implement experimentally and theoretically, defined at any order of perturbation theory, yields a finite cross section at any order of perturbation theory, and yields a cross section that is relatively insensitive to hadronization.

The first criteria are practical considerations. For example, an algorithm can be too slow to run experimentally and must be applicable with partons (theory) or detector measurements (experimental) as inputs. The third and fourth requirements are those of infra-red and collinear (IRC) safety, which ensures pQCD calculations are applicable. The last requirement is meant to ensure that jets are representative of the hard partons in the event rather than those arising from non-perturbative effects in hadronization, the activity in the Underlying Event (UE), modifications from detector effects, pileup contamination, and other effects. The two main types of algorithms are cone and sequential-recombination algorithms.

Cone algorithms reconstruct jets by summing the 4-momentum of all particles within a cone and checking if it satisfies a set of criteria [141]. This creates a list of candidate cones which must then be split and merged to find non-overlapping jet cones. This type of algorithm was extensively used at the Tevatron but not at the LHC.

Sequential-recombination algorithms are based on the concept of successive parton branchings as predicted from pQCD. The algorithms attempt to invert the branching by combining particles based on a distance measure that is small when the QCD branching is kinematically favored. Most of the algorithms fall into a family called generalised-k_t algorithms [142] that proceeds as follows.

1. Input the list of objects inside of an event.
2. Using those objects build an inter-particle distance d_{ij} and a beam distance d_{iB}

$$d_{ij} = \min\left(p_{t,i}^{2p}, p_{t,j}^{2p}\right) \Delta R_{ij}^2 \tag{5.6}$$

$$d_{iB} = p_{t,i}^{2p} R^2, \tag{5.7}$$

   where p is a free parameter, ΔR_{ij} is the distance in η–ϕ between pairs, and R is the jet radius.
3. If d_{ij} is the smallest then remove objects i and j from the list and add their combination k. If d_{iB} is the smallest then object i is called a jet and removed from the list.
4. Repeat steps 2 and 3 until all objects are removed from the list.

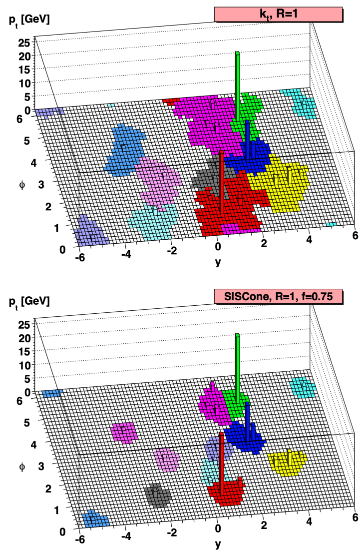

Figure 5.2: Illustration of a parton-level event that is injected random soft ghosts as clustered by four different algorithm [143]. The regular circular shapes created by the anti-k_t algorithm (bottom right) is favorable and used at the LHC.

This class of algorithms guide the clustering process to combine nearby objects which may have originated from a splitting. The k_t algorithm with $p = 1$ combines soft objects since the minimum distance is driven by the smallest p_T [144, 145]. This is based on the idea that soft emissions are enhanced in pQCD. Theoretically this is appealing but experimentally the jets are sensitive to UE and pileup. The Cambridge/Aachen algorithm with $p = 0$ is purely geometrical and is not as sensitive to soft backgrounds but favors nearby objects that could arise from collinear splitting [146] . The anti-k_t algorithm with $p = -1$ is the most widely used algorithm at the LHC since it favors hard particles first [147]. This is advantageous because jets form around hard cores up to a characteristic jet radius, making them insensitive to soft radiation and circular in the η–ϕ plane as shown in Figure 5.2. These features are important for experimental calibration. The jets used in this thesis are built using the anti–k_t algorithm implemented in the `FastJet` package [142, 148].

5.8.2 Particle Flow Jets

Particle-flow objects were introduced in Run 2 to utilize information from both the calorimeters and tracker [149]. In Run 1, jets were built using topo-clusters (calorimeter only) and then calibrated to the particle-level using tracks associated with the jet. By actually building the signal (the objects entering the jet clustering) with both the calorimeter and tracker, the energy resolution is improved. The advantages of tracking information are:

- The design calorimeter energy resolution for single charged pions in the barrel is

$$\frac{\sigma(E)}{E} = \frac{50\%}{\sqrt{E}} \oplus \frac{1\%}{E} \oplus 3.4\%, \tag{5.8}$$

  while the design p_{T} resolution for the tracker is

$$\sigma\left(\frac{1}{p_{\mathrm{T}}}\right) \cdot p_{\mathrm{T}} = 0.036\% \cdot p_{\mathrm{T}} \oplus 1.3\%, \tag{5.9}$$

  where the quantities are measured in GeV. Therefore, for low-energy charged particles the resolution in the tracker is considerably better than the energy resolution of the calorimeter. Additionally, soft particles which may be vetoed by the topo-clusters can be included as tracks.
- The charged particle angular resolution is better for the tracker.
- Soft charged particles originating from a hadronic jet that are swept outside of the jet cone by the magnetic field before reaching the calorimeter can be associated by using the track ϕ.
- Tracks within a jet can be matched with vertices, allowing rejection of pileup matched jets.

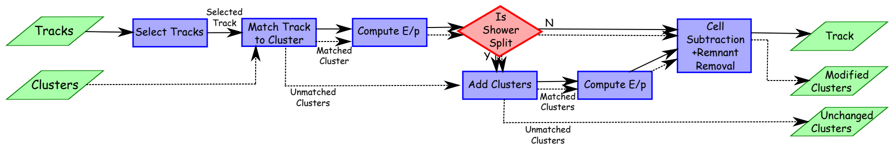

Figure 5.3: Flow chart of the particle flow algorithm. The procedure associates tracks and topo clusters, subtracts the charged particle contribution of the association from the cluster, and returns modified topo clusters as well as the original objects. These objects are then used in jet clustering [149].

Meanwhile, the calorimeter is able to reconstruct charged and neutral particles, has a superior energy resolution at high energies, and has larger geometrical acceptance than the tracker. Therefore, a combination of the two systems provides superior jet reconstruction.

The Particle Flow (PFlow) algorithm takes in tracks and topo-clusters and returns associated tracks, unmodified topo-clusters, and energy subtracted topo-clusters. The routine is shown in Figure 5.3. First, each track is associated to a single topo-cluster and the expected energy deposit in the cluster based on the track is calculated. Then, the algorithm evaluates the probability that the track deposited energy in more than one cluster. If the probability is high, then additional topo-clusters are added to the track/topo-cluster system. The expected energy is subtracted cell-by-cell from the matched clusters. Finally, the topo-cluster remnants originating from shower fluctuations are removed.

The inputs to the anti–k_t algorithm are the positive energy topo-clusters after the energy subtraction step and selected tracks that are matched to the hard-scatter PV with $|z_0 \sin\theta| < 2$ mm. Then, the jet candidates undergo Jet Energy Scale (JES) calibration where the energy scale is corrected to the particle level and the Jet Energy Resolution (JER) is measured.

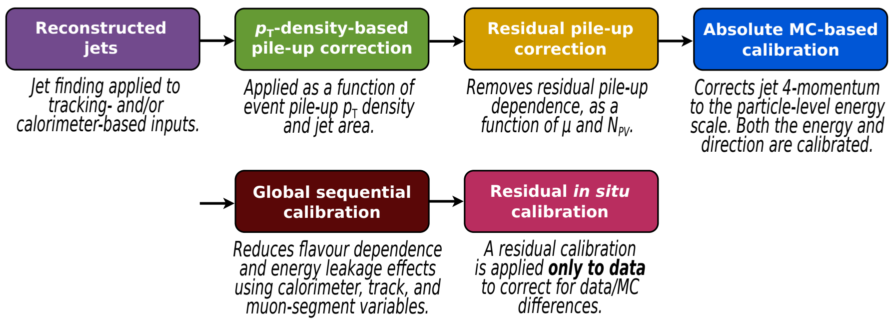

Figure 5.4: Stages of JES calibrations. Each step is applied to the 4-momentum of the jet [150].

5.8.3 Jet Energy Scale Calibration

The calibration addresses experimental effects including pileup contamination, variable detector response, and energy leakage in order for the measured JES to be close to the particle-level scale. The procedure is outlined in Figure 5.4.

First, the jet p_{T} is corrected for energy contamination from pileup. The correction is proportional to the jet area and dependent on the median jet p_{T} density in an event. Then, residual corrections are applied based on the NPV and mean number of interactions per bunch-crossing μ. Next, the jet 4-momenta are corrected to the particle level with E–η dependent factors derived from inclusive dijet samples. Then, a global sequential calibration is applied to reduce flavor dependence and energy leakage using calorimeter, track, and muon-segment variables.

Finally, an *in situ* calibration measures the jet response in data and MC, using the ratio as a correction to data. The jet response is measured by balancing the p_{T} of a jet against a well measured reference object in γ+Jet, $Z(\rightarrow ee)$+Jet, $Z(\rightarrow \mu\mu)$+Jet, and multijet events. The response is defined as the

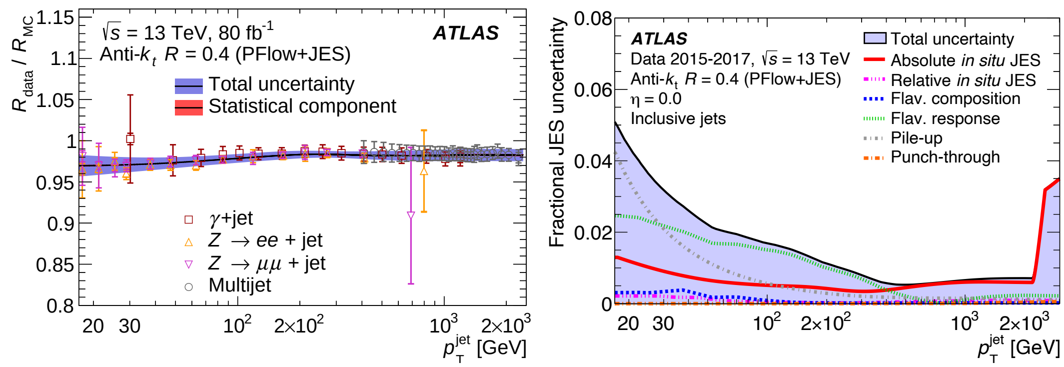

Figure 5.5: (left) Ratio of the PFlow+JES jet response in data to MC as a function of jet p_{T} for Z+jet, γ+jet, and multijet in situ calibrations. (right) The fractional JES systematic uncertainty versus p_{T} for central anti–k_t $R = 0.4$ jets [150].

average ratio of the jet p_{T} to the reference object p_{T} in bins of the reference object p_{T}

$$\mathcal{R} = \langle \frac{p_{\mathrm{T}}^{\mathrm{jet}}}{p_{\mathrm{T}}^{\mathrm{ref}}} \rangle. \tag{5.10}$$

The ratio is sensitive to effects that could change the absolute jet energy, such as additional radiative jets and energy leakage into or out of the jet cone. Therefore, the final *in-situ* calibration is a double ratio $c = \mathcal{R}^{\mathrm{data}}/\mathcal{R}^{\mathrm{MC}}$, shown as a function of the jet p_{T} in the left side of Figure 5.5. The inverse of the curve is taken as a scale factor and applied to data. The individual contributions from the four processes are also compared (unfilled markers). The fractional JES systematic uncertainty is shown in the right side of Figure 5.5.

5.8.4 Jet Energy Resolution

After the jet calibration, the resolution is measured in data [150]. The relative JER is parameterized as a p_{T} dependent functional form expected for calorimeter-responses with three independent contributions arising from noise (N), stochastic (S), and constant C terms:

$$\frac{\sigma\left(p_{\mathrm{T}}\right)}{p_{\mathrm{T}}}=\frac{N}{p_{\mathrm{T}}} \oplus \frac{S}{\sqrt{p_{\mathrm{T}}}} \oplus C. \tag{5.11}$$

The noise term (N) comes from electronic noise in the detector and pileup, which are both approximately independent of any single jet p_{T}. It is expected to be significant up to p_{T} around 30 GeV. The stocastic term (S) is from fluctuations in the amount of energy deposited in the detector and limits the resolution up to several hundred GeV in p_{T}. The constant term (C) arises from fluctuations that are proportional to the jet p_{T} such as the starting point of hadron showers and is dominate in the high-p_{T} region above roughly 400 GeV.

To precisely measure the JER in data, the jets must either recoil against a well measured reference object or be balanced in a well-defined dijet event. The later is preferred because dijets events are frequently produced, well understood theoretically, and approximately balance in the p_{T} of the two leading jets. The dijet events must pass central and forward jet trigger, Jet Vertex Tagging (JVT) selection, and topological criteria. The measurement is done using tag-and-probe in bins of the average jet transverse momentum $p_{\mathrm{T}}^{\mathrm{avg}}$ and the probe jet $\eta_{\mathrm{det}}^{\mathrm{probe}}$.

The noise term of Eq. 5.11 is constrained by measuring fluctuations of energy deposits from pileup in data collected by random unbiased triggers. The measurements are done with the random cone method that sums energy deposits in the calorimeter within random cones with areas similar to anti–k_t $R = 0.4$ jets. The electronic contribution to the noise is estimated using dedicated MC samples with zero pileup $\mu = 0$. The full noise term in the JER combination is the quadrature sum of the

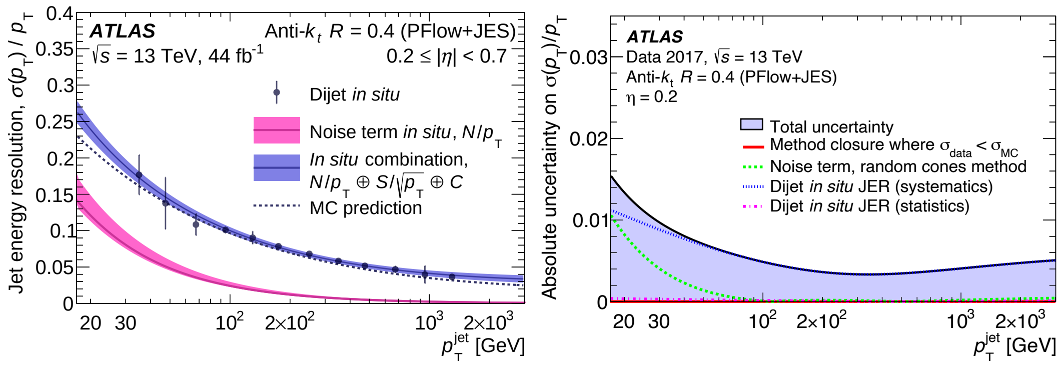

Figure 5.6: (left) The relative jet resolution as a function of p_T for fully calibrated PFlow+JES jets. (right) Absolute uncertainty on the relative JER as a function of p_T [150].

pileup and electronic noises. Systematic uncertainties are applied to account for differences between data and MC as well as fit parameterization instability.

The combined JER measurement is done by performing a fit to the dijet measurements with a constraint on the noise term from the random cone measurements. The functional form from Eq. 5.11 is used to extrapolate across p_T^{jet}. The dijet measurement uncertainties are fully correlated and the noise term uncertainties are propagated while repeating the fit for different values of N. The resulting JER combination for PFlow+JES jets and absolute uncertainties are shown in Figure 5.6. A comparison with EM+JES jets can be found in [150] and in general the PFlow+JES jets beform better at low-p_T where the ID information is helpful.

Part III

Analysis

6

Core Components

This thesis presents a search for the pair production of gluinos, where each gluino subsequently undergoes an RPV decay to either 3 quarks, or 5 quarks via an intermediate neutralino, resulting in a final state with at least 6 or at least 10 jets. Example decay diagrams for these processes are shown in Figure 6.1.

This analysis is particularly challenging since the final state for the signal process is simply jets, iden-

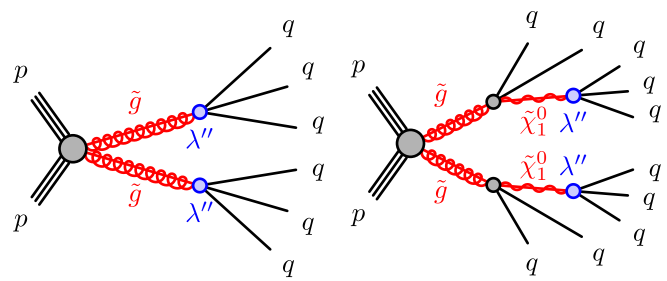

Figure 6.1: Feynman diagrams for pair-produced gluino's decaying to (left) six quarks via RPV $\lambda^{''}$ coupling with an intermediate offshell squark $(\tilde{q})$ and (right) ten quarks through an intermediate neutralino ($\tilde{\chi}_1^0$) which then decays to three quarks via RPV $\lambda^{''}$ coupling.

tical to QCD multijet processes which are abundantly produced at the LHC. Two methods of investigating these signatures are employed by the analysis. The first is a jet counting method, using selections on standard kinematic variables to isolate the signal from the large multijet background then looking for an excess number of highly energetic jets. The second is a novel mass resonance method, using a newly developed Machine Learning (ML) algorithm to exploit the expected resonance from the SUSY particle when the jets from a given gluino are combined.

The chapter provides an overview of core analysis components including the data and MC samples, object definitions, event preselection, data format, and cutflows. The details of the two methods are left for dedicated subsequent chapters.

6.1 Data Samples

The analyses use the full $\sqrt{s} = 13$ TeV Run 2 dataset collected by ATLAS during the years 2015 – 2018. The Good Run List (GRL) is used to select data deemed good for physics by ATLAS, corresponding to a total integrated luminosity of 140 fb^{-1} [151]. The DAOD_PHYS derivation is used with p-tag p5083. Events are also required to pass basic event cleaning requirements to remove events in which a subdetector raised an error flag. Jets are also required to pass cleaning requirements to remove instances of high calorimeter noise signals and non-collision background. After the good run lists are selected, a general preselection is applied to all regions of the analysis based upon the expected kinematics of the direct decay model. The cuts on the cascade model are generally tighter so they are applied downstream during the analysis. All preselection criteria are summarized in Table 6.1 and discussed further below.

Table 6.1: Preselection requirements

Selection Criteria	Value
Trigger selection	`HLT_ht1000_L1J100`
leading jet p_{T}	≥ 200 GeV
H_{T}	≥ 1100 GeV
jet p_{T}	≥ 50 GeV
jet $\lvert\eta\rvert$	< 2.8
Number of Jets	≥ 4

6.2 Signal Model Samples

The two simplified models are shown in Figure 6.1, with the direct decay model on the left and the cascade decay model on the right. Both models probe RPV λ'' couplings. The direct decay model targets heavy pair produced particles (gluino $\tilde{g}$ in the RPV model) decaying directly to quarks. The cascade decay model targets pair produced heavy particles (gluinos) decaying to quarks via an intermediate heavy particle (neutralino $\tilde{\chi}^0$). The signals are generated as LO simplified models using `MG5_aMC@NLO` event generator [152, 153] using the RPV UFO [154] interfaced to Pythia 8 [155].

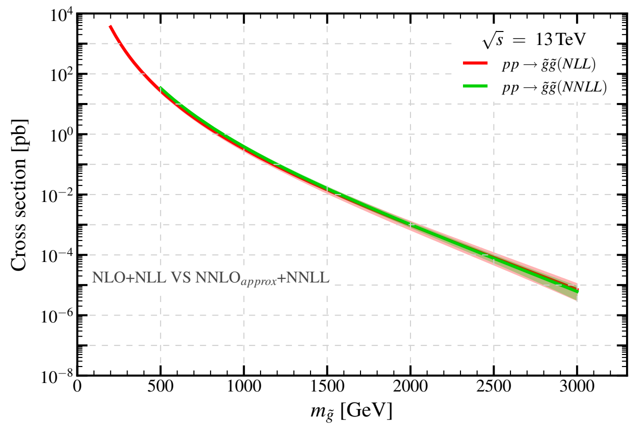

Figure 6.2: The theoretical cross sections for pair produced gluinos in proton-proton collisions as a function of the gluino mass. The red curve computed at next to leading order in the strong coupling adding the resummation of soft gluon emission at next-to-leading-logarithmic accuracy (NLO+NLL). The improved green curve is recomputed at next-to-next-leading order and next-to-next-to-leading-logarithmic (NNLO+NNLL) accuracy [162].

Two additional partons are included in the matrix element calculation to mimic NLO contributions without the full computational cost. The A14 [156] set of tunes are used for UE together with the NNPDF2.3LO PDF set [157]. The EvtGen program [158] is used to generate the events in free space which is then passed through a simulated version of the ATLAS detector using GEANT4 [159, 160]. The signal cross-sections are calculated at NNLO in α_S, adding the resummation of soft gluon emission at next-to-next-to-leading-logarithmic (NNLL) accuracy (NNLO+NNLL) as recommended by the SUSY working group and shown in Figure 6.2 [161].

Simulated signal samples cover a range of $m_{\tilde{g}}$ and $m_{\tilde{\chi}}$. In the direct decay model, the $m_{\tilde{g}}$ is varied from 900 to 2500 GeV in steps of 100 GeV. As shown in Figure 6.2, this targets 4 orders of magnitude in the cross section from 1 pb at 900 GeV to 10^{-4} pb at 2500 GeV. Three sets of samples exist depending on the flavour of final state quarks, targeting light quarks with an optional heavy flavour b-quark. In the first, the non-zero λ''_{112} coupling leads to the $\tilde{g} \to uds$ decay. The second set of samples contain gluino decays of the form $\tilde{g} \to udb$, arising from a non-zero $\lambda^{''}_{113}$ decay. The final two samples contain a mixture where all $\lambda^{''}$ couplings are open. In the cascade model, for each $m_{\tilde{g}}$ in the range 1000 – 2400 GeV, a range of neutralino masses from 50 to 1900 GeV are studied. The three flavour samples are also studied for the cascade model.

6.3 Background Samples

While a data-driven method is primarily used to estimate the backgrounds, simulated events are used to validate part of the methodology and to derive scale factors for the jet counting method. Multijet events constitute the dominant background in the search region, with a small contribution from top-quark pair production ($t\bar{t}$). Other backgrounds including γ+jets, W+jets, Z+jets, single-top quark, and diboson are negligible.

Multijet production was generated using Pythia 8.230, with leading-order MEs for dijet production matched to the parton shower [163]. The renormalization and factorization scales were set to the geometric mean of the squared transverse masses of the two outgoing particles in the ME:

$$p_{\mathrm{T}}^{\mathrm{hat}} = \sqrt{(p_{\mathrm{T},1}^2 + m_1^2)(p_{\mathrm{T},2}^2 + m_2^2)}. \tag{6.1}$$

The NNPDF2.3LO PDF set was used in the ME generation, the parton shower, and the simulation of the multi-parton interactions [157] . The A14 set of tuned parameters was used [164]. Perturbative uncertainties were estimated through event weights that encompass variations of the scales at which α_S is evaluated in the initial- and final-state shower as well as the PDF uncertainty in the shower and the non-singular part of the splitting functions [155]. The fragmentation and hadronization was based on the Lund string model [165, 166]. To populate the inclusive jet p_{T} spectrum efficiently, the sample used a biased phase-space sampling which was compensated for by an appropriately decreasing event weight. Specifically, events at a scale $p_{\mathrm{T}}^{\mathrm{hat}}$ were oversampled by a factor of $(p_{\mathrm{T}}^{\mathrm{hat}}/10\,\mathrm{GeV})^4$.

6.4 Objects

Jets: PFlow jets are constructed with the anti–k_T algorithm and $R = 0.4$ [147]. This strategy offers significant improvements in the JER, reduced pileup jet rates, and a more accurate jet direction in the η–ϕ plane. More details about the reconstruction are in Section 5.8. Jets containing a large particle momentum contribution from pile-up vertices, as measured by the JVT discriminant are rejected if they have $p_T = 20$ – 60 GeV, $|\eta| < 2.4$ and JVT < 0.5 [167]. Jets were selected with $p_{\mathrm{T}} \geq 50$ GeV and $|\eta| < 2.8$.

b-**tagging:** Selected jets are tagged as b-jets if they are within the ID acceptance of $|\eta| < 2.5$ and are identified by a dedicated multivariate algorithm (DL1r). The algorithm uses a selection of inputs including information about the impact parameters of ID tracks, the presence of displaced secondary vertices, and the reconstructed flight paths of b- and c-hadrons inside the jet [168]. The b-tagging algorithm uses a working point with an efficiency of 77%, determined with a sample of simulated $t\bar{t}$ events. The mis-tag rate is 20% for c-jets and 0.9% for light-flavour jets. Differences in efficiency and mis-tag rate between data and MC simulation are taken into account with scale factors [168]. Figure

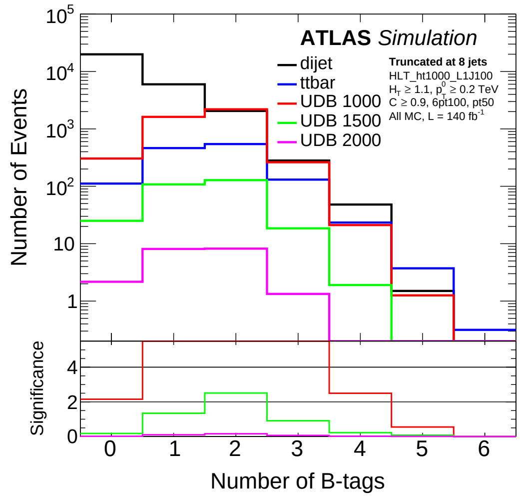

Figure 6.3: Number of b-tags in the signal region for several UDB models, multi-jets, and $t\bar{t}$ MC.

6.3 shows the number of b-tagged jets for several UDB models, the multi-jet MC, and $t\bar{t}$ MC.

Leptons: Events containing an electron or muon are rejected. These leptons are also used in the overlap removal described below. Electron candidates are reconstructed from an isolated ECAL energy deposit matched to an ID track [132], have $p_{\mathrm{T}} > 10$ GeV, $|\eta| < 2.47$, and satisfy the Loose likelihood-based identification criteria [129, 132]. More details can be found in Section 5.3. The longitudinal impact parameter relative to the primary vertex is required to be $z_0 \sin\theta < 0.5$ mm. Muon candidates are formed by combining information from the MS and ID [135]. They are required to have p_{T} > 10 GeV, $|\eta| < 2.7$, $z_0 \sin\theta < 0.5$ mm, and satisfy the Medium identification requirements [135]. More details can be found in Section 5.5

Overlap Removal A procedure is applied to remove non-isolated leptons and avoid double counting tracks and energy depositions associated with overlapping reconstructed jets, electrons, and muons. The procedure applies the following actions to an event:

- If two electrons share a track: the object with lower p_{T} is rejected
- If a muon and an electron share their ID track: electron is rejected, unless the muon is a calo-muon, then the muon is rejected
- If a jet and an electron are within $\Delta R = \sqrt{\eta^2 + \phi^2} < 0.2$: the jet is removed
- If a jet and an electron are within $\Delta R < 0.4$: the electron is removed
- If a jet and a muon are within $\Delta R < 0.2$ or the muon track is ghost associated to the jet: the jet is removed if it's number of tracks is lower than 3 and if the jet p_{T} and total track p_{T} are consistent with the muon FSR or energy loss
- If a muon and a jet are within $\Delta R < 0.4$: the muon is rejected.

Multiplicative scale factors are applied to MC to account for differences between data and simulation for reconstruction, identification and isolation efficiencies, and for the jet momentum scales and JER.

6.5 Trigger

Events are required to pass the lowest un-prescaled H_{T} trigger (`HLT_ht1000_L1J100`) with an online threshold of 850–1000 GeV, depending on the data-taking period. The ATLAS triggering system is described in Section 4.7 and Ref. [115]. The L1 requires events to contain at least one jet with $p_{\mathrm{T}} > 100$ GeV (`L1J100`). The HLT requires $H_T > 1000$ GeV for data recorded in 2016-2018 (`HLT_ht1000_L1J100`) and $H_T > 850$ GeV for 2015 (`HLT_ht850_L1J75`). The turn-on curves are

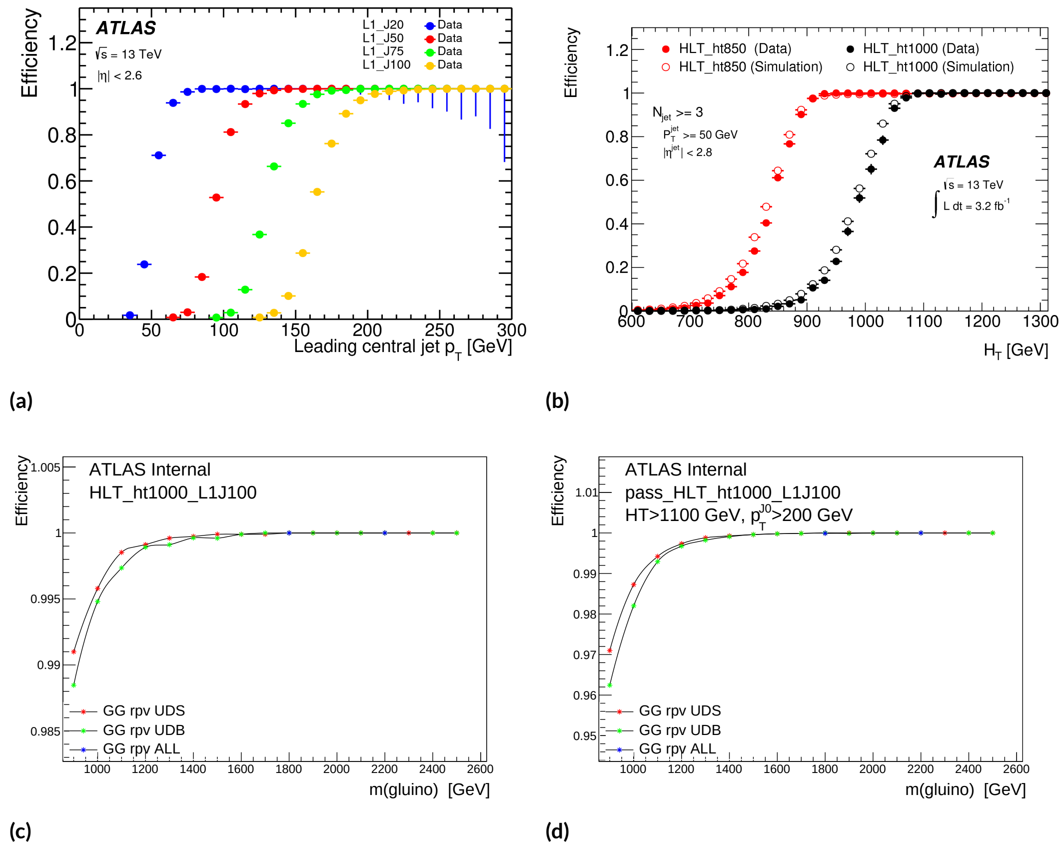

Figure 6.4: Turn-on curves for L1 jet trigger (a) and HLT_ht trigger (b). The trigger used in this analysis is `HLT_ht1000_L1J100`. Efficiency with respect to the total number of signal events for (c) the lowest un-prescaled HT trigger and (d) the lowest un-prescaled HT trigger after the offline plateau selections are applied.

shown in Figures 6.4a and 6.4b. The `HLT_ht1000_L1J100` trigger has an efficiency greater than 95% for signal events, as shown in Figure 6.4c. In order to ensure the trigger plateau, events are required to have $H_\mathrm{T} > 1100$ GeV and leading jet $p_T > 200$ GeV. Figure 6.4d shows that the signal efficiency remains high even after the plateau criteria are applied.

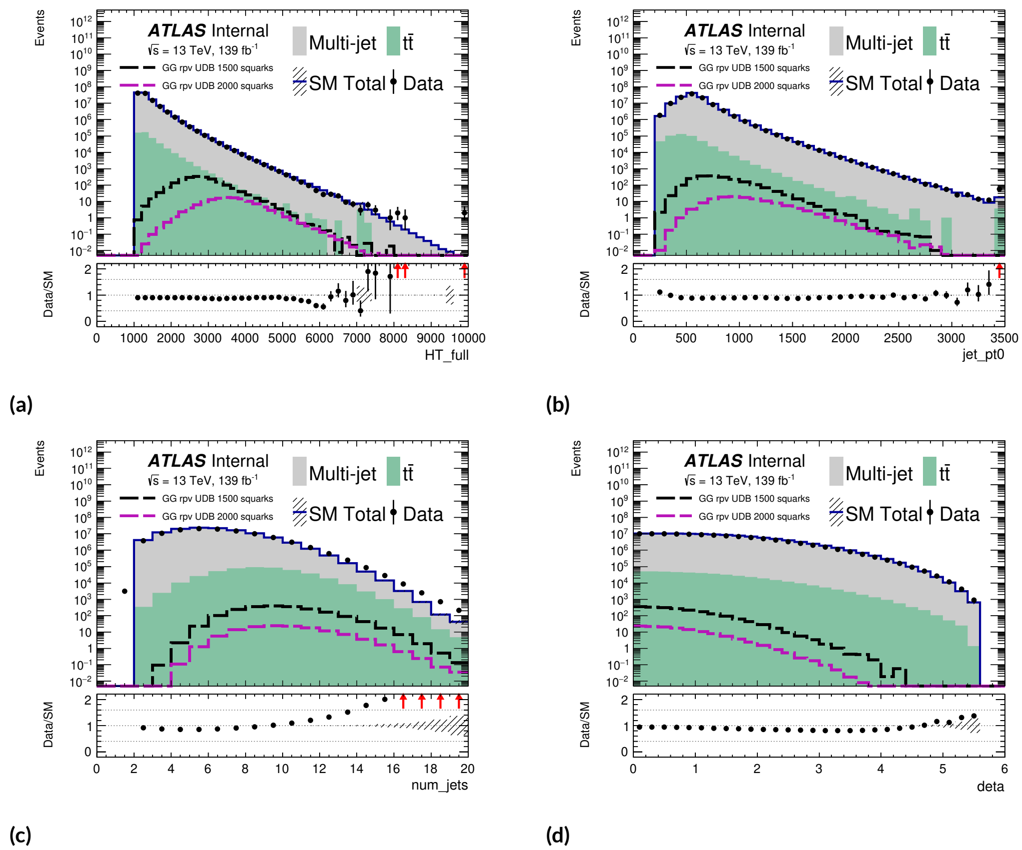

Figure 6.5: Data-MC comparison distributions for the H_{T} (upper left), leading jet p_{T} (upper right), number of jets (lower left), difference in leading jet η (lower right) spectrums. The full Run 2 dataset of $140\,\mathrm{fb}^{-1}$ is shown (black points) compared to the simulated multijet (gray) and $t\bar{t}$ (green) contributions making up the SM total (hatched). Thank you to Lea Halser and John Anders for producing the figures.

6.6 Data-MC Comparisons

Figure 6.5 shows data-MC comparisons for important variables after the preselection: the sum of all accepted jet p_{T} (HT_full), the leading jet p_{T}, the total number of signal jets and the $|\Delta\eta_{12}|$ between the two leading jets per event. The lower panels of the plots show ratio of Run-2 data to MC. Only statistical uncertainties are considered. The H_{T} and leading jet p_{T} distributions have a flat ratio distribution at around ~ 0.95, except for the tails at high values which is covered by the statistical uncertainty, showing that the MC is overestimating the data slightly. These spectra also show that the signals are on average more energetic than the multijet events, an important feature used by both analysis methods. The number of jets distribution shows a trend starting at 7 that the spectrum is not well modeled by MC and a data-driven background estimation is needed. Futhermore, the left panel of Figure 6.6 shows that the n-jets distribution is a strong variable to suppress the multi-jet background.

6.7 Event Topology and C-Parameter

Event shape variables in general describe how energy flows in an event and can be effectively to distinguish isotropic signal decays from the background multijet events. They are defined in such a way to vanish for $2 \to 2$ processes and reach a maximum when the energy is uniformly distributed in the event. Since possible $\tilde{g}$ candidates have high masses, they would be pair produced almost at rest or with a low boost. This results in close to isotropic decays or C-parameter high values. In the opposite direction, the QCD multijets is dominated by dijet events that have lower C-parameter values.

The variable used is derived from the linearised sphericity tensor [169]

$$M_{xyz} = \frac{1}{\sum_i |\vec{p_i}|} \sum_i \frac{1}{|\vec{p_i}|} \begin{pmatrix} p_{x,i}^2 & p_{x,i}p_{y,i} & p_{x,i}p_{z,i} \\ p_{y,i}p_{x,i} & p_{y,i}^2 & p_{y,i}p_{z,i} \\ p_{z,i}p_{x,i} & p_{z,i}p_{y,i} & p_{z,i}^2 \end{pmatrix}. \tag{6.2}$$

Given the normalisation of the M_{xyz} tensor, its eigenvalues (λ_i) are defined such that $\sum_i \lambda_i = 1$. When two of them are zero, the third one must be equal to one. In this case the final state consists

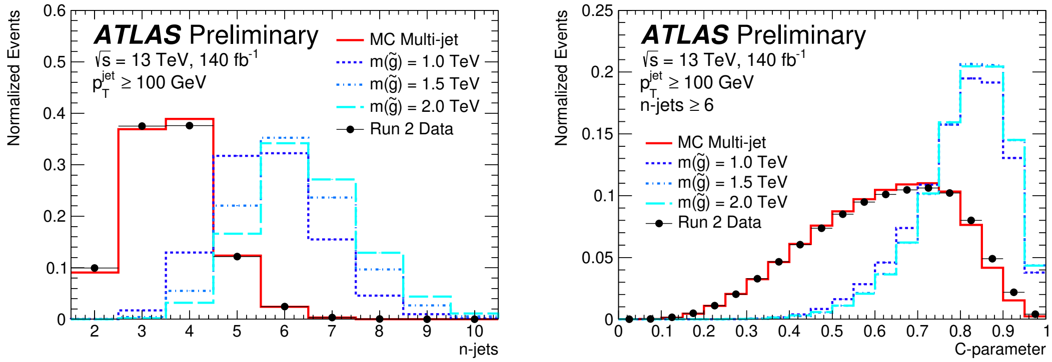

Figure 6.6: Comparison between normalised to unity distributions of the observed data, the QCD Multi-jet background and signal models. Left: n-jets spectrum with a p_{T} requirement of 100 GeV. Right: distribution of the C variable for events with at least 6 jets above 100 GeV.

of two back-to-back jets. If there are three jets with the momenta lying on the same plane, one of the eigenvalues will be equal to 0. If, instead, the spread of the momenta in the final state is close to spherical, the eigenvalues will all be close to $1/3$.

From the eigenvalues of the sphericity tensor, the C-parameter is defined as

$$C = 3(\lambda_1\lambda_2 + \lambda_1\lambda_3 + \lambda_2\lambda_3) \tag{6.3}$$

and its distribution is shown in the right panel of Figure 6.6, comparing the general shape between the Pythia multijet and signal models. The signal events show an isotropic energy flow, featuring a higher distribution of C. The multijet events, instead, have typically lower C values. The variable above roughly 0.9 provides strong seperation power. The modeling of the C-parameter in this region, however, is not perfect, which will be discussed further in the analysis method sections.

The shape of the C-parameter can be understood as follows. For 2 jets events $\lambda_3 = 0$ and the max value of $C = 3(1/2 \cdot 1/2) = 3/4 = 0.75$. So, $C > 0.75$ is possible only in events with n-jets > 2. How that region is populated depends on the p_{T} hierarchy of the jets. If the p_{T} of the two leading jets is much larger than the remaining jets, then $\lambda_1, \lambda_2 \gg \lambda_3 \simeq 0$. While $C = 1$ is achieved ideally for a perfect spherical momentum distribution. For example, for 3-jet events, this could occur if all three jets have an exactly equal momentum magnitude. These types of configurations are rare in multijet events, and thus the C shape has a steeply falling trend after the 0.75 value.

7

Jet Counting Method

The Jet Counting Method (JCM) looks for an excess number of events with high p_{T} jets. This experimental signature is expected from pair produced massive particles that decay all hadronically but not from the multijet background. Previous analyses at $\sqrt{s} = 7$ and 8 TeV searched for similar signatures but did not observe an excess [170, 171]. This iteration uses additional cuts on the C-parameter and number of b-tagged jets. Though no excess is observed, exclusion limits on the signal models are significantly extended. This chapter is largely adapted from a note produced by Stefano Franchellucci, Pantelis Kontaxakis, and Anna Sfyrla.

A main advantage of this method is its simplicity – events are counted in signal regions and the SM background is estimated. Then, the yields are interpretted in background only and signal plus background scenarios. The results can be reinterpreted following the same procedure for other signal models. The analysis strategy, background estimate, systematic uncertainties, method validation, and results are discussed in Sections 7.1 – 7.5.

7.1 Strategy

The spectra shown in Figure 7.1 are used to optimize Signal Region (SR) definitions for the direct decay models. The bin content is equal to the number of MC events where ≥ 7 jets are counted above the p_{T} threshold reported on the horizontal axis. The signal over background ratio and the significance assuming a 30% uncertainty on the background are given in the bottom panels [172]. The background rejection improves significantly with a selection on the C-parameter as shown in Figure 7.1b.

For the cascade decay models, the number of jets depends on the mass difference between the $\tilde{g}$ and the intermediate $\tilde{\chi}_1^0$, denoted $\Delta m_{\tilde{g}-\tilde{\chi}_1^0} = m_{\tilde{g}} - m_{\tilde{\chi}_1^0}$. If $\Delta m_{\tilde{g}-\tilde{\chi}_1^0}$ is large then the neutralino may be highly boosted, which could lead to quarks with overlapping parton showers and merged jets in reconstruction. For this case, a n-jet threshold at 7 is found to be sufficiently sensitive. When $\Delta m_{\tilde{g}-\tilde{\chi}_1^0}$ is an intermediate size, the energy may be well distributed among the decay products and a higher requirement of 8 jets improves background rejection considerably as shown in Figure 7.2.

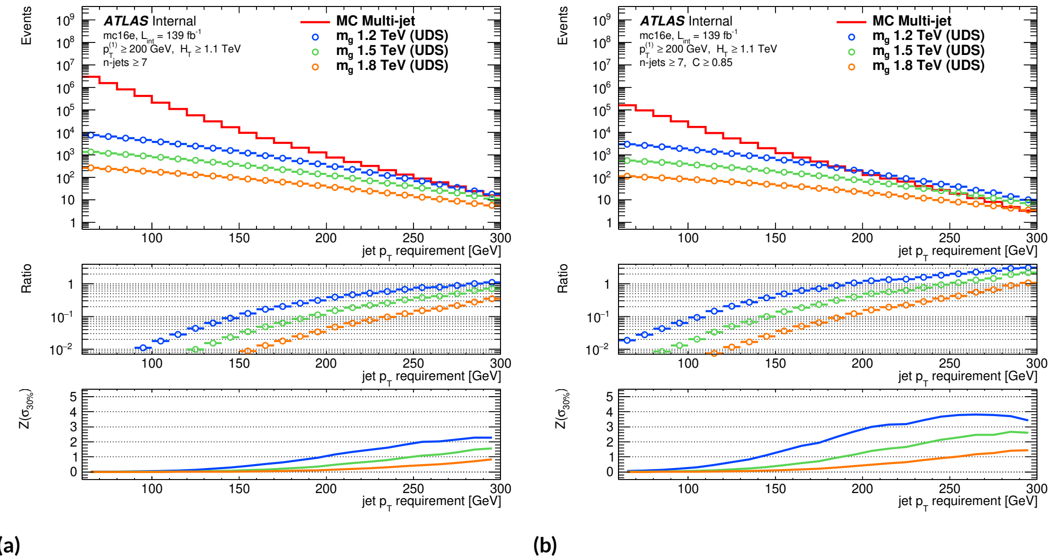

Figure 7.1: Histograms showing the number of events counted in MC samples containing at least 7 jets with p_T above the one reported in the horizontal axis without (a) and with (b) an additional cut on the C-parameter. The middle panel shows the ratio of the counts between signal and background simulations. The bottom panel shows the significance computed using the MC yields and assuming 30% systematic uncertainty on the background counts. The multijet background (red) and three direct decay signal models (blue, green, orange) are shown.

Lastly when $\Delta m_{\tilde{g}-\tilde{\chi}_1^0}$ is small, the neutralino is produced at threshold so most of the energy will be carried by its decay products. The jets produced directly from the gluino may be soft enough to merge, leading to a similar final state as the first case where a ≥ 7 jet selection is sufficient.

The SM background is estimated by extrapolating the number of events across N_{jets} using data and MC for the overall scale and extrapolation factors, respectively. It makes use of a Control Region (CR) with a low p_{T} requirement to calibrate the background to data as well as a Normalization Region (NR) at lower jet multiplicities. The closer these two regions are to the SR, the better the method is expected to perform. However, if they are too close then there may be substantive signal contamination which would bias the prediction. The amount of bias depends on the given model. The regions optimized

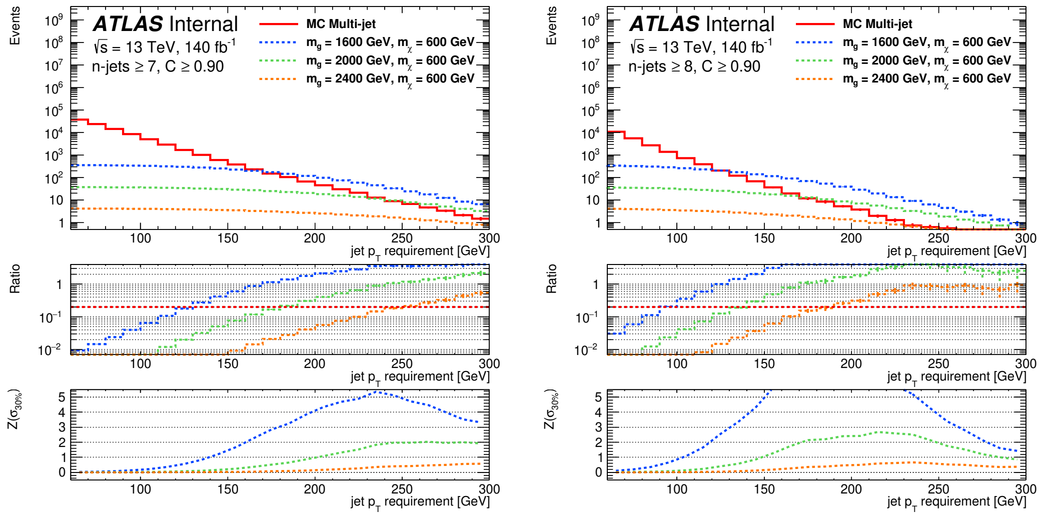

(a) **(b)**

Figure 7.2: Histograms showing the number of events counted in MC samples containing at least 7 (a) or 8 (b) jets with p_T above the one reported in the horizontal axis. The middle panel shows the ratio of the counts between signal and background simulations. The bottom panel shows the significance computed using the MC yields and assuming 30% systematic uncertainty on the background counts. The multijet background (red) and three direct decay signal models (blue, green, orange) are shown.

for the UDS models were chosen to have a CR at 60 GeV. In this way, as shown in Figure 7.7, minimal bias is expected on the background prediction. Dedicated Validation Region (VR) are used to check and validate the background prediction methodology prior to unblinding. The method is discussed in detail in the following section.

For the UDB scenarios an additional event selection based on the number of b-tagged jets is used to further enhance the expected signal to background yields. However, the selection considerably increases the signal contamination in the CR and VRs for the lowest mass gluinos. Consequently, a two-step sequential unblinding procedure is used.

	N. jets	jets p_T [GeV]	C cut	b-tags	Predicted Background	Observed Events	Target model
SR1		180		-	$130.8^{+9.8}_{-30.0}$	115 ± 11	(2×3) small masses
SR2	≥ 7	220	≥ 0.90	-	$25.5^{+4.7}_{-4.7}$	24 ± 5	(2×3) medium masses
SR3		240		-	$11.2^{+1.8}_{-2.9}$	12 ± 3	(2×3) high masses
SR4	≥ 8	180	≥ 0.85	-	$27.3^{+3.6}_{-7.7}$	33 ± 6	(2×5)
SR5	≥ 8	220	≥ 0.85	-	$4.6^{+1.9}_{-1.7}$	7 ± 3	(2×5)
SR1bj	≥ 7	180	≥ 0.85	≥ 2	$36.4^{+3.2}_{-3.2}$	26 ± 5	(2×3) UDB high mass
SR2bj	≥ 8	180	≥ 0.85	≥ 2	$4.8^{+1.0}_{-1.0}$	2 ± 1	(2×5) UDB high mass

Table 7.1: Signal regions definitions. The counting of the jets is to be considered at the given p_T threshold. The background prediction is always normalized using scale factors computed in CRs at lower jet p_T requirements.

	N. jets	jets p_T [GeV]	C cut	Predicted Background	Max Signal Contamination	Observed Events
VR-A1		180	≥ 0.80	$72504.4^{+1845.7}_{-2411.3}$	12.0%	70184 ± 265
VR-A2	5	160	≥ 0.85	$65051.5^{+1763.9}_{-2182.2}$	10.8%	64985 ± 255
VR-A3		150	≥ 0.90	$29542.0^{+2134.9}_{-999.0}$	11.7%	30360 ± 174
VR-B1		120	≥ 0.80	$79593.8^{+2185.9}_{-2818.1}$	11.6%	80271 ± 283
VR-B2	6	110	≥ 0.85	$58246.9^{+3875.2}_{-1824.4}$	11.5%	59997 ± 245
VR-B3		100	≥ 0.90	$28499.1^{+1006.3}_{-2015.0}$	11.5%	30212 ± 174
VR-C1		180		$347.7^{+37.1}_{-72.7}$	11.1%	372 ± 19
VR-C2	≥ 7	220	≤ 0.60	$47.8^{+6.1}_{-10.4}$	12.8%	35 ± 6
VR-C3		240		$18.3^{+3.7}_{-2.9}$	16.0%	14 ± 4
VR-D1	≥ 8	180	≤ 0.60	$22.9^{+5.0}_{-6.3}$	23.1%	16 ± 4

Table 7.2: Validation regions definitions. The counting of the jets is to be considered at the given p_T threshold. The background prediction is always normalized using scale factors computed at lower jet p_T requirements.

First, the models are checked using SRs without b-tagging as defined in Table 7.1. Each model is tested in the region with maximal sensitivity. If no statistical excess is seen above 2σ, the method is validated with b-tag selections using the VRs defined in Table 7.3 (CASE 1). Instead, if an excess is seen then regions with exclusive b-tagging selections are used to validate the method as defined in Table 7.3

	b-tags	N. jets	jets p_T [GeV]	C cut	Expected Background	Max Signal Contamination	Observed Events
				CASE I			
VR-A-bj	≥ 2	5	180	≥ 0.85	$1664.5^{+43.2}_{-43.2}$	17.3%	-
VR-B-bj	≥ 2	6	120	≥ 0.85	$2776.9^{+79.2}_{-79.2}$	13.6%	-
VR-C-bj	≥ 2	≥ 7	180	≤ 0.60	$32.2^{+3.0}_{-3.0}$	8.6%	-
VR-D-bj	≥ 2	≥ 8	160	≤ 0.60	$7.6^{+1.3}_{-1.3}$	9.9%	-
				CASE II			
VR-A-0bj	0	5	140	≥ 0.85	$82794.6^{+493.0}_{-493.0}$	1.0%	-
VR-A-1bj	1	5	140	≥ 0.85	$19927.9^{+236.1}_{-236.1}$	19.2%	-
VR-B-0bj	0	6	100	≥ 0.80	$130659.9^{+651.1}_{-651.1}$	0.8%	-
VR-B-1bj	1	6	100	≥ 0.80	$36240.0^{+322.3}_{-322.3}$	16.3%	-
VR-C-0bj	0	≥ 7	180	≤ 0.60	$289.1^{+12.4}_{-12.4}$	1.3%	-
VR-C-1bj	1	≥ 7	180	≤ 0.60	$86.3^{+5.5}_{-5.5}$	17.8%	-
VR-D-0bj	0	≥ 8	140	≤ 0.60	$228.0^{+18.2}_{-18.2}$	0.8%	-
VR-D-1bj	1	≥ 8	140	≤ 0.60	$58.6^{+4.9}_{-4.9}$	20.1%	-

Table 7.3: Validation regions with b-tagging. The case I refers to the scenario where no excess is seen during the first unblinding step. In this case, the $m_{\tilde{g}} = 1.3$ TeV UDB model considered for the maximal signal contamination. While case II considers the eventuality of a 2σ excess. Here, $m_{\tilde{g}} = 0.9$ TeV is considered for potential signal contamination. In both cases, the Expected Background column contains the MC yields coming from multijet and $t\bar{t}$ samples, and the associated error correspond to the MC statistical error.

and the CR is not used (CASE II). If the background estimate in the VR has bad closure with data, then an additional systematic error is included.

7.2 Background Estimate

The background extrapolation uses MC samples to compute transfer factors across different jets multiplicities and data to normalize the prediction. The number of events with a given jet multiplicity

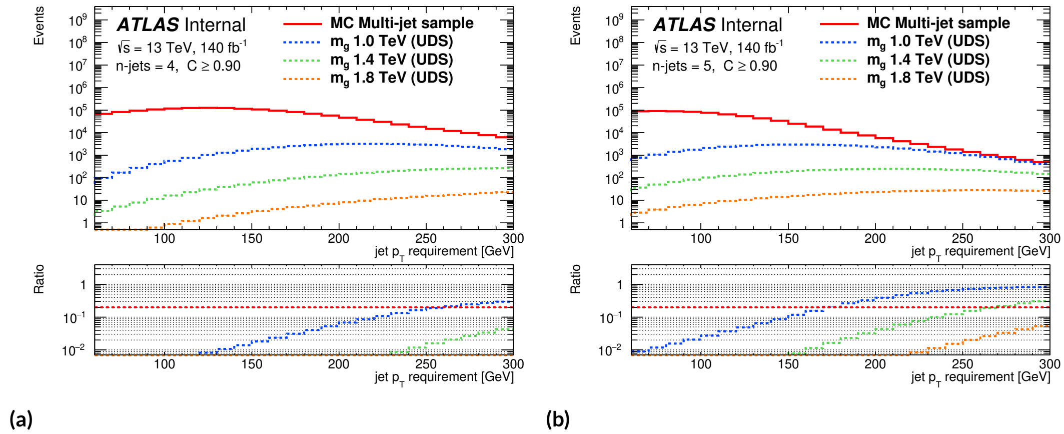

Figure 7.3: The event yields in MC samples with different jets p_T thresholds. Figures (a) and (b) correspond to the exclusive n-jets equal to 4 and 5, respectively, along with a C requirement of at least 0.9. The bottom panels show the ratio of the counts between signal and background. The red dotted line represents the threshold of tolerable signal contamination, arbitrarily set to 20%.

of N above a certain p_T, can be extrapolated as:

$$N_{n-\text{jets}}^{\text{Extr.}} = N_{m-\text{jets}}^{\text{Data}} \cdot \frac{N_{n-\text{jets}}^{\text{MC}}}{N_{m-\text{jets}}^{\text{MC}}}, \tag{7.1}$$

where $m < n$ and the m-jets (exclusive) region should be ideally signal free to avoid introducing bias. Since the signal is characterized by a large multiplicity in the final state, high background purity is expected in events with a low number of jets (< 6). Figure 7.3 shows the expected yields for QCD multijet events and gluino events in low exclusive n-jets bins, demonstrating that events with up to 4 and 5 jets can be used in data for normalizing the background prediction.

As previously mentioned, at first approximation the main source of background is the multijet events. Therefore, the transfer factors are estimated using only the simulated multijet samples. These factors are computed using an exclusive number of jets selection while the signal regions are inclusive. Consequently, if the target regions have a requirement of at least n jets, the extrapolation will be a sum

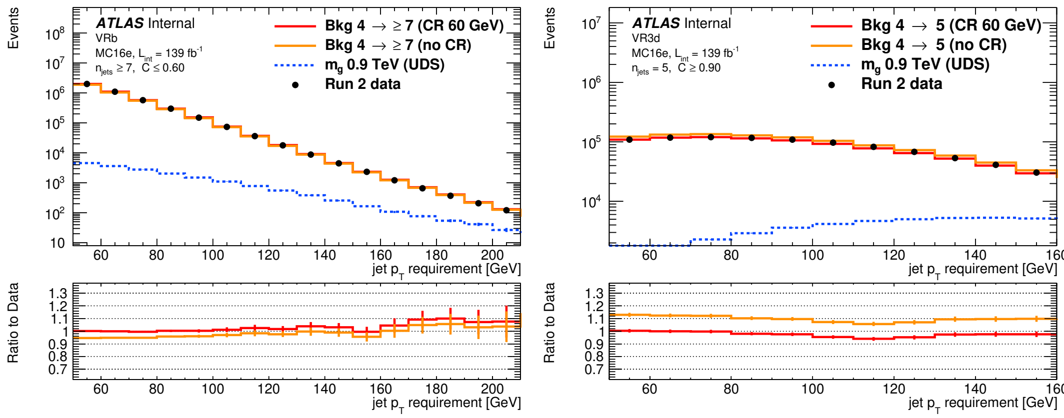

(a) (b)

Figure 7.4: Comparison between the background prediction and data, in different validation regions. Figure (a) shows the test of the method when extrapolating from m =4 to n ≥7 jets, with C≤ 0.6. While in (b) the extrapolation is done for m =4 to n ≥5 jets, but with the inverted C cut, C≥ 0.9. The red histograms show the background extrapolated using the scale factors computed in the CR at a jet p_T requirement of 60 GeV, comparing data and MC. While the orange histograms are the predicted background yields, without the usage of such scale factors.

of the regions with exactly j-jets, where $j \geq n$. This sum can be truncated at $j = n + 2$ since higher multiplicities bring a negligible contribution ($< 0.5\%$) that decreases further at high p_{T}.

To account for the mismodeling of the multijet spectrum from MC, scale factors are estimated from direct comparisons with data in CRs. The scale factors ($s_n = s_n \mid_{p_T \geq p_{T_0}}$) are derived for the MC yields in Eq. 7.1 with a low $p_{T,0} \geq 60$ GeV threshold. This places the CR as close as possible to the SR with minimal signal contamination. For example, the extrapolation from m=4 to $n \geq 7$ jets is

$$N^{\text{Extr.}}_{\geq 7\text{jets}} = \sum_{i=7}^{9} w_{4i} \cdot N^{\text{Data}}_{4-\text{jets}} \cdot \frac{N^{\text{MC}}_{i-\text{jets}}}{N^{\text{MC}}_{4-\text{jets}}}; \qquad w_{4i} = \frac{s_i}{s_4}; \qquad s_i = \left.\frac{N^{\text{Data}}_{i-\text{jets}}}{N^{\text{MC}}_{i-\text{jets}}}\right|_{p_{\mathrm{T}} \geq 60\text{ GeV}}. \tag{7.2}$$

The impact of the scale factors can be seen in Figure 7.4, where the closure in 2 VRs is shown to improve with the additional corrections.

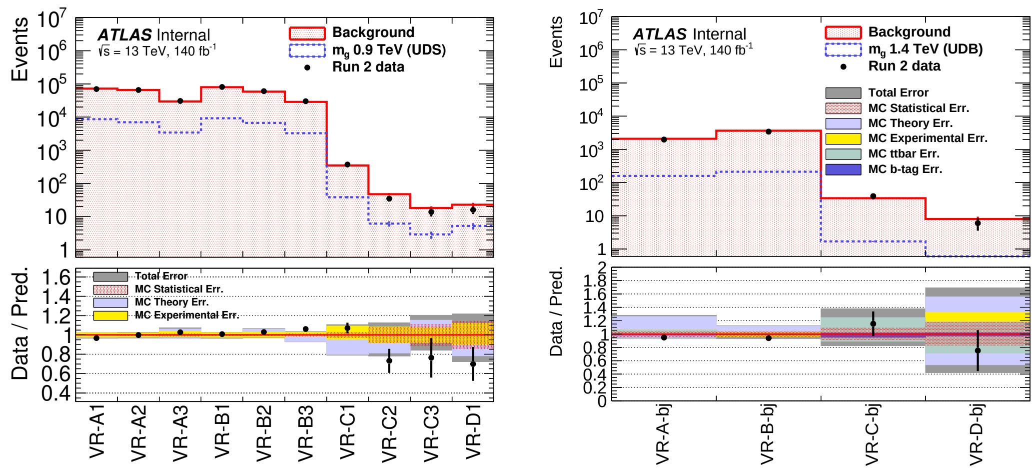

Figure 7.5: Closure test of the background method in all VRs. The background is extrapolated from a n-jet $= 4$ using a CR at 60 GeV. The bottom panel shows the ratio of data over the predicted number of background events. In this panel, the red-shaded region represents the MC statistical error, the light-blue band is the MC theory error and the yellow band is the sum in quadrature of all the JES and JER errors. The grey region is the combination of all these uncertainties.

The closure of the background prediction for the rest of the VRs listed in Table 7.2 is shown below in Figure 7.5. The NR uses n-jets = 4 and the CR uses $p_\mathrm{T} \geq 60$ GeV. There is an agreement between data and the predicted background within the errors for all regions, with the exception of a 5% deviation in VR-B3. A closure uncertainty of 5% is added in quadrature to account for this mismodeling. To further check the robustness of the method, predictions are done in slices of C and compared to data at different jet multiplicities in Figure 7.6. Despite the MC mismodeling known from previous measurements [169], the extrapolation procedure shows fairly accurate results.

Lastly, signal injection tests are performed to check that the method is robust against possible signal contamination. These are done by predicting the yields using Equation 7.2 while replacing data with combinations of MC multijet plus signal samples. Then, the obtained predictions are compared to the pure MC multijet yields. Figure 7.7 displays the predicted number of events from the method, with

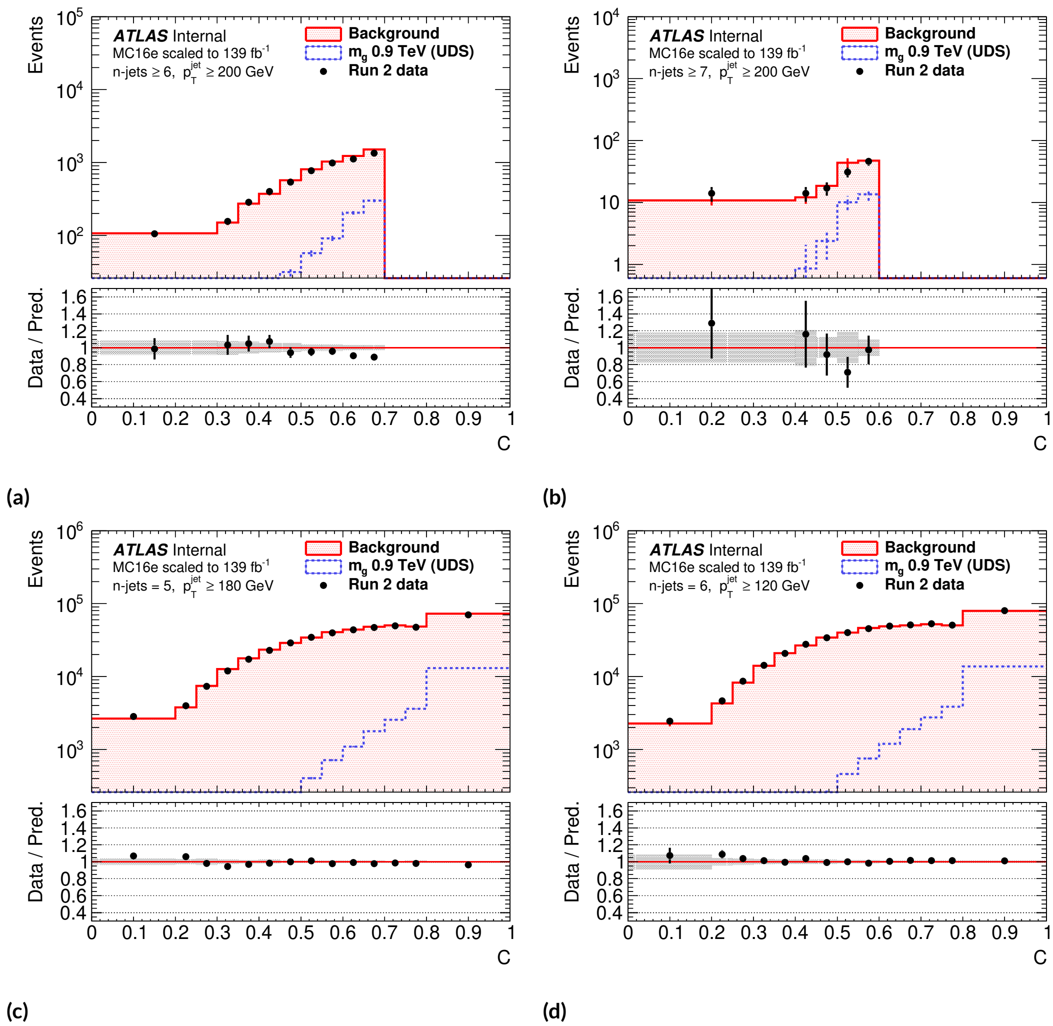

Figure 7.6: Closure test of the background method in binned regions of C. Figures (a) and (b) show respectively subsets of VRa and VRb. While in (c) and (d) the bin at highest C are exactly VR1d and VR1e. The background was extrapolated from a jet multiplicity of 4, and with a CR at 60 GeV. The bottom panel shows the ratio of data over the predicted number of background events. In this panel, the grey-shaded region represents the MC statistical error.

and without signal injection, and the signal events, for all the signal regions. Only the lowest mass points introduce a bias in the background. However, the expected signal-to-noise ratio in the SRs is high enough such that the sensitivity is minimally affected.

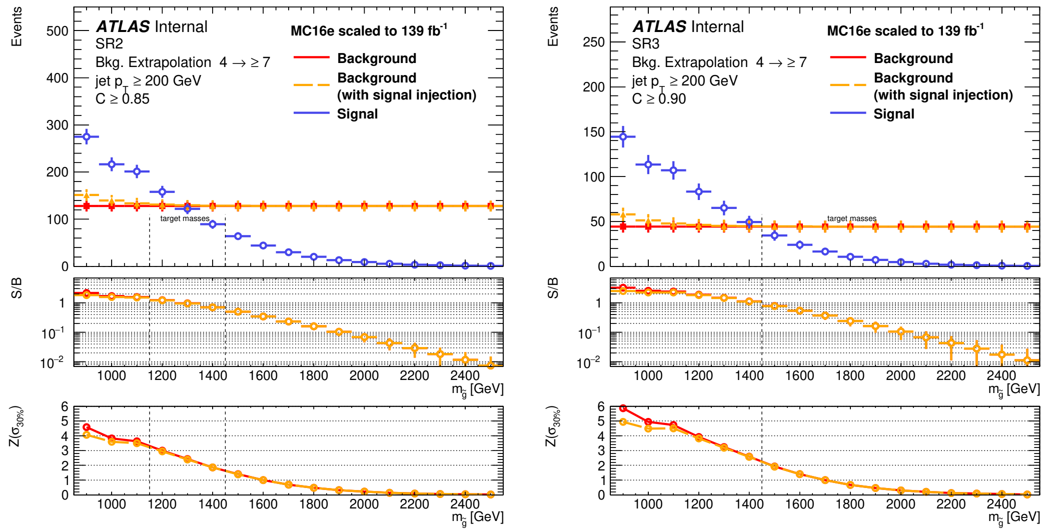

Figure 7.7: Yields in the various SRs using MC only from signal injection tests. The background distribution (red) is obtained for the multijet samples. The background with signal injection (orange), is obtained by replacing the data terms with multijets plus signal events in Equation 7.2. The p_{T} threshold used for the CR is 60 GeV.

7.3 Uncertainties

Different types of systematic errors were considered for this analysis. They can be split into three categories: modeling, experimental, and methodological errors. The first category is mostly accounting for the lack of knowledge and the approximations made in the MC calculations. The experimental errors derive from the calibration procedures. The methodological errors arise from the background method estimation. A final summary of all the uncertainties is outlined in section 7.3.4.

7.3.1 Modeling

This class includes systematic effects in the modeling of both backgrounds and signals. However, the QCD multijet background is expected to have the most relevant uncertainties. The main sources of errors in the MC simulations are: missing higher orders in the perturbative expansion of the partonic cross-section, PDF uncertainties, strong coupling constant α_s uncertainties. The effect of these is evaluated by varying the relevant parameters of the simulation. Using a standard technique, different MC event weights are produced for multiple variations. In this way, the MC sample can be re-weighted according to the different simulation configurations. The predictions of the background and signal yields obtained for each variation are compared to the nominal samples. The distance between nominal and re-weighted yields are quoted as uncertainties.

MC multijet: The considered variations are combined into three different sets, where events weight evaluating the same systematic effect are grouped. The combinations are done by taking an envelope of all the uncertainties. In most of the regions, the highest systematic error is related to the modeling of ISR and FSR. In some cases, strong fluctuations are seen with high statistical uncertainties. These are caused by few events with large weights. To avoid having these large fluctuations, some events were excluded following an outlier removal procedure. An alternative Sherpa sample was also considered, but given the high discrepancies in data comparisons no additional uncertainty was assigned.

MC $\mathbf{t\bar{t}}$: A similar procedure to the multijet case is used also for $t\bar{t}$ but only for the search regions with b-tagging requirements. Both event weights and alternative generators are used.

Signal: The MC event weights are varied to test the impact of the renormalization scale, factorization scale, α_S value, and PDF uncertainties. The method is repeated for each variation to derive an uncertainty and included as Nuissance Parameter (NP)s.

7.3.2 Experimental

Jet Energy Scale and Resolution: The Global Reduction JES with 23 NPs and Simple JER with 8 NPs are used. The background extrapolation was done for each variation and then compared to the nominal one. All VRs were checked and the systematic effects have an impact well below 10%. In the final fit procedure these are included as NPs for both the signal and the background.

Scale Factors: Uncertainties on the b-tagging and JVT scale factors are included for both signal and background as NPs arising from event weight variations.

Luminosity: A luminosity uncertainty is applied as a scale factor to the normalization of the signal samples. For the combined Run 2 dataset, a luminosity uncertainty of 0.8% is used on the measured value of $140068.94\ \mathrm{pb}^{-1}$.

7.3.3 Methodology

VR non-closure: In almost all the tested VRs, the predicted background and the data are compatible within 1σ of the uncertainties. Only one region (VR-B3) has a larger fluctuation, leading to a 4.8% systematic error for regions with a tight C selection ($C \geq$0.9) to cover the observed discrepancy.

7.3.4 Systematics summary

The systematic uncertaintes are summarized below in Table 7.4.

Uncertainty type	# NP	Short description
Signal statistics	1	Weighted Poisson error, computed as the sum of MC weights $\sum_i \sqrt{w_i^2}$
Background statistics	1	MC and data Poisson errors from CR, NR and transfer factors, propagated for equation 7.2
MC multijets	3	MC theory uncertainties with highest contributions, mostly coming from PDF, scale, ISR and FSR modeling uncertainties
MC $t\bar{t}$	4	Similar to multijets, includes Hard Scatter, Parton showering, ISR and FSR modeling uncertainties
MC signal	7	Signal modeling systematics, mostly scale and PDF uncertainties (excluding errors on the cross-section)
JES/JER set	31	Jet energy scale and resolution errors, for the Global Reduction JES and Simple JER sets; this uncertainty is applied to both signal and background
Flavour tagging	5	Uncertainties on b-tagging scale factors; this uncertainty is applied to both signal and background
Jet-vertex tagging	1	Uncertainties on JVT scale factors; this uncertainty is applied to both signal and background
Luminosity	1	Uncertainty on the total Run 2 luminosity (0.8%)
VR non-closure	1	Error to account discrepancies above 1σ in VR, only for $C \geq 0.9$

Table 7.4: Summary of the uncertainties considered for the jet counting method.

7.4 Statistical analysis

A procedure to set limits on the models of interest, in the context of the cut and count (CCA) approach, using the jet-counting method is performed. The software package `pyhf` [173, 174] was used. A profile likelihood ratio combining Poisson probabilities for signal and background is computed, in a single bin, to determine the confidence level (CL) for consistency of the observed data with the signal-plus-background hypothesis (CL_{s+b}). An analogous calculation is performed for the background-only hypothesis (CL_b). From the ratio of these quantities, the confidence level for the presence of signal (CL_s) is determined and it is treated as a modified pseudo-frequentist p-value.

The definitions of the search regions in Table 7.1 were obtained before the unblinding of the data, using the CL_s method. The method was tested over a grid of possible selections. The regions giving the best-expected limits were then chosen. For the optimization all the uncertainties were considered, as summarised in Table 7.4. The tested selections thresholds are: n-jets $\times\, p_{\mathrm{T}} \times C = [7; 8] \times [160; 260]\mathrm{GeV} \times [0.8; 0.95]$.

The results of performing the limit-setting procedure in the signal regions are shown for SR1, SR2 and SR3 in Fig.7.8a as a function of gluino mass for the six-quark (light flavor) model. These results show the expected cross-section limits in comparison to the predicted cross-section from the theory. Under the assumption that all RPV decays are to light-flavor quarks, gluino masses of $m_{\tilde{g}} < 1600$ GeV are expected to be excluded at the 95% CL.

Figure 7.8b shows the expected limits in the $(m_{\tilde{g}}, m_{\tilde{\chi}_1^0})$ phase space, for the cascade decay models in the best-performing regions. For the model where no b-tagging is used, gluino masses above 2200

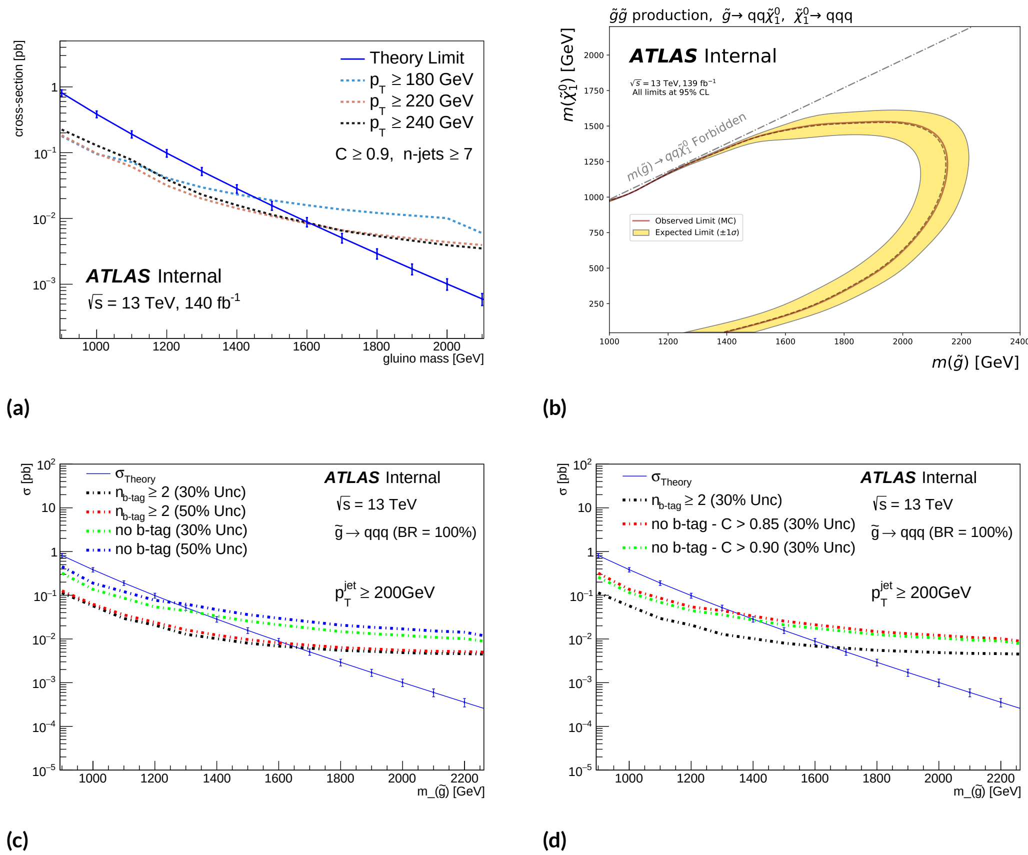

Figure 7.8: Expected cross-section limits at a 95% CL for the direct and cascade decay models. All systematic uncertainties are included in the fitting procedure unless mentioned otherwise. (a) Direct decay UDS scenario where the different dashed represent limits for the three different signal regions (SR1, SR2 and SR3). (b) Exclusion contours in the $(m_{\tilde{g}}, m_{\tilde{\chi}_1^0})$ mass plane for the ten-quark (light flavor) gluino cascade decay models. (c-d) Direct decay UDB scenario where (c) shows the impact of the b-tagging requirement at different systematic uncertainty levels and (d) shows the improvement from including a b-tagging selection.

GeV are expected to be excluded at the 95% CL for the region of $800 < m_{\tilde{\chi}_1^0} < 1600$ GeV and up to 1600 GeV for $m_{\tilde{\chi}_1^0} \geq 50$ GeV.

To further improve the reach of the analysis, regions with flavor tagging selections are also used. These are especially relevant for the UDB models, where each gluino decay produces b-quark. A similar optimization procedure was done also in this case, to identify the best cuts. The highest sensitivity is

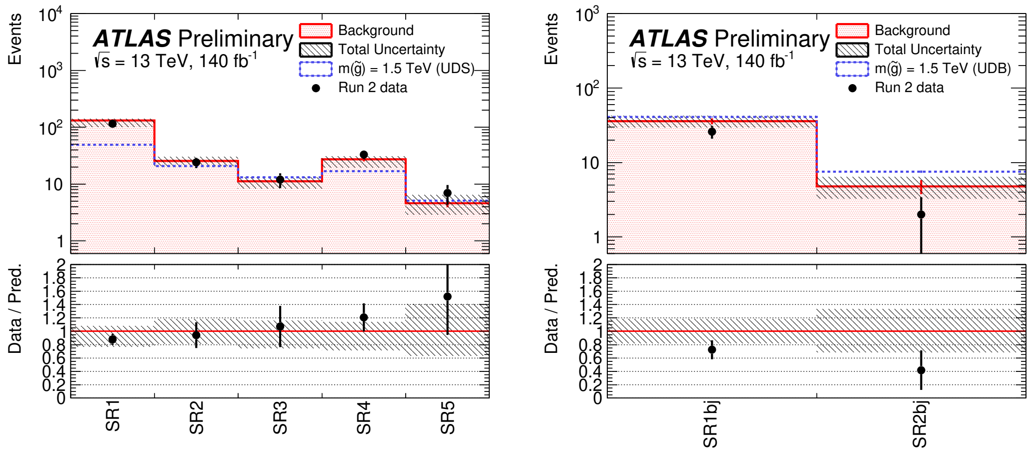

(a) **(b)**

Figure 7.9: Unblinded signal regions, defined in table 7.1. Figure (a) shows the regions targeting the UDS models, while (b) the ones for the UDB models with at least 2 *b*-tagged jets. The background is extrapolated from a jet multiplicity of 4, and with a CR at 60 GeV. The bottom panel shows the ratio of data over the predicted number of background events. In this panel, the red-shaded region represents the MC statistical error, the light-blue band is the MC theory error associated with the multijet fraction of the background while the light-green band is the one associated with the $t\bar{t}$ component. The yellow and purple bands are respectively the sums in quadrature of all the JES/JER errors, and the *b*-tagging systematic errors. The grey region is the combination of all these uncertainties.

obtained with at least 2 b-tagged jets in the event, keeping looser p_{T} and C cuts. Figures 7.8c and 7.8d show the impact of the additional b-tag requirement on some of the expected limit curves.

7.5 Results

The unblinded SR yields are shown in Figure 7.9. The observed yields are consistent with the predicted backgrounds within uncertainties so the limit setting procedure is used. The SR which provides the best expected sensitivity for a given gluino mass is used to set the limit. The exclusion limits for direct UDS and UDB decay models are shown in Figures 7.10a and 7.10b, respectively. Though there is good closure overall, an under fluctuation in the data yields for the direct decay UDB model regions

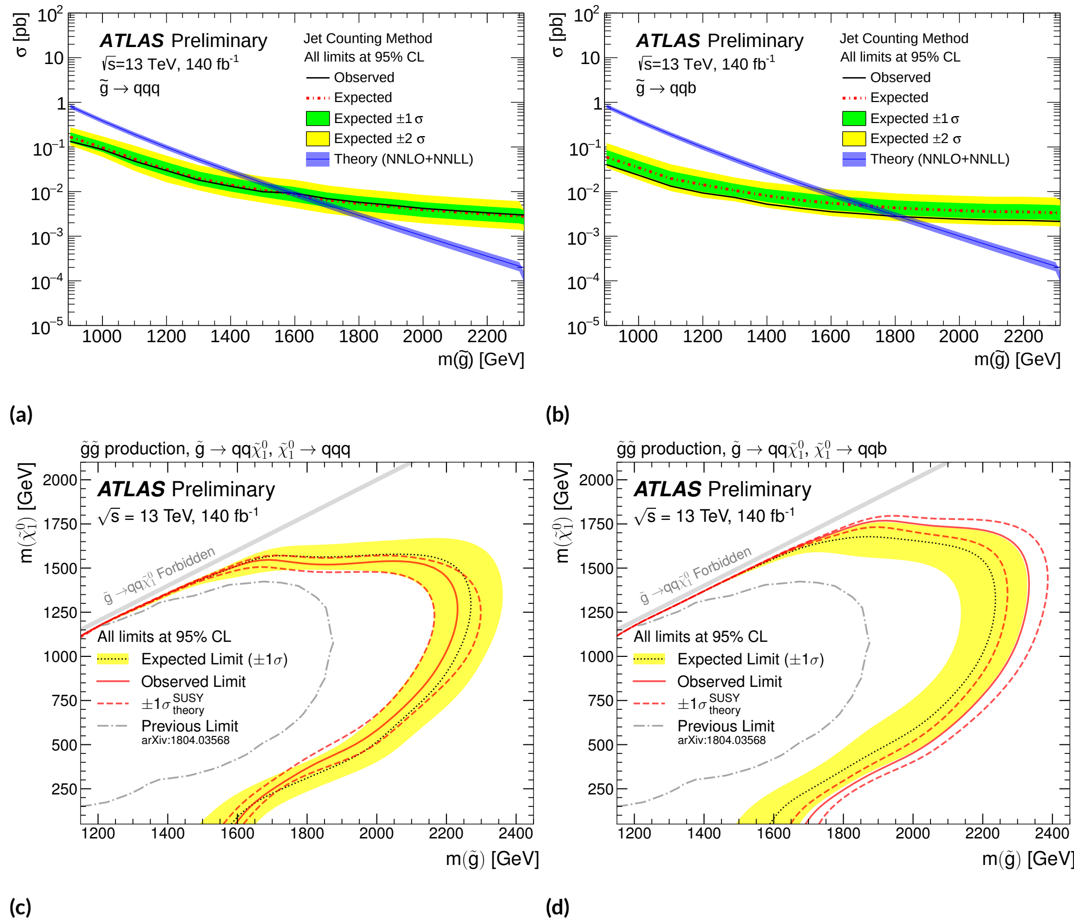

Figure 7.10: Expected and observed cross-section limits at a 95% CL for the direct decay UDS (a) and UDB models (b) as well as the cascade decay UDS (c) and UDB models (d).

led to a systematically stronger observed than expected limit as shown in Figure 7.10b. Likewise, the exclusion limits for the UDS and UDB cascade decay models are shown in Figures 7.10c and 7.10d, respectively. This result extends the exclusion on gluino masses from the previous ATLAS search [77] by around 700-800 GeV for the direct decay models and 500-600 GeV for the cascade models. The results are discussed further with the mass resonance method in the conclusions section.

Upper limits on the product of cross-section, acceptance, and efficiency are shown in Table 7.5 for

Signal region	$\langle\epsilon\sigma\rangle_{obs}^{95}$[fb]	S_{obs}^{95}	S_{exp}^{95}	CL_B	$p(s=0)$ (Z)
SR1	0.32	45	57^{+18}_{-14}	0.51	0.50 (0.00)
SR2	0.09	13	$14.1^{+5.7}_{-4.1}$	0.56	0.50 (0.00)
SR3	0.07	10	$9.5^{+4.1}_{-2.7}$	0.52	0.42 (0.20)
SR4	0.16	22	$17.4^{+6.5}_{-4.7}$	0.26	0.21 (0.79)
SR5	0.07	9.4	$7.4^{+3.6}_{-2.4}$	0.42	0.32 (0.46)
SR1bj	0.08	11	$17.0^{+6.9}_{-4.8}$	0.55	0.50 (0.00)
SR2bj	0.03	4.4	$6.6^{+2.9}_{-1.9}$	0.66	0.50 (0.00)

Table 7.5: The upper limit table for the signal regions for the jet counting method. Left to right: 95% CL upper limits on the visible cross section ($\langle\epsilon\sigma\rangle_{obs}^{95}$) and on the number of signal events (S_{obs}^{95}). The third column (S_{exp}^{95}) shows the 95% CL upper limit on the number of signal events, given the expected number (and $\pm1\sigma$ excursions on the expectation) of background events. The last two columns indicate the CL_B value, i.e. the confidence level observed for the background-only hypothesis, and the discovery p-value ($p(s=0)$).

the jet counting method. The same procedure is used to derive the limits except that the signal model hypothesis is removed and the contribution is allowed to float freely starting.

8

Mass Resonance Method

The mass resonance method aims to observe a localized excess in an invariant mass spectrum, an unambigious sign of new physics. To do so then one must *reconstruct* the event by deciding which of the pair produced particles each jet originates from. Historically, kinematic optimization techniques often based on the angular distance between jets were used. These techniques, however, are intractible at high multiplicities where the number of possible combinations is large and the kinematics of differ-

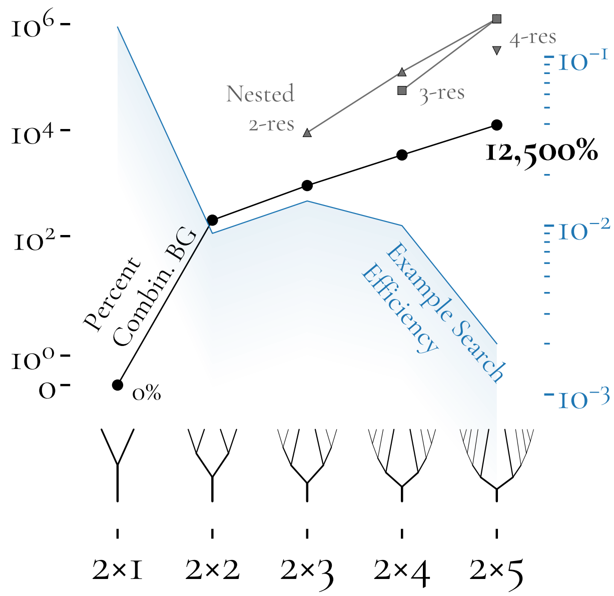

Figure 8.1: Percent combinatorial background given a brute-force analysis (black) is shown as a function of final-state multiplicity. Increased complexities from nested resonances are shown for various intermediate decays (grey). Example past search signal selection efficiencies are also shown (blue) for 1 TeV resonances from recent LHC searches [175–181].

ent choices are similar. This has been referrred to as the *combinatoric problem* of event reconstruction. Figure 8.1 illustrates the impact of the problem on experimental sensitivity, with the signal acceptance dropping off roughly with the final state multiplicity. Recently, machine learning methods that perform well on high dimensional tasks have been proposed in phenomology studies to solve this problem. Most of the studies have focused on reconstructing standard model processes [182–184], while there has been only one search study of pair production decaying to four jets [185]. The search scenario is considerably more challenging because the mass is not known apriori and must be scanned. Though foundational, these studies did not consider the background shape, estimate, or fitting methodology which are essential in practice. This thesis is the first experimental result with such a technique.

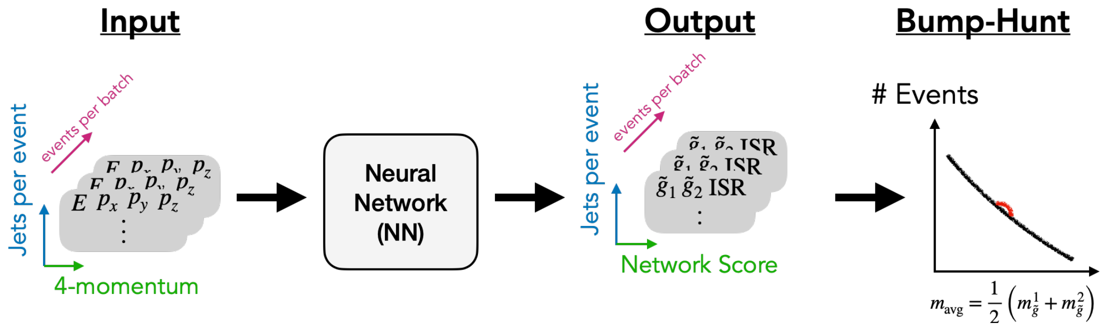

Figure 8.2: Overview of the mass resonance analysis. The jet 4-momentum are fed into a neural network that returns the per jet probability (score) to originate from either gluino or non-signal source. Using the predictions, the jet 4-momenta are added together to make the gluino invariant mass spectrum to perform a bump hunt on.

8.1 Strategy

The method strategy is shown pictorially below in Figure 8.2. Beginning on the left side of Figure 8.2, the calibrated jet 4-momentum are fed into a Neural Network (NN). The output of the NN is 3 numbers per jet that represent the probability to originate from either of the gluinos or a different source (ISR/pileup). The maximum score per jet is used to group the jets and then the 4-momenta of all jets within a grouping is summed to form candidate gluino 4-momenta. Lastly, a bump hunt is performed on the average invariant mass spectrum $m_{\text{avg}} = \frac{1}{2}\left(m^1_{\tilde{g}} + m^2_{\tilde{g}}\right)$ using a profile likelihood ratio test to compare background only and signal plus background hypotheses. The background is estimated using a fit to the smoothly falling mass spectrum. Similar event selections are applied as the jet counting method to reduce the multijet background, requiring at least 6 jets with $p_{\text{T}} \geq 100$ GeV and $C \geq 0.9$. In the next sections the selections are applied unless mentioned otherwise. The following subsections provide technical details about the model, training procedure, performance, background estimate technique, and bump hunt.

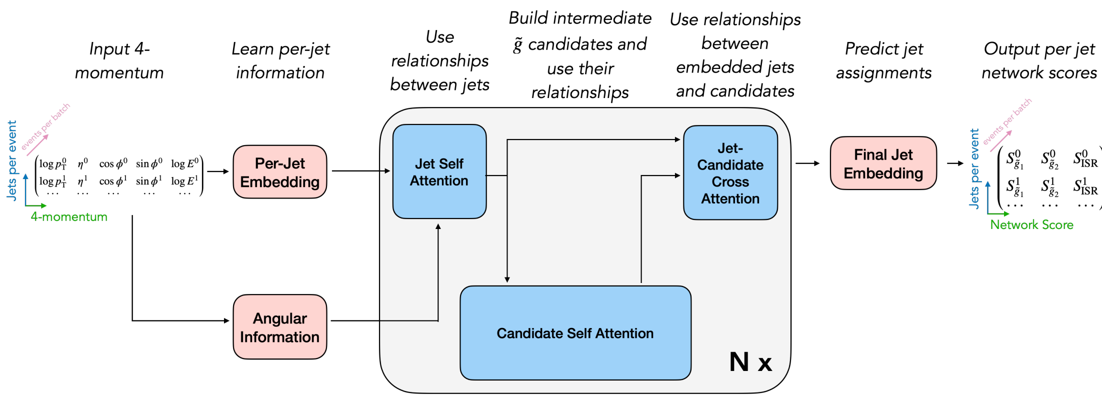

Figure 8.3: Overview of methodology to predict candidate parent ($\tilde{g}$) 4-momentum from jet 4-momentum by using a NN to predict jet pairings. The important conceptual goals of each block are displayed above in text.

8.2 Model

The goal of the architecture design was to make a model that is computationally expressive, capable of processing variable number of jets, and permutation invariant with respect to the input jets as well as the candidate gluinos. Similar objectives have existed in other fields such as natural language processing and protein structure prediction, leading to the attention mechanism that is now used in many generative pretrained transformers [186–188]. Though these techniques are not yet used extensively by ATLAS, it was hypothesized that the attention mechanism could be adapted to tackle the combinatoric problem. The performance of the resulting model outlined in Figure 8.3 confirms that hypothesis.

The model was built from basic computational units referred to as Embedding Block (EB) and Attention Block (AB), which can be seen shaded tan and blue, respectively, in Figure 8.3. These blocks are composed of widely available modules in the PyTorch package [189] as shown in Figure 8.4.

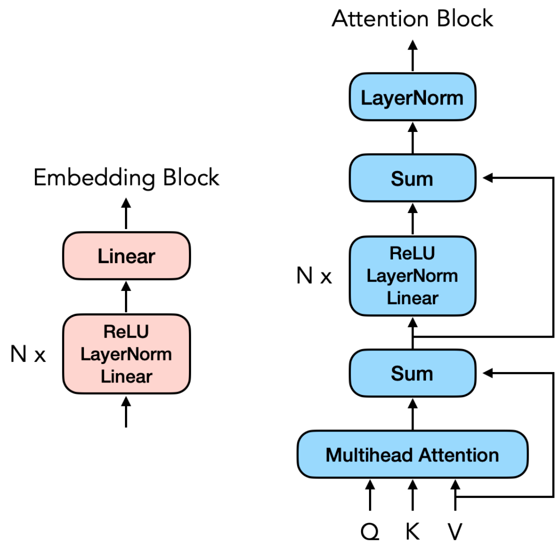

Figure 8.4: The basic model blocks called the Embedding Block (left) and Attention Block (right).

Embedding block: This block learns an embedding from $\mathbb{R}^d \to \mathbb{R}^{d'}$. The input is a d-dimensional vector and the output is d' dimensional vector. This accomplished through repeated applications of the transformation

$$x^{'} = \text{ReLU}\left(\text{LayerNorm}\left(Ax + b\right)\right), \tag{8.1}$$

where A and b are learned matrices, LayerNorm applies normalization over the input, and ReLU is the rectified linear unit function [190]. The final layer is an optional Linear unit so that the output is not constrained to be positive, which a ReLU would have done. Psuedocode is supplied in Algorithm 1, where the subscripts indicate valus that are learned throughout training and N_l is the number of stacked blocks as in Figure 8.4.

Algorithm 1 Embedding Block

function EmbeddingBlock(x)
    Input $x \in \mathbb{R}^d$ ▷ Input d-dim vector
    if Normalize Input **then**
        $x \leftarrow \frac{x - \mathrm{E}_b[x]}{\sqrt{\mathrm{Var}_b[x]+\epsilon}} * \gamma_b + \mathrm{B}_b$ ▷ Optional BatchNorm(x)
    end if
    for i in N_l **do** ▷ Loop over N_l stacked Linear blocks
        $x \leftarrow A_i x + b_i$ ▷ Linear(x)
        $x \leftarrow \frac{x - \mathrm{E}_i[x]}{\sqrt{\mathrm{Var}_i[x]+\epsilon}} * \gamma_i + \mathrm{B}_i$ ▷ LayerNorm(x)
        $x \leftarrow \max(0, x)$ ▷ ReLU(x)
    end for
    if Apply Final Linear **then**
        $x \leftarrow A_f x + b_f$ ▷ Optional Linear(x)
    end if
    Return $x \in \mathbb{R}^{d'}$ ▷ Output d'-dim vector
end function

Attention block: This block learns relationships between objects most often embedded into latent dimensions. The attention mechanism is best understood by reading Section 3 of Ref. [186]. The attention function is a mapping from a query and a set of key-value pairs to an output, where all three inputs are vectors. The output is a weighted sum of the values, with the weights computed from a compatibility function between the query and keys. The type of attention deployed here is called Scaled Dot-Product Attention which uses the dot product as the compatibility function

$$\mathrm{Attention}\left(Q, K, V, \Lambda\right) = \mathrm{softmax}\left(\frac{QK^T}{\sqrt{d_k}} + \Lambda\right) V, \tag{8.2}$$

where the factor of d_k is the key dimension used to regulate how large the dot product can grow, Q is called the query, K is called the key, V is called the value, and Λ is a bias term that can be added

Algorithm 2 Attention Block

function AttentionBlock(Q, K, V, Λ)
  Input $Q \in \mathbb{R}^{d \times d_k}$, Key $K \in \mathbb{R}^{d' \times d_k}$, Value $V \in \mathbb{R}^{d' \times d_v}$, Bias Λ
  for i in N_{attn} **do** ▷ Loop over N_{attn} stacked blocks
    $x \leftarrow \text{MultiHeadAttention}(Q, K, V, \Lambda)$ ▷ Attention
    $x \leftarrow x + V$ ▷ Skip connection
    $\text{resid} \leftarrow x$ ▷ Prepare Skip connection
    $x \leftarrow \text{Embedding(x)}$ ▷ Embedding Alg. 1
    $x \leftarrow x + \text{resid}$ ▷ Skip connection
    $x \leftarrow \frac{x - \text{E}_i[x]}{\sqrt{\text{Var}_i[x] + \epsilon}} * \gamma_i + \text{B}_i$ ▷ LayerNorm(x)
  end for
  Return $x \in \mathbb{R}^{d \times d_v}$
end function

to the attention weights or set to zero. Noteable properties of the attention mechanism is that it is permutation invariant with respect to the inputs, expressive computationally with a message passing like information flow, optimizable via back propagation, and efficient since its model graph is highly parallizeable onto compute architectures as a result of being broad but not deep. After the attention mechanism, further embeddings are used to extract and utilize the information progressively. Psuedocode is supplied in Algorithm 2, where N_{attn} is the number of stacked blocks as in Figure 8.4.

8.2.1 Walkthrough

To best understand the transformations applied by the model below is a walkthrough from input to output, following Figure 8.3. The important variables are the number of input jets J, input features F, per-jet embedding dimension E, and number of target objects T. For the direct decay model $J = 8$ jets, $F = 4$ for the four-momenta, and $T = 3$ for the two gluinos and ISR.

Input: The input to the network is the 8 leading jets stacked in a matrix. If an event has less than 8 jets it is padded with rows of zeros. The matrices are preprocessed as

$$x = \begin{pmatrix} \log p_{\mathrm{T}}^0 & \eta^0 & \cos\phi^0 & \sin\phi^0 & \log E^0 \\ \log p_{\mathrm{T}}^1 & \eta^1 & \cos\phi^1 & \sin\phi^1 & \log E^1 \\ \ldots & \ldots & \ldots & \ldots & \ldots \end{pmatrix}, \tag{8.3}$$

ensuring that the input are of similar magnitude and the azimuthal angle avoids ambigiuties from 2π rotations. Fixed size matrices are used because of hardware constraints.

Per-Jet Embedding: Each jet, is fed into the same EB. The number of dimensions is increased from $\mathbb{R}^5$ to $\mathbb{R}^E$, with $E = 32$ for the final model. Using the same EB preserves permutation invariance.

$$x \leftarrow \mathrm{EmbeddingBlock}(x) \in \mathbb{R}^{\mathrm{J}\times\mathrm{E}} \tag{8.4}$$

Angular Information: The pairwise angular distance between all jets is cast into a latent space as

$$\Lambda \leftarrow (\Delta\eta, \Delta\cos\phi, \Delta\sin\phi) \in \mathbb{R}^{\mathrm{J}\times\mathrm{J}\times 3} \tag{8.5}$$

$$\Lambda \leftarrow \mathrm{EmbeddingBlock}(\Lambda) \in \mathbb{R}^{\mathrm{J}\times\mathrm{J}} \tag{8.6}$$

where J is the number of input jets and 3 is the anglur dimension from (η, $\cos\phi$, $\sin\phi$). This 3-dimension tensor is cast down to a single dimension then used as a bias term in the Jet Self Attention.

Jet Self Attention: Attention between the embedded jets per event with the embedded pariswise angular distance used as a bias. The keeps the dimensionality of the input the same $\mathbb{R}^{\mathrm{J}\times\mathrm{E}} \to \mathbb{R}^{\mathrm{J}\times\mathrm{E}}$.

$$x \leftarrow \mathrm{AttentionBlock}(x, x, x, \Lambda) \in \mathbb{R}^{\mathrm{J}\times\mathrm{E}} \tag{8.7}$$

Candidate Self Attention: Candidate gluinos are built by interpretting arbitrarily the first three dimensions per jet as jet-assignment scores. During evaluation the maximum score is taken per jet to decide which source the jet comes from. However, while training this is not possible since the maximum is not differentiable so the scores are converted to roughly discrete choices using the Gumbel-Softmax which applies a sampling of the softmax probability distribution. The candidates are built by adding (via matrix multiplication) the jet groups, producing latent space candidates. Lastly, attention is applied between the candidates without any angular bias term.

$$c \leftarrow \mathrm{GumbelSoftmax}(x[:, :3]) \in \mathbb{R}^{\mathrm{J}\times 3} \tag{8.8}$$

$$c \leftarrow c^{\mathrm{T}} \times x \in \mathbb{R}^{3\times\mathrm{J}} \times \mathbb{R}^{\mathrm{J}\times\mathrm{E}} = \mathbb{R}^{3\times\mathrm{E}} \tag{8.9}$$

$$c \leftarrow \mathrm{AttentionBlock}(c, c, c) \in \mathbb{R}^{3\times\mathrm{E}} \tag{8.10}$$

Jet-Candidate Cross Attention: Apply attention with Q equal to embedded jets post attention while both key, value equal to the candidate objects post attention, and without any bias term.

$$x \leftarrow \mathrm{AttentionBlock}(x, c, c) \in \mathbb{R}^{\mathrm{J}\times\mathrm{E}} \tag{8.11}$$

Final Embedding: Each embedded jet is fed into the same EB for a final embedding. The number of dimensions is decreased from $\mathbb{R}^E$ to $\mathbb{R}^3$, with $E = 32$ for the final model and 3 from the number of target parents. The outputs of this block are the predicted scores per jet.

$$x \leftarrow \text{EmbeddingBlock}(x) \in \mathbb{R}^{\text{J}\times 3} \tag{8.12}$$

Ouput Scores to m_{avg}: The final predictions are three numbers per jet corresponding to the confidence the jet arose dominantly from either gluino or a different source. Once the network scores are predicted, then the rest of the postprocessing occurs outside of the model. The max score per jet is the predicted assignment. Then the 4-momentum of all jets assigned to each parent are added together to form the predicted gluino 4-momentum.

$$c^\mu \leftarrow \text{ArgMax}(x)^T \times P^\mu \in \mathbb{R}^{3\times \text{J}} \times \mathbb{R}^{\text{J}\times 4} = \mathbb{R}^{3\times 4} \tag{8.13}$$

$$\tilde{g}_0^\mu, \tilde{g}_1^\mu, \text{ISR}^\mu = c_0^\mu, c_1^\mu, c_2^\mu \tag{8.14}$$

where P^μ is the matrix of jet 4-momentum in (E, p_x, p_y, p_z) basis. Lastly, the gluino invariant masses are computed to give the average mass spectrum.

$$m_{\tilde{g}} = \tilde{g}^\mu \tilde{g}_\mu \tag{8.15}$$

$$m_{\text{avg}} = \frac{1}{2}\left(m_{\tilde{g}}^0 + m_{\tilde{g}}^1\right) \tag{8.16}$$

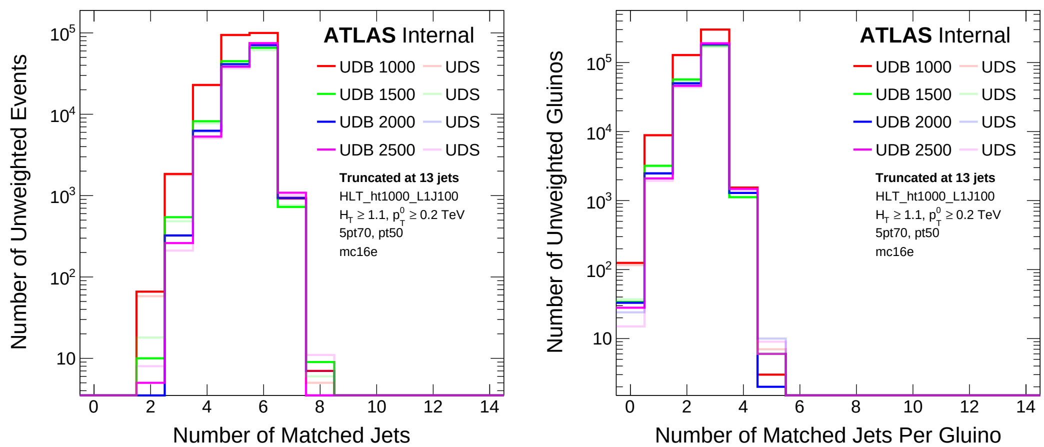

Figure 8.5: Number of jets matched per event (left) and per gluino (right).

8.2.2 Training

The target labels were made per event by matching jets to truth partons, with the minimum $\Delta R \leq 0.4$ match chosen. If there was no match then the jet was assumed to originate from ISR or pileup. Multiple jets were allowed to be matched to the same parton, providing groups of jets that were associated to each $\tilde{g}$. The number of matched jets per event and per $\tilde{g}$ are shown in Figure 8.5.

The training set is made to be close to the target signal region – all events that pass the trigger selection, leading jet pt, at least six jets with p_{T} above 100 GeV, and $C \geq 0.8$. Only events with exactly 3 jets matched per gluino were used in training since the ΔR matching gave worse mass resolution with variable number of jets. To reduce background sculpting and create a smooth model throughout the targeted mass range, all mass points were trained on simultaneously. As shown in Figure 8.5, there are at most 8 matched jets and any tighter selection will only reduce this number. Therefore, for training the events are truncated at 8 jets. Any event with fewer is padded with 0's.

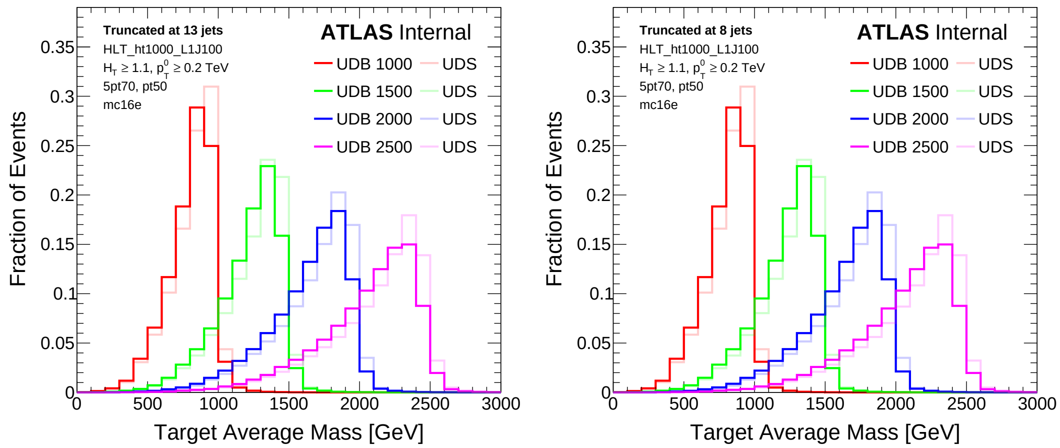

Figure 8.6: Target mass distribution for 2x3 UDB (bold) and UDS (light) models. The mass distribution with number of jets truncated at 13 (left) versus at 8 (right). There is no difference between the plots because the number of matched jets stops at 8 as shown in Figure 8.5.

The total training set size with all mass points is roughly 1.73 million events, with 90% of the dataset used for training and 10% for validation. Each training batch consisted of 2048 events. The training set uses a pileup profile modeled on the 2018 data and labeled as MC16e. Alternative MC samples with the pileup profile varied to represent the 2015–2016 and 2017 datasets were used to test the dependence on the profile and are labeled MC16a and MC16d, respectively. The model was trained using CUDA 11.6, PyTorch 1.13.1, and PyTorch Lightning 2.0.0 [189, 191, 192].

Hardware and Schedule: The model was trained using 8 CPU cores and an NVIDIA Quadro RTX 4000 for 500K steps or roughly 14 hours. Shorter trainings for hyperparameter optimization used 16 CPU cores and an NVIDIA A100.

Optimizer: The Adam optimizer with $\beta_1 = 0.9$, $\beta_2 = 0.999$, $\epsilon = 1\text{e}{-}08$, and $\lambda = 0$ was used. The learning rate (lr) was ramped up linearly to a maximum value of lr_{max} over the first N steps and

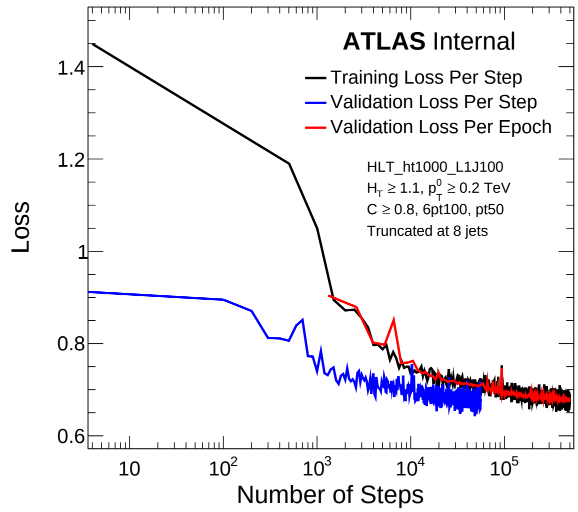

Figure 8.7: The training loss per step (black), validation loss per step (blue), and validation loss per epoch (red). The validation loss step 0 occurs after roughly 10^3 training steps. The validation loss epoch is logged at the end of each validation epoch. The number of events in the training and validation set is different ($90 : 10\%$ split) so the number of steps is different for the three curves. The drop in the loss corresponds to when the network has found an optimal gradient descent, which typically happens when the learning rate warm up phase has ended.

then decayed exponentially by ϵ every N steps for the remainder of the training:

$$\mathrm{lr_{step}} = \mathrm{lr_{max}} \times \begin{cases} \frac{\mathrm{step}}{\mathrm{N}} & \mathrm{step} \leq \mathrm{N} \\ \alpha^{\,\mathrm{step//N}} & \mathrm{else}, \end{cases} \tag{8.17}$$

with $\mathrm{lr_{max}} = 1\mathrm{e}{-3}$, $\mathrm{N} = 2\%$ of the total number of steps, and $\alpha = 0.95$. The model weights were updated on each training step.

Loss Function: The loss function is the sum of a cross entropy loss on the final output L_M and auxiliary losses per repeated block. The loss is symmetrized by taking the minimum loss per event with the jet grouping swapped between gluino's. The strength of the auxiliary term is scaled via λ_{aux}

to favor the final network output, with $\lambda_{\text{aux}} = 0.25$ used for the final model.

$$L = L_{\text{M}} + \lambda_{\text{aux}} L_{\text{aux}} \tag{8.18}$$

$$L_{\text{M}} = \min_{\tilde{g}_0 \leftrightarrow \tilde{g}_1} \text{CrossEntropyLoss}\left(\hat{y}, y\right) \tag{8.19}$$

$$L_{\text{aux}} = \frac{1}{N-1} \sum_{i=0}^{N-1} L_{\text{M}}^{i}, \tag{8.20}$$

where i is a sum over the attention blocks up until the final one. The training and validation loss curves are shown in Figure 8.7.

Hyperparameters: First, by hand we changed the hyperparameters until decent performance was found. Then using those hyperparameters as initial values performed a population based scan with nearby values to pick the model with minimum validation loss [193, 194]. The embedding dimension, number of attention blocks, learning rate, and batch size were scanned over. The model parameters selected are summarized in Table 8.1.

After modest hyperparameter tuning it was found that the final sensitivity is statistically limited as a result of the kinematic event selections, rather than by the model performance. This was found by replacing the predicted signal distribution with the target signal distribution, leaving the background as the predicted spectrum, in the statistical analysis. This swap did not significantly improve the sensitivity. If additional hyperparameter tuning could shift the predicted background spectrum towards smaller values then this would be worthwhile but it was not found to be achievable with the current methodology.

Name	Value
Embedding Input Dimensions	5
Embedding Dimension	32
Embedding MLP # Layers	3
MLP Input Dim	3
MLP # Nodes	32
MLP # Layers	3
# Attention Blocks	4
# Heads per Attention Block	4
Atention Block MLP # Nodes	32
Out Dim	3
Gumble Softmax τ	1
Gumble Softmax Hard	On
Precision	16-bit Mixed
Gradient Clip	0.1

Table 8.1: Table of the used model parameters.

8.2.3 Performance

The confusion matrix of the test set is shown in the Figure 8.8. Along the x-axis is the predicted label, y-axis is the target label, and z-axis is the number of jets per million. First, this verifies that padded jets are always labeled as padded. Second, that the symmetric loss ensures that there is not a preference to label objects as $\tilde{g}_1$ or $\tilde{g}_2$. Third, the number of times a jet is mislabeled as ISR or signal, respectively, is non-negligble.

The fraction of events with $\geq N$ correctly labelled jets (taking into account $\tilde{g}$ swapping) is shown in Table 8.2. Approximately 50% of events have at least 6 correctly matched jets. To compute this number, first the number of jets matched to $\tilde{g}_1$ and $\tilde{g}_2$ is computed. Then the collection of jets are swapped between the gluinos, the number is recomputed, and the maximum accuracy taken. The accuracies are computed inclusively for $\geq N$ jets. The dropoff going from 6 to 7 jets is from softer jets that have less destinctive impacts on the energy flow and mass peaks migrating between the parents.

In general, the performance is good enough to reconstruct mass peaks as shown in Figure 8.9, com-

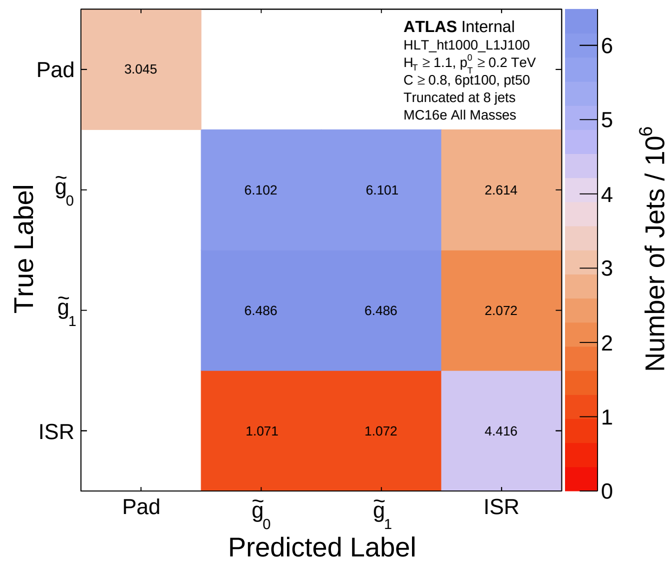

Figure 8.8: Confusion matrix for the model evaluated trained on mc16e and evaluated on independent test set mc16d.

paring the predicted vs target spectrums. All pileup profile variations are included with negligble differences between the generations observed. Mislabeling by either swapping jets between gluinos or with an ISR jet results in a broadening of the mass distribution. Some radiation is also lost by truncating at 8 jets, sharing radiation between jets, and reconstruction inefficiency which shifts the mass peaks below their true values.

The UDB model contains two b-quarks at parton level. Therefore, an additional selection on the number b-tagged jets with the DL1r 77% WP tagger [195] is used. Figure 8.10 shows the m_{avg} distribution with at least 1 or 2 b-tags. The ≥ 1 selection is used to maintain sufficient acceptance.

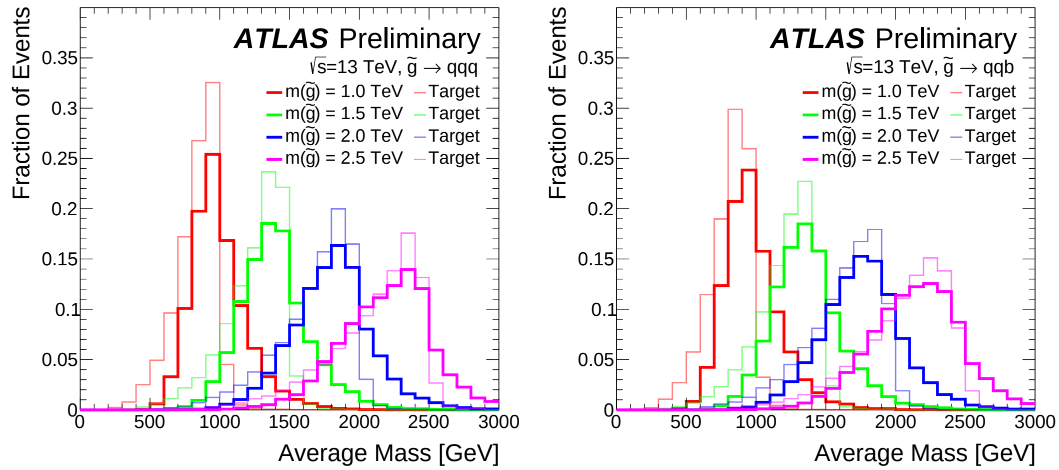

Figure 8.9: Normalised average mass spectrum comparing the shapes of the reconstructed (solid) and target (light) distributions for different masses. The reconstructed distribution is produced using the NN assignments, whereas the target distribution is built assigning jets to gluinos based on their truth labels.

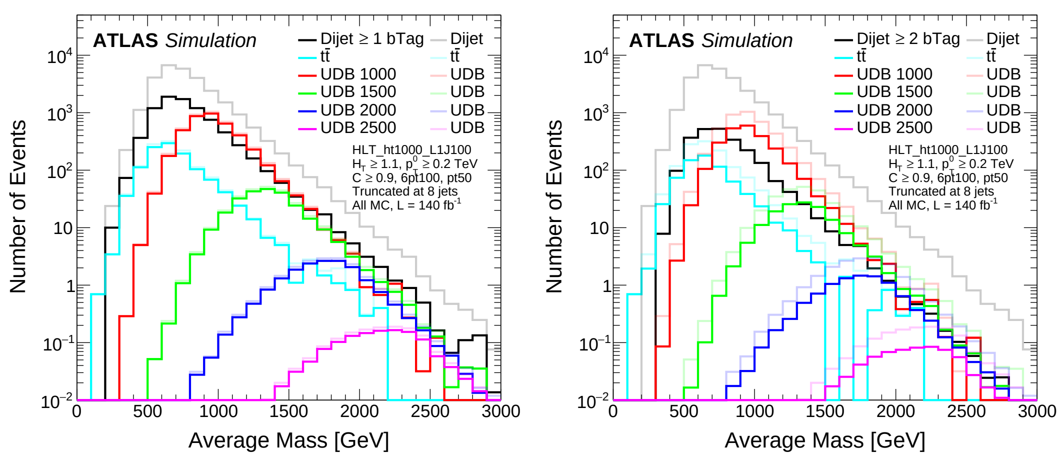

Figure 8.10: Predicted mass distribution on all MC campaigns for multijets (black), $t\bar{t}$ (blue), UDB with number of btagged jets selection (solid colors), and all curves without btag selection (light colors).

sample	≥0	≥1	≥2	≥3	≥4	≥5	≥6	≥7	=8
UDB 900	1.00	1.00	1.00	0.98	0.94	0.68	0.50	0.13	0.11
UDB 1000	1.00	1.00	1.00	0.98	0.94	0.69	0.51	0.14	0.11
UDB 1100	1.00	1.00	1.00	0.98	0.94	0.70	0.52	0.14	0.11
UDB 1200	1.00	1.00	1.00	0.98	0.94	0.71	0.53	0.15	0.12
UDB 1300	1.00	1.00	1.00	0.98	0.95	0.72	0.54	0.15	0.12
UDB 1400	1.00	1.00	1.00	0.98	0.95	0.72	0.54	0.16	0.12
UDB 1500	1.00	1.00	1.00	0.98	0.95	0.72	0.55	0.16	0.13
UDB 1600	1.00	1.00	1.00	0.98	0.95	0.72	0.55	0.16	0.12
UDB 1700	1.00	1.00	1.00	0.98	0.95	0.73	0.55	0.17	0.13
UDB 1800	1.00	1.00	1.00	0.98	0.95	0.73	0.56	0.17	0.13
UDB 1900	1.00	1.00	1.00	0.98	0.96	0.73	0.56	0.17	0.13
UDB 2000	1.00	1.00	1.00	0.99	0.96	0.74	0.57	0.18	0.13
UDB 2100	1.00	1.00	1.00	0.99	0.96	0.75	0.58	0.18	0.14
UDB 2200	1.00	1.00	1.00	0.99	0.96	0.75	0.58	0.19	0.14
UDB 2300	1.00	1.00	1.00	0.99	0.96	0.75	0.58	0.20	0.14
UDB 2400	1.00	1.00	1.00	0.99	0.96	0.76	0.59	0.20	0.14
UDB 2500	1.00	1.00	1.00	0.99	0.96	0.76	0.59	0.20	0.14
UDS 900	1.00	1.00	1.00	0.98	0.94	0.69	0.50	0.14	0.11
UDS 1000	1.00	1.00	1.00	0.98	0.94	0.70	0.52	0.15	0.12
UDS 1100	1.00	1.00	1.00	0.98	0.95	0.71	0.53	0.16	0.12
UDS 1200	1.00	1.00	1.00	0.98	0.95	0.72	0.54	0.17	0.13
UDS 1300	1.00	1.00	1.00	0.98	0.95	0.72	0.55	0.17	0.13
UDS 1400	1.00	1.00	1.00	0.98	0.95	0.73	0.55	0.18	0.14
UDS 1500	1.00	1.00	1.00	0.98	0.95	0.73	0.56	0.18	0.14
UDS 1600	1.00	1.00	1.00	0.98	0.95	0.73	0.56	0.18	0.14
UDS 1700	1.00	1.00	1.00	0.98	0.95	0.73	0.56	0.19	0.14
UDS 1800	1.00	1.00	1.00	0.99	0.96	0.74	0.57	0.19	0.14
UDS 1900	1.00	1.00	1.00	0.99	0.96	0.74	0.58	0.20	0.15
UDS 2000	1.00	1.00	1.00	0.99	0.96	0.75	0.58	0.21	0.15
UDS 2100	1.00	1.00	1.00	0.99	0.96	0.76	0.59	0.21	0.15
UDS 2200	1.00	1.00	1.00	0.99	0.96	0.76	0.59	0.22	0.16
UDS 2300	1.00	1.00	1.00	0.99	0.96	0.76	0.60	0.22	0.16
UDS 2400	1.00	1.00	1.00	0.99	0.96	0.76	0.59	0.22	0.16
UDS 2500	1.00	1.00	1.00	0.99	0.96	0.77	0.60	0.23	0.16
ALL 1800	1.00	1.00	1.00	0.98	0.95	0.72	0.55	0.16	0.12
ALL 2200	1.00	1.00	1.00	0.99	0.96	0.75	0.58	0.18	0.13

Table 8.2: Fraction of events with ≥N correct jet labels per sample.

8.3 Background Estimate

A data-driven method is used to estimate the SM background by fitting the m_{avg} spectrum with a function. This is possible because the predicted mass spectrum is observed to be smoothly falling and thus can be parameterized. Two function families were considered:

- N-parameter polynomial: $f(x) = p_0 \, (1 - x)^{\sum_{i=1}^{N} p_i (\log x)^i}$
- N-parameter exponential: $f(x) = e^{p_0 x} \left(\sum_{i=1}^{N} p_i x^i \right)$,

where $x = m_{\text{avg}}/\sqrt{s}$ and p_i are the fit parameters. To reduce the parameter correlations and stabilize the fit, the functions are normalized such that p_0 controls the scale. This is only feasible for the 2 and 3 parameter functions since the higher order ones have increasingly complex integrals.

The fits were tested on 2015 data with looser selections such that the number of events is similar to the Pythia 8 Multijet MC sample normalized to $140\,\text{fb}^{-1}$, which is representative of the stats expected in the full dataset. The 2015 data sample is preferred for testing because the associated uncertainties of the MC sample are highly dependent on the event weights, with large weights leading to misrepresentative uncertainties. Meanwhile the data sample has more reasonable uncertainties, at the cost of limited stats at the tail of the m_{avg} spectrum. The looser selections are reasonable because the shape of the multijet spectrum is similar at different inclusive C selections as shown in Figure 8.11.

The fit region is set from 0.7 – 3 TeV. The lower edge is chosen so that the multijet spectrum is smoothly falling as shown in Figure 8.10. The upper edge is chosen to include the largest signal mass where there is sensitivity and there is still some stats. Figure 8.12 shows the results of likelihood and

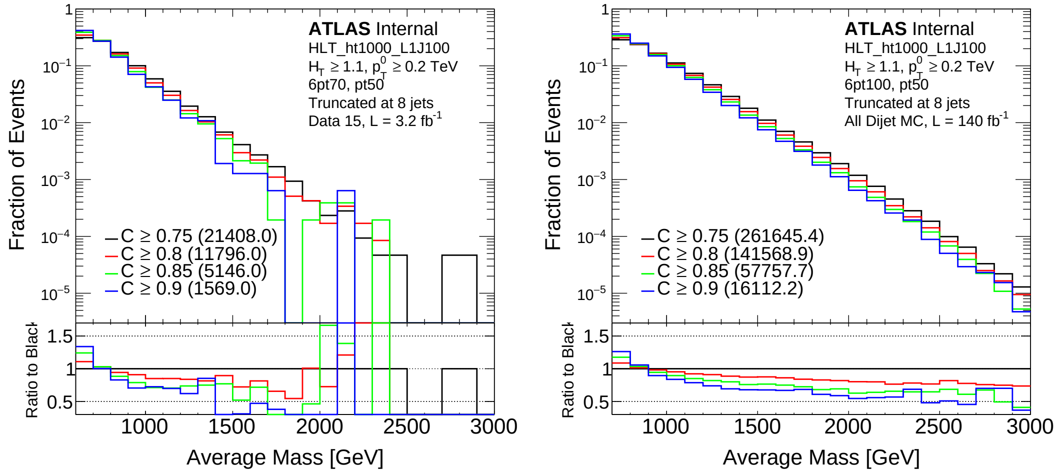

Figure 8.11: The normalized predicted average mass distribution of 2015 data with looser selections (left) and multijet MC sample normalized to 140 fb^{-1} (right) as a function of inclusive C selections.

χ^2 based background only fits to data and multijet MC, respectively. The top panel is the predicted distribution in black and fit in green. The bottom panel is the significance equal to (Data - Fit)/Total Error, where Total Error is the sum in quadrature of the Poisson $\sqrt{N}$ of data and the fit error.

The following criteria were used to determine which function to use.

1. The background fit must have a small $\chi^2/N_{\mathrm{D.O.F.}}$ and probability $1 - P(k/2, \chi^2/2) > 0.1$.
2. The *spurious signal* contribution is $\mu_{\mathrm{Sp}} < 20\%$ or $\mu_{\mathrm{Sp}}/\sigma_{\mathrm{Sp}} < 20\%$, as explained further below. Each N parameter function is checked with the N+1 parameter function within the same family and the N parameter function of the alternative family fits to 2015 data.
3. The function with the lowest number of parameters is chosen since that has less freedom to absorb potential signal and thus has the best sensitivity.
4. If one function from each family remains then the more sensitive and stable is chosen.

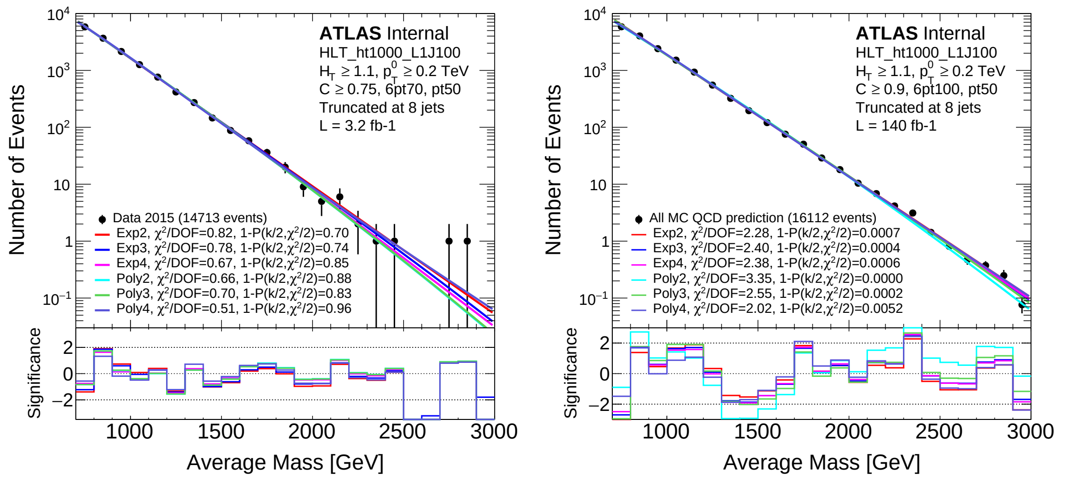

Figure 8.12: Fitted background functional form for data 2015 with C$\geq$ 0.7 and 6pt70 (left). Fitted distribution for all the MC normalized to 140 fb^{-1} with C$\geq$ 0.9 and 6pt100 (right).

The spurious signal contribution μ_{Sp} is defined as the extracted signal strength from an S+B fit when data is background only. If the background function is known exactly then the prediction would be match data, yielding $\mu_{\text{Sp}} = \mu_S = 0$. In practice a nonzero μ_{Sp} is found. Therefore, the spurious signal quantifies the degree to which a background function is able to spuriously create a signal or absorb a signal that is actually there. This is a quantitative way to qualify the fact that the correct background function is not known.

All considered functions pass the first criteria as shown in the left panel of Figure 8.12. The 2 parameter functions do not pass the spurious signal checks. The 3 and 4 parameter functions pass the spurious signal checks for the mass range roughly up to 2 TeV, which is at the limit of the statistical sensitivity. Therefore, the two 3 parameter functions are considered. The 3 parameter exponential is unstable during S+B fits, meaning that small changes in the parameter could yield dramatically different results during optimization. Therefore, the normalized 3-parameter polynomial is chosen.

Two additional tests are done to further validate the functions. First, spurious signal tests are done to validate that random fluctuations of the fitted data do not generate large spurious signals through S+B fits on psuedodata sets with poisson variations per bin. Second, signal injection tests are done to verify that a B only fit to the background function cannot absorb S+B data. The figures are omitted here since they are better discussed in the internal note.

8.4 Uncertainties

8.4.1 Modeling

As in the jet counting method, there are systematic effects on the final result from the physics modeling. However, since the background estimate is entirely data driven, there are no uncertainties from using multijet MC. The uncertainties affecting the signal model are those modifying the event weights to test the renormalization scale, factorization scale, α_S value, and PDF uncertainties as discussed in Section 7.3.1. They are included using the ratio of the re-weighted to nominal spectrums and NPs in the final fit. One-sided uncertainties are symmetrized to stabilize the likelihood minimization.

8.4.2 Experimental

Experimental uncertainties for the scale factor variations, JES, JER, and luminosity variations as discussed in Section 7.3.2 are included. The event kinematics are affected by these variations, so the model is re-evalauted to produce new mass spectrums.

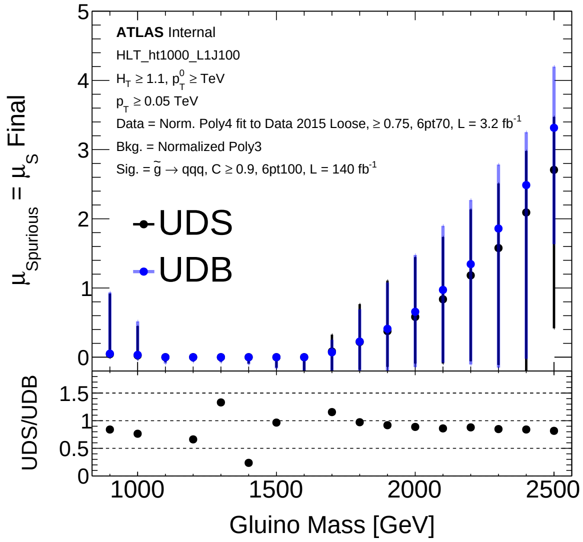

Figure 8.13: The spurious signal systematic per mass point derived from fitting the nominal 3 parameter polynomial function to the 4 parameter function evaluated at each bin center. The 4 parameter function is fitted to 2015 data with looser selections on the C-parameter and the jet p_{T}'s.

8.4.3 Methodology

The systematics from the methodology are entirely from the uncertainty on the choice of background function and its fit. First, uncertainties on the parameters of the fitting function are included in the fit minimization. Second, the uncertainty from the choice of background function is quantified with the spurious signal systematic as defined previously. The value is derived from an S+B fit with the data set equal to a 4 parameter fit to data 2015 and the background function set equal to the nominal 3 parameter function The uncertainty is included with a Gaussian prior for μ_{Sp} such that the contribution starts at 0 and can be pulled to ± 1 times its contribution. This is implemented as a negative plus a positive contribution. The positive term has a Gaussian prior that starts at 1 which produces net 0 spurious signal contribution

$$\lambda = s_i\mu + b_i(\vec{p},\vec{\theta}) + N_{\mathrm{Sp}} = s_i\mu + b_i(\vec{p},\vec{\theta}) + s_i\mu_{\mathrm{Sp}}\left(\theta_{\mathrm{Sp}} - 1\right) \tag{8.21}$$

where θ_{Sp} is a Gaussian nuisance parameter. As the nuisance parameter moves, the contribution becomes nonzero. The distribution of μ_{Sp} is shown below in Figure 8.13. Lastly, no additional systematic is applied for the actual NN because it simply chooses an arbitrary combination of the jet 4-momenta, meaning it may produce imperfect reconstruction but not an unaccounted for bias.

8.5 Statistical Analysis

A bump hunt is performed on the m_{avg} spectrum using a profile likelihood ratio to test background only and signal plus background hypotheses. The likelihood function is the product of Poisson terms for the bin yields and Gaussian terms for the nuisance parameters of the systematic uncertainties:

$$\begin{aligned} L\left(\lambda\right) &= \mathrm{Poisson} \times \mathrm{Gaussian} && (8.22)\\ &= \prod_{i}^{\mathrm{Nbins}} \mathrm{Poisson}\left(k = n_i; \lambda\right) \prod_{\theta_i}^{\vec{\theta}} \mathcal{N}\left(\mu = 0, \sigma = \sigma_\theta\right) && (8.23)\\ &= \prod_{i}^{\mathrm{Nbins}} \frac{\lambda^{n_i} e^{-\lambda}}{n_i!} \prod_{\theta_i}^{\vec{\theta}} \frac{e^{-\frac{1}{2}\theta_i^2}}{\sqrt{2\pi}}. && (8.24) \end{aligned}$$

The fitted background b_i is a function of the nuisance parameters of the background functional form. The signal is scaled by an overall signal strength μ. Then, the B and S+B likelihood functions are

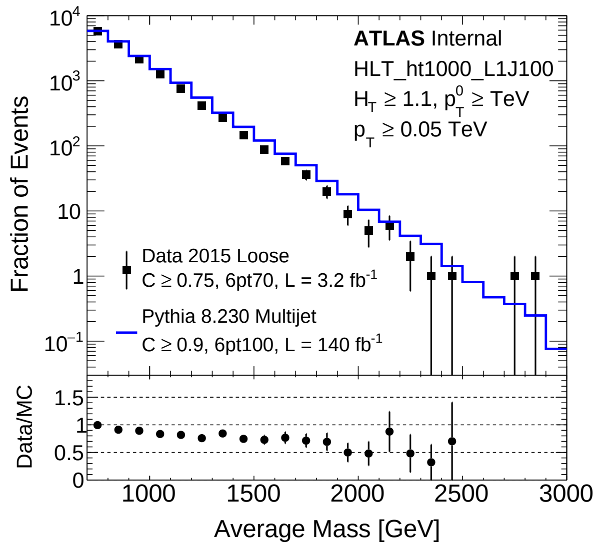

Figure 8.14: Comparison between the predicted average mass spectrum for Data 2015 Loose (black) and a Pythia 8.230 Multijet sample normalized to 140fb^{-1} (blue).

$$L_B = L\left(\lambda = b_i(\vec{p}, \vec{\theta})\right), \tag{8.25}$$

$$L_{S+B} = L\left(\lambda = s_i\mu + b_i(\vec{p}, \vec{\theta})\right). \tag{8.26}$$

The test minimizes the difference log likelihood (DLL) to obtain the optimal μ and θ_i values

$$\text{DLL} = \log L_{S+B} - \log L_B = \log \frac{L_{S+B}}{L_B} \tag{8.27}$$

$$\hat{\mu}, \hat{\vec{\theta}}, \hat{\vec{p}} = \arg\min_{\mu, \vec{p}, \vec{\theta}} \text{DLL}, \tag{8.28}$$

where μ is constrained to be non-negative and $\vec{p}$ is initialized using background only fits.

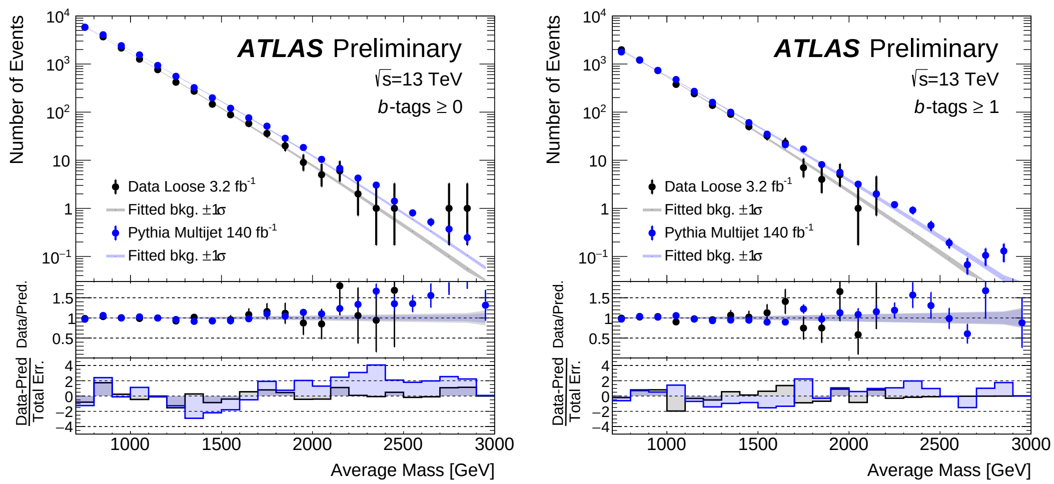

Figure 8.15: Observed data and fitted background model in the nominal (left) and ⍰-tagged (right) regions using a loose selection and 3.2 fb−1 of data which matches roughly the number of events expected in the full selection and full dataset. The grey and blue bands present the combined statistical and systematic uncertainty on the background estimate for the data and MC fit functions respectively.

The procedure is validated with MC simulation as well as a small 3.2 fb^{-1} sample of data from 2015 with a loose selection of $C \geq 0.7$ and 6 jets above 70 GeV such that the number of events is similar to that of the full dataset with nominal selections. A comparison of the distributions is shown in Figure 8.14, showing the overall shape and scale are comparable.

First, background only fits are checked for good closure. The spurious signal systematic is disabled, essentially repeating Figure 8.12 using only the nominal function. Then, S+B fits are done on the background only data to verify that the extracted signal strength is 0, the background prediction closure, impact of uncertainties, and the exclusion sensitivity. All signal systematics and spurious signal systematics are included as NPs. The final fitted signal strength is consistent with 0 up until the stats limitation around 2 TeV.

The 95% confidence limits are produced in the same manor as described in Section 7.4 and shown

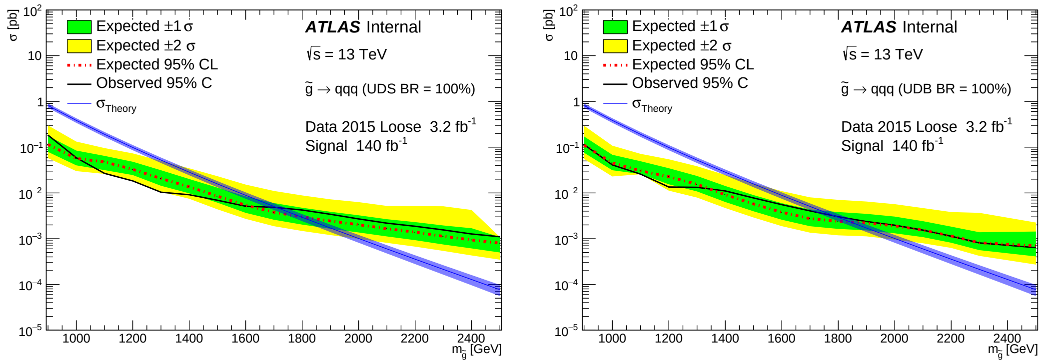

Figure 8.16: Expected exclusion contours for the gluino direct decay model with (left) UDS and (right) UDB decays, as obtained by mass resonance analysis. The yellow and green contours of the band around the expected limit are the $\pm1\sigma$ and $\pm2\sigma$ variations including both systematic and statistical uncertainties, respectively. The theoretical prediction is also shown, with the uncertainties in the prediction shown as a coloured band.

in Figure 8.16. The UDB model requires at least 1 b-tag. The exclusion is slightly worse without the b-tagging selection as compared with the UDS model because of the lower b-jet resolution and shift towards lower p_T from semileptonic decays. The relative systematic rankings are shown in Figures 8.17 and 8.18, showing the sensitivity is statistically limited at high masses.

In addition to the selections previously defined, which are used for the model-dependent interpretation, a set of model-independent SRs are defined using single bins, in the invariant mass distribution with a width of 300 GeV, and assume no signal contribution outside of the SR. When considering the model-independent SRs the background is estimated through a fit to the reconstructed average mass distribution excluding the signal region bin. This is contrary to the model-dependent fits which are performed using the full average-mass distribution with 100 GeV bins. Validation of the model-independent fits are given in Table 8.3, showing the 95% CL on the cross section times acceptance, number of events, and corresponding significance.

Signal channel	$\langle\epsilon\sigma\rangle_{\rm obs}^{95}$[fb]	$S_{\rm obs}^{95}$	$S_{\rm exp}^{95}$	CL_B	$p(s=0)\,(Z)$
700 - 1000 GeV	1.54	215.1	$172.4^{+76.1}_{-25.3}$	0.67	0.33 (0.44)
800 - 1100 GeV	0.93	129.6	$125.7^{+50.7}_{-23.5}$	0.59	0.41 (0.23)
900 - 1200 GeV	0.56	77.8	$88.2^{+36.0}_{-21.9}$	0.32	0.50 (0.00)
1000 - 1300 GeV	0.29	41.1	$66.6^{+26.6}_{-18.1}$	0.06	0.50 (0.00)
1100 - 1400 GeV	0.42	58.5	$61.4^{+12.1}_{-21.3}$	0.41	0.50 (0.00)
1200 - 1500 GeV	0.33	46.4	$46.5^{+18.6}_{-12.0}$	0.50	0.50 (0.00)
1300 - 1600 GeV	0.29	40.6	$30.5^{+13.6}_{-4.7}$	0.74	0.25 (0.67)
1400 - 1700 GeV	0.24	33.7	$23.8^{+10.5}_{-3.9}$	0.82	0.16 (0.98)
1500 - 1800 GeV	0.18	24.8	$17.7^{+8.0}_{-2.7}$	0.80	0.17 (0.97)
1600 - 1900 GeV	0.11	16.1	$14.3^{+5.5}_{-3.7}$	0.65	0.31 (0.49)
1700 - 2000 GeV	0.06	9.0	$10.7^{+4.4}_{-2.5}$	0.32	0.50 (0.00)
1800 - 2100 GeV	0.06	7.8	$8.2^{+3.6}_{-2.4}$	0.46	0.50 (0.00)
1900 - 2200 GeV	0.06	8.7	$6.6^{+3.2}_{-1.5}$	0.75	0.20 (0.83)
2000 - 2300 GeV	0.04	5.1	$5.1^{+4.1}_{-0.2}$	0.44	0.50 (0.00)
2100 - 2400 GeV	0.03	4.4	$4.1^{+2.5}_{-1.4}$	0.53	0.46 (0.11)
2200 - 2500 GeV	0.02	2.4	$3.5^{+2.2}_{-1.3}$	0.21	0.50 (0.00)
2300 - 2600 GeV	0.02	2.3	$3.0^{+2.1}_{-1.1}$	0.29	0.49 (0.01)
2400 - 2700 GeV	0.02	2.2	$2.6^{+2.0}_{-1.1}$	0.35	0.49 (0.03)
2500 - 2800 GeV	0.01	2.1	$2.4^{+1.9}_{-1.0}$	0.40	0.49 (0.02)
2600 - 2900 GeV	0.01	2.0	$2.3^{+1.8}_{-0.9}$	0.44	0.49 (0.03)
2700 - 3000 GeV	0.01	2.0	$2.1^{+1.9}_{-0.9}$	0.46	0.49 (0.04)

Table 8.3: Left to right: 95% CL upper limits on the visible cross section ($\langle\epsilon\sigma\rangle_{\rm obs}^{95}$) and on the number of signal events ($S_{\rm obs}^{95}$). The third column ($S_{\rm exp}^{95}$) shows the 95% CL upper limit on the number of signal events, given the expected number (and $\pm1\sigma$ excursions on the expectation) of background events. The last two columns indicate the CL_B value, i.e. the confidence level observed for the background-only hypothesis, and the discovery p-value ($p(s=0)$).

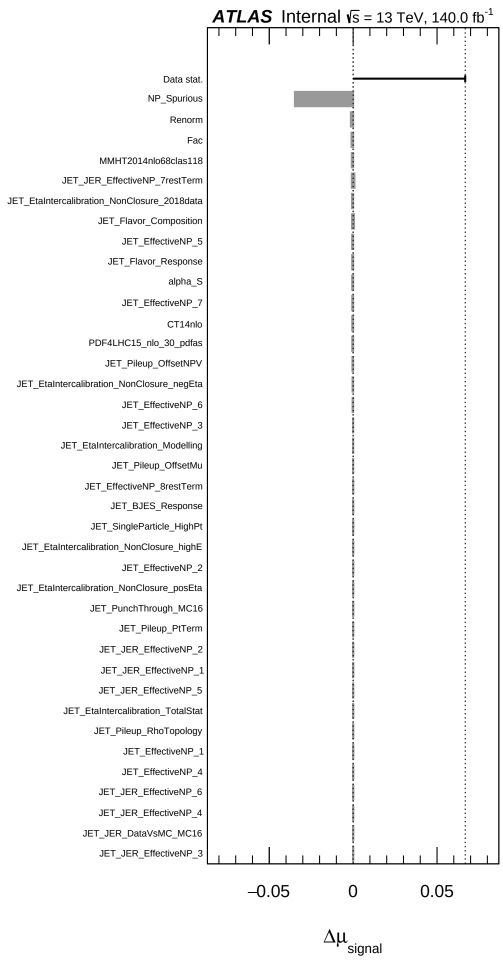

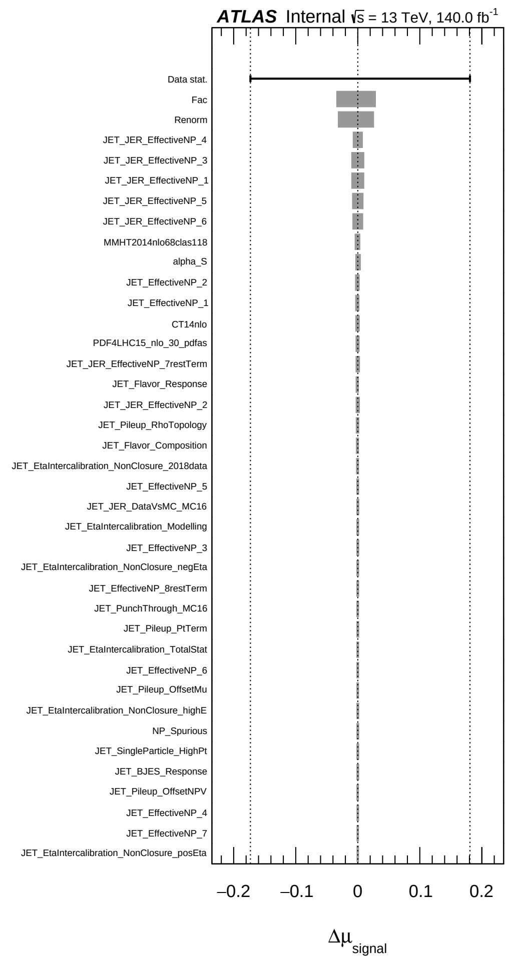

Figure 8.17: Pre-unblinding ranking of contributions to the pull of μ_{signal} by the various systematics for UDB 900 GeV (left) and 1500 GeV (right). At lower masses the systematics contribute but at higher masses where the signal yield is lower the statistical uncertainty dominates.

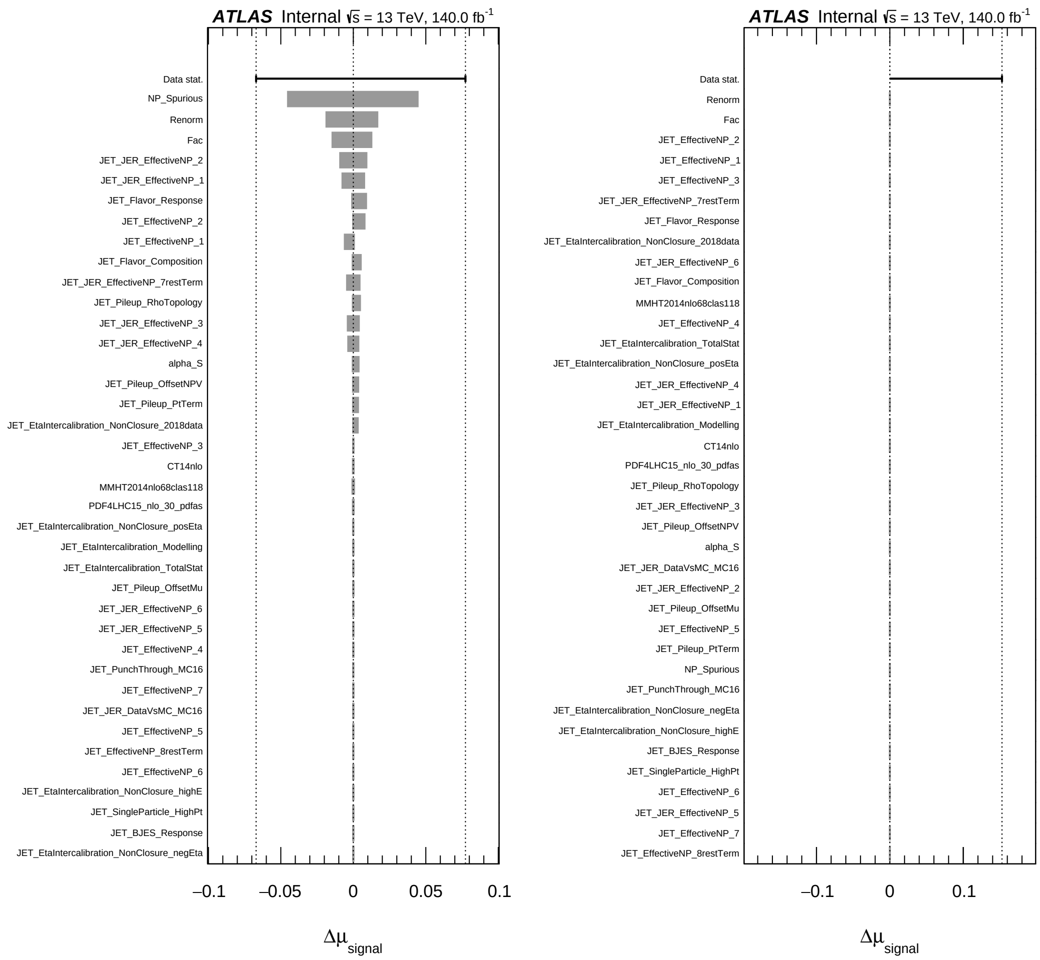

Figure 8.18: Ranking of contributions to the pull of μ_{signal} by the various systematics for UDS 900 GeV (left) and 1500 GeV (right). At lower masses the systematics contribute but at higher masses where the signal yield is lower the statistical uncertainty dominates.

8.6 Results

The observed data event yields and the corresponding estimates for the backgrounds in the SRs are shown in Figure 7 for the mass resonance method. No significant excess of data over the expected event yields is observed in any of the SRs. However, there are fluctuations in data around 1500 GeV that results in slight mismodeling of the background expectation and slight swings in the exclusion contours.

The profile likelihood-ratio test [196] is used to establish 95% confidence intervals using the CL_s prescription [197]. The asymptotic approximation of the CL_s is used for all statistical tests except for the high mass model independent bins of the mass resonance method where the number of events is small and toys are generated. The approximation is validated for other regions with moderately small yields for both methods using toys. The uncertainties introduced in the previous section are included as nuisance parameters described by a Gaussian distribution. Upper limits on the product of cross-section, acceptance, and efficiency are shown in Tables 8.4 and 8.5. The upper limits range from 7.9 to 0.03 fb, depending on the signal region considered.

Exclusion limits as a function of the masses of the SUSY particles are shown in Figure 8.20 for the direct gluino decay model. Gluinos with masses up to 1730 and 1800 GeVare excluded in the models where the gluino decay with 100% branching ratio into qqq and qqb, respectively.

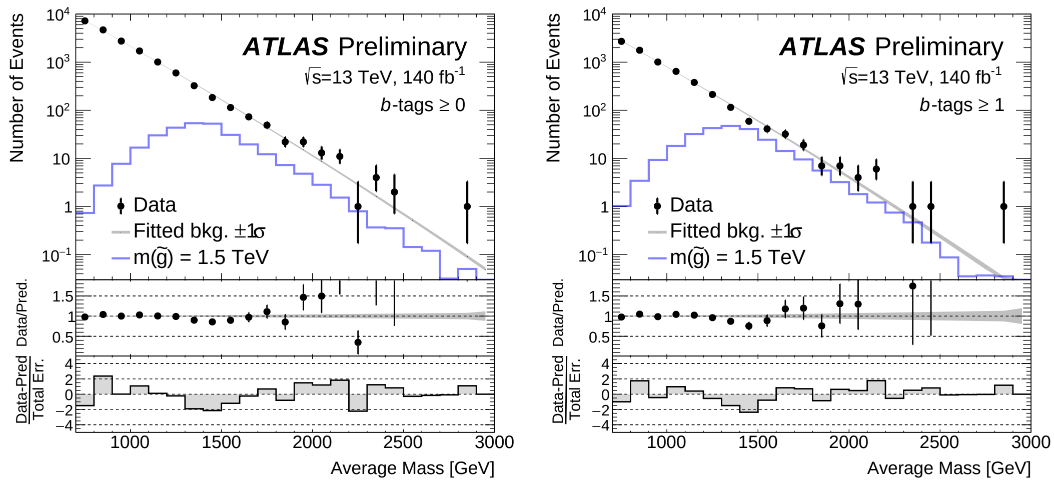

Figure 8.19: Background only fits to the reconstructed average mass spectrum of the candidate gluinos (left) ≥ 0 and (right) $\geq 1\,b$-tagged of the mass resonance method. The grey bands include both statistical and systematic uncertainties.

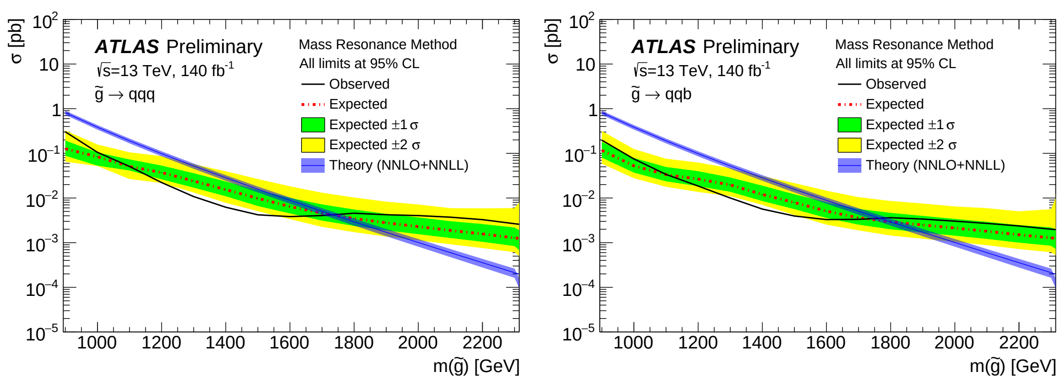

Figure 8.20: Observed and expected exclusion contours for the gluino direct decay model with (left) UDS and (right) UDB decays, as obtained by the mass resonance analysis. The yellow and green contours of the band around the expected limit are the $\pm 1\sigma$ and $\pm 2\sigma$ variations including both systematic and statistical uncertainties, respectively. The theoretical prediction is also shown, with the uncertainties in the prediction shown as a coloured band.

$\mathrm{m_{avg}}$ range [GeV]	$\langle\epsilon\sigma\rangle^{95}_{obs}$[fb]	S^{95}_{obs}	S^{95}_{exp}	CL_B	$p(s=0)\,(Z)$
700 - 1000	7.3	1000	1300^{+460}_{-300}	0.22	0.50 (0.00)
800 - 1100	5.7	800	360^{+150}_{-49}	0.99	0.01 (2.5)
900 - 1200	2.1	290	210^{+88}_{-25}	0.81	0.18 (0.91)
1000 - 1300	1.5	210	160^{+50}_{-34}	0.80	0.18 (0.90)
1100 - 1400	0.54	76	120^{+45}_{-30}	0.09	0.50 (0.00)
1200 - 1500	0.27	37	85^{+33}_{-24}	0.00	0.50 (0.00)
1300 - 1600	0.16	23	63^{+37}_{-18}	0.00	0.50 (0.00)
1400 - 1700	0.16	22	47^{+19}_{-13}	0.00	0.50 (0.00)
1500 - 1800	0.24	33	$38.8^{+16}_{-9.9}$	0.25	0.50 (0.00)
1600 - 1900	0.26	37	$37.9^{+15}_{-9.7}$	0.47	0.50 (0.00)
1700 - 2000	0.30	42	$34.1^{+12}_{-6.8}$	0.71	0.29 (0.55)
1800 - 2100	0.25	35	$28.2^{+12}_{-7.6}$	0.72	0.28 (0.57)
1900 - 2200	0.29	41	$24.5^{+11}_{-3.8}$	0.93	0.06 (1.5)
2000 - 2300	0.19	27	$21.5^{+7.6}_{-4.4}$	0.78	0.19 (0.89)
2100 - 2400	0.15	21	$15.5^{+6.2}_{-2.3}$	0.74	0.20 (0.84)
2200 - 2500	0.08	11	$10.5^{+3.2}_{-1.9}$	0.57	0.40 (0.26)
2300 - 2600	0.08	11	$9.2^{+3.9}_{-1.2}$	0.66	0.27 (0.61)
2400 - 2700	0.05	6.9	$6.8^{+2.1}_{-1.4}$	0.51	0.48 (0.05)
2500 - 2800	0.02	2.3	$3.1^{+2.1}_{-1.2}$	0.26	0.50 (0.01)
2600 - 2900	0.04	5.3	$5.2^{+2.2}_{-1.3}$	0.52	0.46 (0.10)
2700 - 3000	0.06	8.3	$8.2^{+0.4}_{-0.7}$	0.53	0.44 (0.16)

Table 8.4: The upper limit table for the $\geq 0\ b$-tagged jets region. Left to right: 95% CL upper limits on the visible cross section ($\langle\epsilon\sigma\rangle^{95}_{obs}$) and on the number of signal events (S^{95}_{obs}). The third column (S^{95}_{exp}) shows the 95% CL upper limit on the number of signal events, given the expected number (and $\pm 1\sigma$ excursions on the expectation) of background events. The last two columns indicate the CL_B value, i.e. the confidence level observed for the background-only hypothesis, and the discovery p-value ($p(s=0)$).

m_{avg} range [GeV]	$\langle\epsilon\sigma\rangle^{95}_{obs}$[fb]	S^{95}_{obs}	S^{95}_{exp}	CL_B	$p(s=0)\,(Z)$
700 - 1000	5.7	800	960^{+330}_{-240}	0.31	0.50 (0.00)
800 - 1100	3.3	460	320^{+100}_{-65}	0.89	0.11 (1.2)
900 - 1200	1.1	150	130^{+38}_{-31}	0.74	0.24 (0.71)
1000 - 1300	0.92	130	92^{+40}_{-13}	0.81	0.18 (0.91)
1100 - 1400	0.36	51	70^{+27}_{-20}	0.17	0.50 (0.00)
1200 - 1500	0.16	23	52^{+21}_{-15}	0.00	0.50 (0.00)
1300 - 1600	0.11	16	39^{+15}_{-11}	0.00	0.50 (0.00)
1400 - 1700	0.12	17	$28.9^{+12}_{-8.1}$	0.04	0.50 (0.00)
1500 - 1800	0.20	27	$24.9^{+25}_{-7.1}$	0.61	0.38 (0.29)
1600 - 1900	0.25	35	$30.0^{+10}_{-7.1}$	0.68	0.45 (0.13)
1700 - 2000	0.21	30	$27.7^{+10}_{-7.7}$	0.58	0.42 (0.20)
1800 - 2100	0.17	24	$24.0^{+5.9}_{-6.2}$	0.51	0.49 (0.03)
1900 - 2200	0.18	25	$21.6^{+5.9}_{-5.8}$	0.71	0.26 (0.65)
2000 - 2300	0.13	18	$17.1^{+5.3}_{-2.1}$	0.63	0.32 (0.47)
2100 - 2400	0.10	13	$12.4^{+3.3}_{-2.6}$	0.63	0.30 (0.51)
2200 - 2500	0.05	6.4	$6.4^{+2.5}_{-1.5}$	0.50	0.50 (0.00)
2300 - 2600	0.05	6.8	$6.7^{+2.6}_{-0.8}$	0.54	0.42 (0.20)
2400 - 2700	0.03	4.0	$3.9^{+2.2}_{-1.2}$	0.52	0.45 (0.14)
2500 - 2800	0.01	2.0	$2.1^{+1.8}_{-0.9}$	0.47	0.49 (0.02)
2600 - 2900	0.04	5.4	$5.3^{+2.2}_{-1.3}$	0.53	0.43 (0.19)
2700 - 3000	0.04	6.1	$6.0^{+2.3}_{-0.6}$	0.53	0.42 (0.20)

Table 8.5: The upper limit table for the ≥ 1 b-tagged jets region. Left to right: 95% CL upper limits on the visible cross section ($\langle\epsilon\sigma\rangle^{95}_{obs}$) and on the number of signal events (S^{95}_{obs}). The third column (S^{95}_{exp}) shows the 95% CL upper limit on the number of signal events, given the expected number (and $\pm 1\sigma$ excursions on the expectation) of background events. The last two columns indicate the CL_B value, i.e. the confidence level observed for the background-only hypothesis, and the discovery p-value ($p(s = 0)$).

9

Conclusion

A search for RPV SUSY signals in events with multiple jets is performed with $140\ \mathrm{fb}^{-1}$ of proton–proton collision data at $\sqrt{s} = 13$ TeVcollected by the ATLAS detector at the LHC. Two methods are utilised, a jet counting method searching for excess events in single-bin signal regions defined at high jet multiplicity and high C, and a mass resonance approach, which searches for a localized excess in the reconstructed gluino mass spectrum. A novel machine-learning approach is employed to address the combinatorial assignment problem and successfully reconstruct the gluino mass. No significant excess is seen in any signal region. Limits are set on the production of gluinos in the direct and cascade decay models in $U\bar{D}\bar{D}$ scenarios of RPV SUSY. In the direct decay model, gluinos with masses up to 1800 GeV are excluded at 95% CL. In the cascade decay model, gluinos with masses as high as 2340 GeV are excluded for a neutralino with 1250 GeV mass. Model-independent limits are also set on the signal production cross section times branching ratio in five overlapping signal regions. This search significantly extends the limits from previous results beyond the expected improvement due to the larger dataset. These results improve upon the previously existing LHC limits owing to the larger luminosity, the introduction of event shape variables to suppress background, and the development of machine-learning techniques to assign jets to gluinos and reconstruct their mass. Looking forward, the techniques developed here will become a backbone for searches and measurements at colliders as well as other experiments.

References

[1] Ux standard model of physics. https://texample.net/tikz/examples/model-physics/.

[2] Particle Data Group. Review of Particle Physics. *Progress of Theoretical and Experimental Physics*, 2020(8), 08 2020. ISSN 2050-3911. doi: 10.1093/ptep/ptaa104. URL https://doi.org/10.1093/ptep/ptaa104. 083C01.

[3] E. Noether. Invariante variationsprobleme. *Nachrichten von der Gesellschaft der Wissenschaften zu Göttingen, Mathematisch-Physikalische Klasse*, 1918:235–257, 1918. URL http://eudml.org/doc/59024.

[4] Bloom et al. High-energy inelastic $e - p$ scattering at 6° and 10°. *Phys. Rev. Lett.*, 23:930–934, Oct 1969. doi: 10.1103/PhysRevLett.23.930. URL https://link.aps.org/doi/10.1103/PhysRevLett.23.930.

[5] M. Breidenbach, J. I. Friedman, H. W. Kendall, E. D. Bloom, D. H. Coward, H. DeStaebler, J. Drees, L. W. Mo, and R. E. Taylor. Observed behavior of highly inelastic electron-proton scattering. *Phys. Rev. Lett.*, 23:935–939, Oct 1969. doi: 10.1103/PhysRevLett.23.935. URL https://link.aps.org/doi/10.1103/PhysRevLett.23.935.

[6] B.J. Bjørken and S.L. Glashow. Elementary particles and su(4). *Physics Letters*, 11(3):255–257, 1964. ISSN 0031-9163. doi: https://doi.org/10.1016/0031-9163(64)90433-0. URL https://www.sciencedirect.com/science/article/pii/0031916364904330.

[7] Aubert et al. Experimental observation of a heavy particle j. *Phys. Rev. Lett.*, 33:1404–1406, Dec 1974. doi: 10.1103/PhysRevLett.33.1404. URL https://link.aps.org/doi/10.1103/PhysRevLett.33.1404.

[8] Augustin et al. Discovery of a narrow resonance in e^+e^- annihilation. *Phys. Rev. Lett.*, 33:1406–1408, Dec 1974. doi: 10.1103/PhysRevLett.33.1406. URL https://link.aps.org/doi/10.1103/PhysRevLett.33.1406.

[9] Abe et al. Observation of top quark production in $\overline{p}p$ collisions with the collider detector at fermilab. *Phys. Rev. Lett.*, 74:2626–2631, Apr 1995. doi: 10.1103/PhysRevLett.74.2626. URL https://link.aps.org/doi/10.1103/PhysRevLett.74.2626.

[10] Abachi et al. Observation of the top quark. *Phys. Rev. Lett.*, 74:2632–2637, Apr 1995. doi: 10.1103/PhysRevLett.74.2632. URL https://link.aps.org/doi/10.1103/PhysRevLett.74.2632.

[11] S. W. Herb, D. C. Hom, L. M. Lederman, J. C. Sens, H. D. Snyder, J. K. Yoh, J. A. Appel, B. C. Brown, C. N. Brown, W. R. Innes, K. Ueno, T. Yamanouchi, A. S. Ito, H. Jöstlein, D. M. Kaplan, and R. D. Kephart. Observation of a dimuon resonance at 9.5 gev in 400-gev proton-nucleus collisions. *Phys. Rev. Lett.*, 39:252–255, Aug 1977. doi: 10.1103/PhysRevLett.39.252. URL https://link.aps.org/doi/10.1103/PhysRevLett.39.252.

[12] J. J. Thomson M.A. F.R.S. Xl. cathode rays. *The London, Edinburgh, and Dublin Philosophical Magazine and Journal of Science*, 44(269):293–316, 1897. doi: 10.1080/14786449708621070. URL https://doi.org/10.1080/14786449708621070.

[13] Carl D. Anderson. The apparent existence of easily deflectable positives. *Science*, 76(1967): 238–239, 1932. doi: 10.1126/science.76.1967.238. URL https://www.science.org/doi/abs/10.1126/science.76.1967.238.

[14] Seth H. Neddermeyer and Carl D. Anderson. Note on the nature of cosmic-ray particles. *Phys. Rev.*, 51:884–886, May 1937. doi: 10.1103/PhysRev.51.884. URL https://link.aps.org/doi/10.1103/PhysRev.51.884.

[15] Perl et al. Evidence for anomalous lepton production in $e^+ - e^-$ annihilation. *Phys. Rev. Lett.*, 35:1489–1492, Dec 1975. doi: 10.1103/PhysRevLett.35.1489. URL https://link.aps.org/doi/10.1103/PhysRevLett.35.1489.

[16] FREDERICK REINES and CLYDE L. COWANjun. The neutrino. *Nature*, 178(4531):446–449, 1956.

[17] G. Danby, J-M. Gaillard, K. Goulianos, L. M. Lederman, N. Mistry, M. Schwartz, and J. Steinberger. Observation of high-energy neutrino reactions and the existence of two kinds of neutrinos. *Phys. Rev. Lett.*, 9:36–44, Jul 1962. doi: 10.1103/PhysRevLett.9.36. URL https://link.aps.org/doi/10.1103/PhysRevLett.9.36.

[18] K. Kodama et al. Observation of tau neutrino interactions. *Physics Letters B*, 504(3):218–224, 2001. ISSN 0370-2693. doi: https://doi.org/10.1016/S0370-2693(01)00307-0. URL https://www.sciencedirect.com/science/article/pii/S0370269301003070.

[19] Jeffrey Goldstone, Abdus Salam, and Steven Weinberg. Broken symmetries. *Phys. Rev.*, 127:965–970, Aug 1962. doi: 10.1103/PhysRev.127.965. URL https://link.aps.org/doi/10.1103/PhysRev.127.965.

[20] Y. Nambu and G. Jona-Lasinio. Dynamical model of elementary particles based on an analogy with superconductivity. i. *Phys. Rev.*, 122:345–358, Apr 1961. doi: 10.1103/PhysRev.122.345. URL https://link.aps.org/doi/10.1103/PhysRev.122.345.

[21] J. Goldstone. Field theories with superconductor solutions. *Il Nuovo Cimento (1955-1965)*, 19(1):154–164, 1961. doi: 10.1007/BF02812722. URL https://doi.org/10.1007/BF02812722.

[22] Barber et al. Discovery of three-jet events and a test of quantum chromodynamics at petra. *Phys. Rev. Lett.*, 43:830–833, Sep 1979. doi: 10.1103/PhysRevLett.43.830. URL https://link.aps.org/doi/10.1103/PhysRevLett.43.830.

[23] G. Arnison et al. Experimental observation of isolated large transverse energy electrons with associated missing energy at s=540 gev. *Physics Letters B*, 122(1):103–116, 1983. ISSN 0370-2693. doi: https://doi.org/10.1016/0370-2693(83)91177-2. URL https://www.sciencedirect.com/science/article/pii/0370269383911772.

[24] M. Banner et al. Observation of single isolated electrons of high transverse momentum in events with missing transverse energy at the cern pp collider. *Physics Letters B*, 122(5):476–485, 1983. ISSN 0370-2693. doi: https://doi.org/10.1016/0370-2693(83)91605-2. URL https://www.sciencedirect.com/science/article/pii/0370269383916052.

[25] P. Bagnaia et al. Evidence for zo→e+e− at the cern pp collider. *Physics Letters B*, 129(1):130–140, 1983. ISSN 0370-2693. doi: https://doi.org/10.1016/0370-2693(83)90744-X. URL https://www.sciencedirect.com/science/article/pii/037026938390744X.

[26] G. Arnison et al. Experimental observation of lepton pairs of invariant mass around 95 gev/c2 at the cern sps collider. *Physics Letters B*, 126(5):398–410, 1983. ISSN 0370-2693. doi: https://doi.org/10.1016/0370-2693(83)90188-0. URL https://www.sciencedirect.com/science/article/pii/0370269383901880.

[27] CMS Collaboration. Observation of a new boson at a mass of 125 GeV with the CMS experiment at the LHC. *Physics Letters B*, 716(1):30–61, sep 2012. doi: 10.1016/j.physletb.2012.08.021. URL https://doi.org/10.1016%2Fj.physletb.2012.08.021.

[28] ATLAS Collaboration. Observation of a new particle in the search for the Standard Model Higgs boson with the ATLAS detector at the LHC. *Phys. Lett. B*, 716:1, 2012. doi: 10.1016/j.physletb.2012.08.020.

[29] Peter W. Higgs. Broken symmetries and the masses of gauge bosons. *Phys. Rev. Lett.*, 13:508–509, Oct 1964. doi: 10.1103/PhysRevLett.13.508. URL https://link.aps.org/doi/10.1103/PhysRevLett.13.508.

[30] F. Englert and R. Brout. Broken symmetry and the mass of gauge vector mesons. *Phys. Rev. Lett.*, 13:321–323, Aug 1964. doi: 10.1103/PhysRevLett.13.321. URL https://link.aps.org/doi/10.1103/PhysRevLett.13.321.

[31] G. S. Guralnik, C. R. Hagen, and T. W. B. Kibble. Global conservation laws and massless particles. *Phys. Rev. Lett.*, 13:585–587, Nov 1964. doi: 10.1103/PhysRevLett.13.585. URL https://link.aps.org/doi/10.1103/PhysRevLett.13.585.

[32] C. N. Yang and R. L. Mills. Conservation of isotopic spin and isotopic gauge invariance. *Phys. Rev.*, 96:191–195, Oct 1954. doi: 10.1103/PhysRev.96.191. URL https://link.aps.org/doi/10.1103/PhysRev.96.191.

[33] Jeff Greensite. *An introduction to the confinement problem*, volume 821. 2011. doi: 10.1007/978-3-642-14382-3.

[34] David J. Gross and Frank Wilczek. Ultraviolet behavior of non-abelian gauge theories. *Phys. Rev. Lett.*, 30:1343–1346, Jun 1973. doi: 10.1103/PhysRevLett.30.1343. URL https://link.aps.org/doi/10.1103/PhysRevLett.30.1343.

[35] H. David Politzer. Reliable perturbative results for strong interactions? *Phys. Rev. Lett.*, 30:1346–1349, Jun 1973. doi: 10.1103/PhysRevLett.30.1346. URL https://link.aps.org/doi/10.1103/PhysRevLett.30.1346.

[36] Sheldon L. Glashow. Partial-symmetries of weak interactions. *Nuclear Physics*, 22(4):579–588, 1961. ISSN 0029-5582. doi: https://doi.org/10.1016/0029-5582(61)90469-2. URL https://www.sciencedirect.com/science/article/pii/0029558261904692.

[37] A. Salam and J.C. Ward. Electromagnetic and weak interactions. *Physics Letters*, 13(2):168–171, 1964. ISSN 0031-9163. doi: https://doi.org/10.1016/0031-9163(64)90711-5. URL https://www.sciencedirect.com/science/article/pii/0031916364907115.

[38] Steven Weinberg. A model of leptons. *Phys. Rev. Lett.*, 19:1264–1266, Nov 1967. doi: 10.1103/PhysRevLett.19.1264. URL https://link.aps.org/doi/10.1103/PhysRevLett.19.1264.

[39] T. D. Lee and C. N. Yang. Question of parity conservation in weak interactions. *Phys. Rev.*, 104:254–258, Oct 1956. doi: 10.1103/PhysRev.104.254. URL https://link.aps.org/doi/10.1103/PhysRev.104.254.

[40] C. S. Wu, E. Ambler, R. W. Hayward, D. D. Hoppes, and R. P. Hudson. Experimental test of parity conservation in beta decay. *Phys. Rev.*, 105:1413–1415, Feb 1957. doi: 10.1103/PhysRev.105.1413. URL https://link.aps.org/doi/10.1103/PhysRev.105.1413.

[41] Richard L. Garwin, Leon M. Lederman, and Marcel Weinrich. Observations of the failure of conservation of parity and charge conjugation in meson decays: the magnetic moment of the free muon. *Phys. Rev.*, 105:1415–1417, Feb 1957. doi: 10.1103/PhysRev.105.1415. URL https://link.aps.org/doi/10.1103/PhysRev.105.1415.

[42] V. C. Rubin, Jr. Ford, W. K., and N. Thonnard. Rotational properties of 21 sc galaxies with a large range of luminosities and radii, from ngc 4605 (r=4kpc) to ugc 2885 (r=122kpc). 238:471–487, 1980. doi: 10.1086/158003.

[43] Leszek Roszkowski, Enrico Maria Sessolo, and Sebastian Trojanowski. WIMP dark matter candidates and searches—current status and future prospects. *Reports on Progress in Physics*, 81(6):066201, may 2018. doi: 10.1088/1361-6633/aab913. URL https://doi.org/10.1088%2F1361-6633%2Faab913.

[44] Plank Collaboration. Plank 2015 results. *Astronomy Astrophysics*, 594:A1, sep 2016. doi: 10.1051/0004-6361/201527101. URL https://doi.org/10.1051%2F0004-6361%2F201527101.

[45] Felix Kahlhoefer. Review of LHC dark matter searches. *International Journal of Modern Physics A*, 32(13):1730006, may 2017. doi: 10.1142/s0217751x1730006x. URL https://doi.org/10.1142%2Fs0217751x1730006x.

[46] S. Perlmutter, G. Aldering, G. Goldhaber, R. A. Knop, P. Nugent, P. G. Castro, S. Deustua, S. Fabbro, A. Goobar, D. E. Groom, I. M. Hook, A. G. Kim, M. Y. Kim, J. C. Lee, N. J. Nunes,

R. Pain, C. R. Pennypacker, R. Quimby, C. Lidman, R. S. Ellis, M. Irwin, R. G. McMahon, P. Ruiz-Lapuente, N. Walton, B. Schaefer, B. J. Boyle, A. V. Filippenko, T. Matheson, A. S. Fruchter, N. Panagia, H. J. M. Newberg, W. J. Couch, and The Supernova Cosmology Project. Measurements of ω and λ from 42 high-redshift supernovae. *The Astrophysical Journal*, 517 (2):565–586, jun 1999. doi: 10.1086/307221. URL https://doi.org/10.1086%2F307221.

[47] Adam G. Riess, Alexei V. Filippenko, Peter Challis, Alejandro Clocchiatti, Alan Diercks, Peter M. Garnavich, Ron L. Gilliland, Craig J. Hogan, Saurabh Jha, Robert P. Kirshner, B. Leibundgut, M. M. Phillips, David Reiss, Brian P. Schmidt, Robert A. Schommer, R. Chris Smith, J. Spyromilio, Christopher Stubbs, Nicholas B. Suntzeff, and John Tonry. Observational evidence from supernovae for an accelerating universe and a cosmological constant. *The Astronomical Journal*, 116(3):1009–1038, sep 1998. doi: 10.1086/300499. URL https://doi.org/10.1086%2F300499.

[48] Jerome Martin. Everything you always wanted to know about the cosmological constant problem (but were afraid to ask). *Comptes Rendus Physique*, 13(6-7):566–665, jul 2012. doi: 10.1016/j.crhy.2012.04.008. URL https://doi.org/10.1016%2Fj.crhy.2012.04.008.

[49] P. J. E. Peebles and Bharat Ratra. The cosmological constant and dark energy. *Reviews of Modern Physics*, 75(2):559–606, apr 2003. doi: 10.1103/revmodphys.75.559. URL https://doi.org/10.1103%2Frevmodphys.75.559.

[50] Anto. I. Lonappan, Sumit Kumar, Ruchika, Bikash R. Dinda, and Anjan A. Sen. Bayesian evidences for dark energy models in light of current observational data. *Physical Review D*, 97(4), feb 2018. doi: 10.1103/physrevd.97.043524. URL https://doi.org/10.1103%2Fphysrevd.97.043524.

[51] Andrei D Sakharov. Violation of cp invariance, c asymmetry, and baryon asymmetry of the universe. *Soviet Physics Uspekhi*, 34(5):392, may 1991. doi: 10.1070/PU1991v034n05ABEH002497. URL https://dx.doi.org/10.1070/PU1991v034n05ABEH002497.

[52] M. B. GAVELA, P. HERNNDEZ, J. ORLOFF, and O. PENE. STANDARD MODEL CP-VIOLATION AND BARYON ASYMMETRY. *Modern Physics Letters A*, 09(09):795–809, mar 1994. doi: 10.1142/s0217732394000629. URL https://doi.org/10.1142%2Fs0217732394000629.

[53] Bastian Bergerhoff and Christof Wetterich. Electroweak phase transition in the early universe ?, 1997.

[54] The Super-Kamiokande Collaboration. Evidence for oscillation of atmospheric neutrinos. *Physical Review Letters*, 81(8):1562–1567, aug 1998. doi: 10.1103/physrevlett.81.1562. URL https://doi.org/10.1103%2Fphysrevlett.81.1562.

[55] SNO Collaboration. Measurement of the rate of $\nu_e + d \rightarrow p + p + e^-$ interactions produced by 8b solar neutrinos at the sudbury neutrino observatory. *Physical Review Letters*, 87(7), jul 2001. doi: 10.1103/physrevlett.87.071301. URL https://doi.org/10.1103%2Fphysrevlett.87.071301.

[56] KamLand Collaboration. Precision measurement of neutrino oscillation parameters with kamland. *Phys. Rev. Lett.*, 100:221803, Jun 2008. doi: 10.1103/PhysRevLett.100.221803. URL https://link.aps.org/doi/10.1103/PhysRevLett.100.221803.

[57] Karlsruhe Tritium Neutrino Experiment. Improved upper limit on the neutrino mass from a direct kinematic method by KATRIN. *Physical Review Letters*, 123(22), nov 2019. doi: 10.1103/physrevlett.123.221802. URL https://doi.org/10.1103%2Fphysrevlett.123.221802.

[58] R. Barbieri and G.F. Giudice. Upper bounds on supersymmetric particle masses. *Nuclear Physics B*, 306(1):63–76, 1988. ISSN 0550-3213. doi: https://doi.org/10.1016/0550-3213(88)90171-X. URL https://www.sciencedirect.com/science/article/pii/055032138890171X.

[59] Nathaniel Craig. Naturalness: A snowmass white paper, 2022.

[60] Gino Isidori, G Ridolfi, and A Strumia. On the metastability of the Standard Model vacuum. *Nucl. Phys. B*, 609:387–409, 2001. doi: 10.1016/S0550-3213(01)00302-9. URL https://cds.cern.ch/record/493737.

[61] Richard P Feynman, Fernando B Morinigo, and William G Wagner. Feynman lectures on gravitation. *European Journal of Physics*, 24(3):330, may 2003. doi: 10.1088/0143-0807/24/3/702. URL https://dx.doi.org/10.1088/0143-0807/24/3/702.

[62] R. D. Peccei and Helen R. Quinn. Constraints imposed by CP conservation in the presence of pseudoparticles. *Phys. Rev. D*, 16:1791–1797, Sep 1977. doi: 10.1103/PhysRevD.16.1791. URL https://link.aps.org/doi/10.1103/PhysRevD.16.1791.

[63] Yuval Grossman. Introduction to flavor physics. pages 111–144, 2014. doi: 10.5170/CERN-2010-002.111. URL https://cds.cern.ch/record/1272886.

[64] Yu. A. Golfand and E. P. Likhtman. Extension of the Algebra of Poincare Group Generators and Violation of p Invariance. *JETP Lett.*, 13:323–326, 1971.

[65] D. V. Volkov and V. P. Akulov. Is the Neutrino a Goldstone Particle? *Phys. Lett. B*, 46:109, 1973. doi: 10.1016/0370-2693(73)90490-5.

[66] J. Wess and B. Zumino. Supergauge Transformations in Four-Dimensions. *Nucl. Phys. B*, 70: 39, 1974. doi: 10.1016/0550-3213(74)90355-1.

[67] J. Wess and B. Zumino. Supergauge Invariant Extension of Quantum Electrodynamics. *Nucl. Phys. B*, 78:1, 1974. doi: 10.1016/0550-3213(74)90112-6.

[68] S. Ferrara and B. Zumino. Supergauge Invariant Yang-Mills Theories. *Nucl. Phys. B*, 79:413, 1974. doi: 10.1016/0550-3213(74)90559-8.

[69] Abdus Salam and J. A. Strathdee. Supersymmetry and Nonabelian Gauges. *Phys. Lett. B*, 51: 353, 1974. doi: 10.1016/0370-2693(74)90226-3.

[70] Herbi K. Dreiner, Yong Sheng Koay, Dominik Köhler, Víctor Martín Lozano, Javier Montejo Berlingen, Saurabh Nangia, and Nadja Strobbe. The abc of rpv: Classification of r-parity violating signatures at the lhc for small couplings, 2023.

[71] Pierre Fayet. Supersymmetry and Weak, Electromagnetic and Strong Interactions. *Phys. Lett. B*, 64:159, 1976. doi: 10.1016/0370-2693(76)90319-1.

[72] Pierre Fayet. Spontaneously Broken Supersymmetric Theories of Weak, Electromagnetic and Strong Interactions. *Phys. Lett. B*, 69:489, 1977. doi: 10.1016/0370-2693(77)90852-8.

[73] Glennys R. Farrar and Pierre Fayet. Phenomenology of the Production, Decay, and Detection of New Hadronic States Associated with Supersymmetry. *Phys. Lett. B*, 76:575, 1978. doi: 10.1016/0370-2693(78)90858-4.

[74] Savas Dimopoulos and Howard Georgi. Softly Broken Supersymmetry and SU(5). *Nucl. Phys. B*, 193:150, 1981. doi: 10.1016/0550-3213(81)90522-8.

[75] Herbert K. Dreiner. An Introduction to explicit R-parity violation. *Adv. Ser. Direct. High Energy Phys.*, 21:565–583, 2010. doi: 10.1142/9789814307505_0017.

[76] B. C. Allanach, A. Dedes, and H. K. Dreiner. R parity violating minimal supergravity model. *Phys. Rev. D*, 69:115002, 2004. doi: 10.1103/PhysRevD.69.115002. [Erratum: Phys.Rev.D 72, 079902 (2005)].

[77] ATLAS Collaboration. Search for R-parity-violating supersymmetric particles in multi-jet final states produced in pp collisions at $\sqrt{s} = 13$ TeV using the ATLAS detector at the LHC. *Phys. Lett. B*, 785:136, 2018. doi: 10.1016/j.physletb.2018.08.021.

[78] LHC New Physics Working Group. Simplified models for LHC new physics searches. *Journal of Physics G: Nuclear and Particle Physics*, 39(10):105005, sep 2012. doi: 10.1088/0954-3899/39/10/105005. URL https://doi.org/10.1088%2F0954-3899%2F39%2F10%2F105005.

[79] H Georgi. Effective field theory. *Annual Review of Nuclear and Particle Science*, 43(1):209–252, 1993. doi: 10.1146/annurev.ns.43.120193.001233. URL https://doi.org/10.1146/annurev.ns.43.120193.001233.

[80] Ilaria Brivio and Michael Trott. The standard model as an effective field theory. *Physics Reports*, 793:1–98, feb 2019. doi: 10.1016/j.physrep.2018.11.002. URL https://doi.org/10.1016%2Fj.physrep.2018.11.002.

[81] Celine Degrande, Nicolas Greiner, Wolfgang Kilian, Olivier Mattelaer, Harrison Mebane, Tim Stelzer, Scott Willenbrock, and Cen Zhang. Effective field theory: A modern approach to anomalous couplings. *Annals of Physics*, 335:21–32, aug 2013. doi: 10.1016/j.aop.2013.04.016. URL https://doi.org/10.1016%2Fj.aop.2013.04.016.

[82] John C. Collins, Davison E. Soper, and George Sterman. Factorization of hard processes in qcd, 2004.

[83] Richard D. Ball, Valerio Bertone, Stefano Carrazza, Luigi Del Debbio, Stefano Forte, Patrick Groth-Merrild, Alberto Guffanti, Nathan P. Hartland, Zahari Kassabov, José I. Latorre, Emanuele R. Nocera, Juan Rojo, Luca Rottoli, Emma Slade, and Maria Ubiali. Parton distributions from high-precision collider data. Parton distributions from high-precision collider data. *Eur. Phys. J. C*, 77(10):663, 2017. doi: 10.1140/epjc/s10052-017-5199-5. URL https://cds.cern.ch/record/2267455.

[84] Anwar A. Bhatti and Don Lincoln. Jet physics at the tevatron. *Annual Review of Nuclear and Particle Science*, 60(1):267–297, nov 2010. doi: 10.1146/annurev.nucl.012809.104430. URL https://doi.org/10.1146%2Fannurev.nucl.012809.104430.

[85] A. Metz and A. Vossen. Parton fragmentation functions. *Progress in Particle and Nuclear Physics*, 91:136–202, nov 2016. doi: 10.1016/j.ppnp.2016.08.003. URL https://doi.org/10.1016%2Fj.ppnp.2016.08.003.

[86] ATLAS Collaboration. Public atlas luminosity results for run-2 of the lhc. 2019. URL https://twiki.cern.ch/twiki/bin/view/AtlasPublic/LuminosityPublicResultsRun2.

[87] LHC Guide. 2017. URL https://cds.cern.ch/record/2255762.

[88] Maximilien Brice. Cross section of an LHC dipole in the tunnel. 2011. URL https://cds.cern.ch/record/1365795.

[89] Oliver Sim Bruning, Paul Collier, P Lebrun, Stephen Myers, Ranko Ostojic, John Poole, and Paul Proudlock. *LHC Design Report*. CERN Yellow Reports: Monographs. CERN, Geneva, 2004. doi: 10.5170/CERN-2004-003-V-1. URL https://cds.cern.ch/record/782076.

[90] Belen Salvachua. Overview of proton runs during run 2. 2019. URL https://indico.cern.ch/event/751857/contributions/3259373/attachments/1783143/2910577/belen-Evian2019.pdf.

[91] Luminosity determination in pp collisions at $\sqrt{s} = 13$ TeV using the ATLAS detector at the LHC. Technical report, CERN, Geneva, 2019. URL https://cds.cern.ch/record/2677054. All figures including auxiliary figures are available at https://atlas.web.cern.ch/Atlas/GROUPS/PHYSICS/CONFNOTES/ATLAS-CONF-2019-021.

[92] Joao Pequenao. Computer generated image of the whole ATLAS detector. 2008. URL https://cds.cern.ch/record/1095924.

[93] The ATLAS Collaboration. The atlas experiment at the cern large hadron collider. *Journal of Instrumentation*, 3(08):S08003, aug 2008. doi: 10.1088/1748-0221/3/08/S08003. URL https://dx.doi.org/10.1088/1748-0221/3/08/S08003.

[94] Izaak Neutelings. Cms coordinate system. 2021. URL https://tikz.net/axis3d_cms/.

[95] Joao Pequenao. Computer generated image of the ATLAS inner detector. 2008. URL https://cds.cern.ch/record/1095926.

[96] ATLAS Collaboration. Study of the material of the ATLAS inner detector for Run 2 of the LHC. Study of the material of the ATLAS inner detector for Run 2 of the LHC. *JINST*, 12:P12009, 2017. doi: 10.1088/1748-0221/12/12/P12009. URL https://cds.cern.ch/record/2273894. 60 pages in total, author list starting page 44, 21 figures, 7 tables, submitted to JINST, All figures including auxiliary figures are available at https://atlas.web.cern.ch/Atlas/GROUPS/PHYSICS/PAPERS/PERF-2015-07/.

[97] ATLAS Collaboration. ATLAS pixel detector electronics and sensors. *JINST*, 3:P07007, 2008. doi: 10.1088/1748-0221/3/07/P07007. URL https://cds.cern.ch/record/1119279.

[98] M. Backhaus. The upgraded pixel detector of the atlas experiment for run 2 at the large hadron collider. *Nuclear Instruments and Methods in Physics Research Section A: Accelerators, Spectrometers, Detectors and Associated Equipment*, 831:65–70, 2016. ISSN 0168-9002. doi: https://doi.org/10.1016/j.nima.2016.05.018. URL https://www.sciencedirect.com/science/article/pii/S0168900216303837. Proceedings of the 10th International "Hiroshima" Symposium on the Development and Application of Semiconductor Tracking Detectors.

[99] Alessandro La Rosa. ATLAS Pixel Detector: Operational Experience and Run-1 to Run-2 Transition. Technical report, CERN, Geneva, 2015. URL https://cds.cern.ch/record/1956433. presented at VERTEX 2014 - 23rd International Workshop on Vertex Detectors, Doksy, Czech Republic, 15 Sep 2014. PoS(Vertex2014)001.

[100] M Capeans, G Darbo, K Einsweiller, M Elsing, T Flick, M Garcia-Sciveres, C Gemme, H Pernegger, O Rohne, and R Vuillermet. ATLAS Insertable B-Layer Technical Design Report. Technical report, 2010. URL https://cds.cern.ch/record/1291633.

[101] ATLAS Collaboration. Production and integration of the ATLAS insertable b-layer. *Journal of Instrumentation*, 13(05):T05008–T05008, may 2018. doi: 10.1088/1748-0221/13/05/t05008. URL https://doi.org/10.1088%2F1748-0221%2F13%2F05%2Ft05008.

[102] The ATLAS collaboration. Operation and performance of the ATLAS semiconductor tracker. *Journal of Instrumentation*, 9(08):P08009–P08009, aug 2014. doi: 10.1088/1748-0221/9/08/p08009. URL https://doi.org/10.1088%2F1748-0221%2F9%2F08%2Fp08009.

[103] ATLAS Collaboration. The Silicon Microstrip Sensors of the ATLAS SemiConductor Tracker. Technical Report 1, CERN, Geneva, 2007. URL https://cds.cern.ch/record/1019885.

[104] ATLAS Collaboration. Performance of the ATLAS transition radiation tracker in run 1 of the LHC: tracker properties. *Journal of Instrumentation*, 12(05):P05002–P05002, may 2017. doi: 10.1088/1748-0221/12/05/p05002. URL https://doi.org/10.1088%2F1748-0221%2F12%2F05%2Fp05002.

[105] The ATLAS Collaboration. TRT performance results from 13 TeV collision data. https://atlas.web.cern.ch/Atlas/GROUPS/PHYSICS/PLOTS/TRT-2016-001/. Accessed: 2021-03-25.

[106] *ATLAS magnet system: Technical Design Report, 1*. Technical design report. ATLAS. CERN, Geneva, 1997. doi: 10.17181/CERN.9O5C.VDTM. URL https://cds.cern.ch/record/338080.

[107] Joao Pequenao. Computer Generated image of the ATLAS calorimeter. 2008. URL https://cds.cern.ch/record/1095927.

[108] *ATLAS liquid-argon calorimeter: Technical Design Report*. Technical design report. ATLAS. CERN, Geneva, 1996. doi: 10.17181/CERN.FWRW.FOOQ. URL https://cds.cern.ch/record/331061.

[109] Nikiforos Nikiforou. Performance of the ATLAS Liquid Argon Calorimeter after three years of LHC operation and plans for a future upgrade, 2013.

[110] Ana Maria Henriques Correia. The ATLAS Tile Calorimeter. Technical Report ATL-TILECAL-PROC-2015-002, CERN, Geneva, Mar 2015. URL https://cds.cern.ch/record/2004868.

[111] *ATLAS muon spectrometer: Technical Design Report*. Technical design report. ATLAS. CERN, Geneva, 1997. URL https://cds.cern.ch/record/331068.

[112] L Pontecorvo. The ATLAS Muon Spectrometer. 2004. doi: 10.1140/epjcd/s2004-04-013-y. URL https://cds.cern.ch/record/676896. revised version number 1 submitted on 2003-07-27 16:31:16.

[113] ATLAS Collaboration. Performance of the ATLAS muon trigger in pp collisions at $\sqrt{s}$ =8 TeV. Performance of the ATLAS muon trigger in pp collisions at $\sqrt{s}$ = 8 TeV. *Eur. Phys. J. C*, C75:120, 2015. doi: 10.1140/epjc/s10052-015-3325-9. URL https://cds.cern.

ch/record/1749694. 19 pages plus author list (34 pages total), 17 figures, 3 tables, submitted to European Physics Journal C, All figures including auxiliary figures are available at http://atlas.web.cern.ch/Atlas/GROUPS/PHYSICS/PAPERS/TRIG-2012-03.

[114] The ATLAS collaboration. Operation of the ATLAS trigger system in Run 2. *Journal of Instrumentation*, 15(10):P10004–P10004, Oct 2020. ISSN 1748-0221. doi: 10.1088/1748-0221/15/10/p10004. URL http://dx.doi.org/10.1088/1748-0221/15/10/P10004.

[115] ATLAS Collaboration. Performance of the ATLAS trigger system in 2015. *Eur. Phys. J. C*, 77:317, 2017. doi: 10.1140/epjc/s10052-017-4852-3.

[116] The ATLAS collaboration. The atlas level-1 calorimeter trigger. *Journal of Instrumentation*, 3(03):P03001, mar 2008. doi: 10.1088/1748-0221/3/03/P03001. URL https://dx.doi.org/10.1088/1748-0221/3/03/P03001.

[117] ATLAS Collaboration. Performance of the ATLAS muon trigger in pp collisions at $\sqrt{s} =$ 8 TeV. *Eur. Phys. J. C*, 75:120, 2015. doi: 10.1140/epjc/s10052-015-3325-9.

[118] ATLAS Collaboration. Topological cell clustering in the ATLAS calorimeters and its performance in LHC Run 1. *Eur. Phys. J. C*, 77:490, 2017. doi: 10.1140/epjc/s10052-017-5004-5.

[119] Wheels in motion for atlas upgrade. https://cerncourier.com/a/wheels-in-motion-for-atlas-upgrade/.

[120] T Kawamoto, S Vlachos, L Pontecorvo, J Dubbert, G Mikenberg, P Iengo, C Dallapiccola, C Amelung, L Levinson, R Richter, and D Lellouch. New Small Wheel Technical Design Report. Technical report, 2013. URL https://cds.cern.ch/record/1552862. ATLAS New Small Wheel Technical Design Report.

[121] G. Iakovidis, L. Levinson, Y. Afik, C. Alexa, T. Alexopoulos, J. Ameel, D. Amidei, D. Antrim, A. Badea, C. Bakalis, H. Boterenbrood, R.S. Brener, S. Chan, J. Chapman, G. Chatzianastasiou, H. Chen, M.C. Chu, R.M. Coliban, T. Costa de Paiva, G. de Geronimo, R. Edgar, N. Felt, S. Francescato, M. Franklin, T. Geralis, K. Gigliotti, P. Giromini, P. Gkountoumis, I. Grayzman, L. Guan, J. Guimaraes da Costa, L. Han, S. Hou, X. Hu, K. Hu, J. Huth, M. Ivanovici, G. Jin, K. Johns, E. Kajomovitz, G. Kehris, I. Kiskiras, A. Koulouris, E. Kyriakis, A. Lankford, L. Lee, H. Leung, F. Li, Y. Liang, H. Lu, N. Lupu, V. Martinez, S. Martoiu, D. Matakias, I. Mehalev, I. Mesolongitis, P. Miao, G. Mikenberg, L. Moleri, P. Moschovakos, J. Narevicius, J. Oliver, D. Pietreanu, R. Pinkham, E. Politis, V. Polychronakos, S. Popa, M.M. Prapa,

I. Ravinovich, A. Roich, R.A. Rojas Caballero, Y. Rozen, M. Schernau, T. Schwartz, G. Scott, O. Shaked, M. Solis, S. Sun, A. Taffard, S. Tang, Z. Tarem, W. Tse, Y. Tu, A. Tuna, P. Tzanis, S. Tzanos, R. Vari, M. Vasile, A. Vdovin, J. Vermeulen, J. Wang, X. Wang, A. Wang, R. Wang, X. Xiao, L. Yao, C. Yildiz, K. Zachariadou, B. Zhou, J. Zhu, S.U. Zimmermann, and O. Zormpa. The new small wheel electronics. *Journal of Instrumentation*, 18(05):P05012, may 2023. doi: 10.1088/1748-0221/18/05/p05012. URL https://doi.org/10.1088%2F1748-0221%2F18%2F05%2Fp05012.

[122] Status report: Test of micromegas trigger with cosmics in bb5. https://indico.cern.ch/event/1021352/contributions/4286861/attachments/2216276/3752906/20210326_badea_nswgeneral_mmtpcosmics.pdf, .

[123] Mm trigger algorithm. https://indico.cern.ch/event/878092/contributions/3805937/attachments/2011678/3361322/Tuna-2020-03-30-mmtp.pdf, .

[124] Trigger commissioning. https://indico.cern.ch/event/1030130/contributions/4325294/attachments/2238882/3796688/Tuna-2021-04-30-trigger.pdf, .

[125] Update on testing the nsw micromegas trigger processor with cosmics in bb5. https://indico.cern.ch/event/1035055/contributions/4377324/attachments/2254782/3825684/20210531_badea_muon_week_tpcosmics.pdf, .

[126] ATLAS Collaboration. Performance of the ATLAS track reconstruction algorithms in dense environments in LHC Run 2. *Eur. Phys. J. C*, 77:673, 2017. doi: 10.1140/epjc/s10052-017-5225-7.

[127] ATLAS Collaboration. Reconstruction of primary vertices at the ATLAS experiment in Run 1 proton–proton collisions at the LHC. *Eur. Phys. J. C*, 77:332, 2017. doi: 10.1140/epjc/s10052-017-4887-5.

[128] ATLAS Collaboration. Vertex Reconstruction Performance of the ATLAS Detector at $\sqrt{s} = 13$ TeV. ATL-PHYS-PUB-2015-026, 2015. URL https://cds.cern.ch/record/2037717.

[129] ATLAS Collaboration. Electron reconstruction and identification in the ATLAS experiment using the 2015 and 2016 LHC proton–proton collision data at $\sqrt{s} = 13$ TeV. *Eur. Phys. J. C*, 79:639, 2019. doi: 10.1140/epjc/s10052-019-7140-6.

[130] ATLAS Collaboration. Improved electron reconstruction in ATLAS using the Gaussian Sum Filter-based model for bremsstrahlung. ATLAS-CONF-2012-047, 2012. URL https://cds.cern.ch/record/1449796.

[131] ATLAS Collaboration. Electron and photon reconstruction and performance in ATLAS using a dynamical, topological cell clustering-based approach. ATL-PHYS-PUB-2017-022, 2017. URL https://cds.cern.ch/record/2298955.

[132] ATLAS Collaboration. Electron and photon performance measurements with the ATLAS detector using the 2015-2017 LHC proton–proton collision data. 2019.

[133] Studies of the muon momentum calibration and performance of the ATLAS detector with *pp* collisions at $\sqrt{s}$=13 TeV. 12 2022.

[134] ATLAS Collaboration. Measurement of the muon reconstruction performance of the ATLAS detector using 2011 and 2012 LHC proton–proton collision data. *Eur. Phys. J. C*, 74:3130, 2014. doi: 10.1140/epjc/s10052-014-3130-x.

[135] ATLAS Collaboration. Muon reconstruction performance of the ATLAS detector in proton–proton collision data at $\sqrt{s} = 13$ TeV. *Eur. Phys. J. C*, 76:292, 2016. doi: 10.1140/epjc/s10052-016-4120-y.

[136] ATLAS Collaboration. Muon reconstruction and identification efficiency in ATLAS using the full Run 2 *pp* collision data set at $\sqrt{s} = 13$ TeV. *Eur. Phys. J., C*, 81:578, 2021. doi: 10.1140/epjc/s10052-021-09233-2. URL https://cds.cern.ch/record/2746302. 64 pages in total, author list starting page 42, auxiliary material starting at page 59, 34 figures, 3 tables. All figures including auxiliar figures are available at https://atlas.web.cern.ch/Atlas/GROUPS/PHYSICS/PAPERS/MUON-2018-03/.

[137] ATLAS Collaboration. Measurement of the tau lepton reconstruction and identification performance in the ATLAS experiment using *pp* collisions at $\sqrt{s} = 13$ TeV. ATLAS-CONF-2017-029, 2017. URL https://cds.cern.ch/record/2261772.

[138] ATLAS Collaboration. Performance of missing transverse momentum reconstruction with the ATLAS detector using proton–proton collisions at $\sqrt{s} = 13$ TeV. *Eur. Phys. J. C*, 78:903, 2018. doi: 10.1140/epjc/s10052-018-6288-9.

[139] J E Huth, N Wainer, K Meier, N J Hadley, F Aversa, Mario Greco, P Chiappetta, J P Guillet, S Ellis, Zoltán Kunszt, and Davison Eugene Soper. Toward a standardization of jet definitions. 1990. URL https://cds.cern.ch/record/217490.

[140] Simone Marzani, Gregory Soyez, and Michael Spannowsky. *Looking Inside Jets*. Springer International Publishing, 2019. doi: 10.1007/978-3-030-15709-8. URL https://doi.org/10.1007%2F978-3-030-15709-8.

[141] Gavin P Salam and Grégory Soyez. A practical seedless infrared-safe cone jet algorithm. *Journal of High Energy Physics*, 2007(05):086–086, may 2007. doi: 10.1088/1126-6708/2007/05/086. URL https://doi.org/10.1088%2F1126-6708%2F2007%2F05%2F086.

[142] Matteo Cacciari, Gavin P. Salam, and Gregory Soyez. FastJet user manual. *Eur. Phys. J. C*, 72: 1896, 2012. doi: 10.1140/epjc/s10052-012-1896-2.

[143] Gavin P. Salam. Towards jetography. *The European Physical Journal C*, 67(3-4):637–686, may 2010. doi: 10.1140/epjc/s10052-010-1314-6. URL https://doi.org/10.1140%2Fepjc%2Fs10052-010-1314-6.

[144] S. Catani, Yuri L. Dokshitzer, M. H. Seymour, and B. R. Webber. Longitudinally invariant K_t clustering algorithms for hadron hadron collisions. *Nucl. Phys. B*, 406:187–224, 1993. doi: 10.1016/0550-3213(93)90166-M.

[145] Stephen D. Ellis and Davison E. Soper. Successive combination jet algorithm for hadron collisions. *Phys. Rev. D*, 48:3160–3166, Oct 1993. doi: 10.1103/PhysRevD.48.3160. URL https://link.aps.org/doi/10.1103/PhysRevD.48.3160.

[146] Yu.L Dokshitzer, G.D Leder, S Moretti, and B.R Webber. Better jet clustering algorithms. *Journal of High Energy Physics*, 1997(08):001–001, aug 1997. doi: 10.1088/1126-6708/1997/08/001. URL https://doi.org/10.1088%2F1126-6708%2F1997%2F08%2F001.

[147] Matteo Cacciari, Gavin P. Salam, and Gregory Soyez. The anti-k_t jet clustering algorithm. *JHEP*, 04:063, 2008. doi: 10.1088/1126-6708/2008/04/063.

[148] Matteo Cacciari. FastJet: A Code for fast k_t clustering, and more. In *Proceedings, Deep inelastic scattering, 14th International Workshop, DIS 2006*, pages 487–490.

[149] ATLAS Collaboration. Jet reconstruction and performance using particle flow with the ATLAS Detector. *Eur. Phys. J. C*, 77:466, 2017. doi: 10.1140/epjc/s10052-017-5031-2.

[150] Georges Aad et al. Jet energy scale and resolution measured in proton–proton collisions at $\sqrt{s} = 13$ TeV with the ATLAS detector. *Eur. Phys. J. C*, 81(8):689, 2021. doi: 10.1140/epjc/s10052-021-09402-3.

[151] Luminosity determination in pp collisions at $\sqrt{s} = 13$ TeV using the ATLAS detector at the LHC. Technical report, CERN, Geneva, 2022. URL https://cds.cern.ch/record/2844887. 74 pages in total, 36 figures, 10 tables, submitted to EPJC. All figures including auxiliary figures are available at https://atlas.web.cern.ch/Atlas/GROUPS/PHYSICS/PAPERS/DAPR-2021-01.

[152] Johan Alwall, Michel Herquet, Fabio Maltoni, Olivier Mattelaer, and Tim Stelzer. MadGraph 5 : Going Beyond. *JHEP*, 06:128, 2011. doi: 10.1007/JHEP06(2011)128.

[153] J. Alwall, R. Frederix, S. Frixione, V. Hirschi, F. Maltoni, O. Mattelaer, H. S. Shao, T. Stelzer, P. Torrielli, and M. Zaro. The automated computation of tree-level and next-to-leading order differential cross sections, and their matching to parton shower simulations. *JHEP*, 07:079, 2014. doi: 10.1007/JHEP07(2014)079.

[154] Benjamin Fuks. Beyond the Minimal Supersymmetric Standard Model: from theory to phenomenology. *Int. J. Mod. Phys. A*, 27:1230007, 2012. doi: 10.1142/S0217751X12300074.

[155] S. Mrenna and P. Skands. Automated parton-shower variations in PYTHIA 8. *Phys. Rev. D*, 94:074005, 2016. doi: 10.1103/PhysRevD.94.074005.

[156] Peter Skands, Stefano Carrazza, and Juan Rojo. Tuning PYTHIA 8.1: the Monash 2013 Tune. *Eur. Phys. J. C*, 74(8):3024, 2014. doi: 10.1140/epjc/s10052-014-3024-y.

[157] Richard D. Ball et al. Parton distributions with LHC data. *Nucl. Phys. B*, 867:244, 2013. doi: 10.1016/j.nuclphysb.2012.10.003.

[158] D. J. Lange. The EvtGen particle decay simulation package. *Nucl. Instrum. Meth. A*, 462:152, 2001. doi: 10.1016/S0168-9002(01)00089-4.

[159] GEANT4 Collaboration, S. Agostinelli, et al. GEANT4 – a simulation toolkit. *Nucl. Instrum. Meth. A*, 506:250, 2003. doi: 10.1016/S0168-9002(03)01368-8.

[160] A. Ribon et al. Status of geant4 hadronic physics for the simulation of LHC experiments at the start of the LHC physics program. 2010. URL https://lcgapp.cern.ch/project/docs/noteStatusHadronic2010.pdf.

[161] Atlas susy crosssections 13tev gluglu nnlo approx and nnll. https://twiki.cern.ch/twiki/bin/view/LHCPhysics/SUSYCrossSections13TeVgluglu#NNLOapprox_NNLL.

[162] Christoph Borschensky, Michael Krämer, Anna Kulesza, Michelangelo Mangano, Sanjay Padhi, Tilman Plehn, and Xavier Portell. Squark and gluino production cross sections in $$pp$$ p p collisions at $$\sqrt{s} = 13, 14, 33$$ s = 13 , 14 , 33 and $$100$$ 100 TeV. *The European Physical Journal C*, 74(12), dec 2014. doi: 10.1140/epjc/s10052-014-3174-y. URL https://doi.org/10.1140%2Fepjc%2Fs10052-014-3174-y.

[163] Torbjörn Sjöstrand, Stefan Ask, Jesper R. Christiansen, Richard Corke, Nishita Desai, Philip Ilten, Stephen Mrenna, Stefan Prestel, Christine O. Rasmussen, and Peter Z. Skands. An introduction to PYTHIA 8.2. *Comput. Phys. Commun.*, 191:159–177, 2015. doi: 10.1016/j.cpc.2015.01.024.

[164] ATLAS Collaboration. ATLAS Pythia 8 tunes to 7 TeV data. ATL-PHYS-PUB-2014-021, 2014. URL https://cds.cern.ch/record/1966419.

[165] Bo Andersson, G. Gustafson, G. Ingelman, and T. Sjöstrand. Parton fragmentation and string dynamics. *Phys. Rept.*, 97:31–145, 1983. doi: 10.1016/0370-1573(83)90080-7.

[166] Torbjorn Sjöstrand. Jet fragmentation of multiparton configurations in a string framework. *Nucl. Phys. B*, 248:469–502, 1984. doi: 10.1016/0550-3213(84)90607-2.

[167] ATLAS Collaboration. Performance of pile-up mitigation techniques for jets in pp collisions at $\sqrt{s} = 8$ TeV using the ATLAS detector. *Eur. Phys. J. C*, 76:581, 2016. doi: 10.1140/epjc/s10052-016-4395-z.

[168] ATLAS Collaboration. Identification and energy calibration of hadronically decaying tau leptons with the ATLAS experiment in pp collisions at $\sqrt{s} = 8$ TeV. *Eur. Phys. J. C*, 75:303, 2015. doi: 10.1140/epjc/s10052-015-3500-z.

[169] Georges Aad et al. Measurement of hadronic event shapes in high-p_T multijet final states at $\sqrt{s} = 13$ TeV with the ATLAS detector. *JHEP*, 01:188, 2021. doi: 10.1007/JHEP01(2021)188. [Erratum: JHEP 12, 053 (2021)].

[170] ATLAS Collaboration. Search for pair production of massive particles decaying into three quarks with the ATLAS detector in $\sqrt{s} = 7$ TeV pp collisions at the LHC. *JHEP*, 12:086, 2012. doi: 10.1007/JHEP12(2012)086.

[171] ATLAS Collaboration. Search for massive supersymmetric particles decaying to many jets using the ATLAS detector in pp collisions at $\sqrt{s} = 8$ TeV. *Phys. Rev. D*, 91:112016, 2015. doi: 10.1103/PhysRevD.91.112016.

[172] Robert D. Cousins, James T. Linnemann, and Jordan Tucker. Evaluation of three methods for calculating statistical significance when incorporating a systematic uncertainty into a test of the background-only hypothesis for a Poisson process. *Nucl. Instrum. Meth. A*, 595(2):480, 2008. doi: 10.1016/j.nima.2008.07.086.

[173] Lukas Heinrich, Matthew Feickert, and Giordon Stark. pyhf: v0.7.2. URL `https://doi.org/10.5281/zenodo.1169739`. https://github.com/scikit-hep/pyhf/releases/tag/v0.7.2.

[174] Lukas Heinrich, Matthew Feickert, Giordon Stark, and Kyle Cranmer. pyhf: pure-python implementation of histfactory statistical models. *Journal of Open Source Software*, 6(58):2823, 2021. doi: 10.21105/joss.02823. URL `https://doi.org/10.21105/joss.02823`.

[175] Albert M. Sirunyan et al. Search for pair-produced resonances each decaying into at least four quarks in proton-proton collisions at $\sqrt{s} = 13$ TeV. *Phys. Rev. Lett.*, 121(14):141802, 2018. doi: 10.1103/PhysRevLett.121.141802.

[176] Albert M. Sirunyan et al. Search for pair-produced resonances decaying to quark pairs in proton-proton collisions at $\sqrt{s} = 13$ TeV. *Phys. Rev. D*, 98(11):112014, 2018. doi: 10.1103/PhysRevD.98.112014.

[177] Albert M Sirunyan et al. Search for pair-produced three-jet resonances in proton-proton collisions at $\sqrt{s}$ =13 TeV. *Phys. Rev. D*, 99(1):012010, 2019. doi: 10.1103/PhysRevD.99.012010.

[178] Georges Aad et al. Search for new resonances in mass distributions of jet pairs using 139 fb^{-1} of pp collisions at $\sqrt{s} = 13$ TeV with the ATLAS detector. *JHEP*, 03:145, 2020. doi: 10.1007/JHEP03(2020)145.

[179] Morad Aaboud et al. A search for pair-produced resonances in four-jet final states at $\sqrt{s} =$ 13 TeV with the ATLAS detector. *Eur. Phys. J. C*, 78(3):250, 2018. doi: 10.1140/epjc/s10052-018-5693-4.

[180] Georges Aad et al. Search for massive supersymmetric particles decaying to many jets using the ATLAS detector in pp collisions at $\sqrt{s} = 8$ TeV. *Phys. Rev. D*, 91(11):112016, 2015. doi: 10.1103/PhysRevD.91.112016. [Erratum: Phys. Rev. D 93, 039901 (2016)].

[181] Morad Aaboud et al. Search for R-parity-violating supersymmetric particles in multi-jet final states produced in p-p collisions at $\sqrt{s} = 13$ TeV using the ATLAS detector at the LHC. *Phys. Lett. B*, 785:136–158, 2018. doi: 10.1016/j.physletb.2018.08.021.

[182] Alexander Shmakov, Michael James Fenton, Ta-Wei Ho, Shih-Chieh Hsu, Daniel Whiteson, and Pierre Baldi. SPANet: Generalized permutationless set assignment for particle physics using symmetry preserving attention. *SciPost Phys.*, 12:178, 2022. doi: 10.21468/SciPostPhys.12.5.178. URL https://scipost.org/10.21468/SciPostPhys.12.5.178.

[183] Shikai Qiu, Shuo Han, Xiangyang Ju, Benjamin Nachman, and Haichen Wang. A holistic approach to predicting top quark kinematic properties with the covariant particle transformer, 2023.

[184] Lukas Ehrke, John Andrew Raine, Knut Zoch, Manuel Guth, and Tobias Golling. Topological reconstruction of particle physics processes using graph neural networks, 2023.

[185] Anthony Badea, William James Fawcett, John Huth, Teng Jian Khoo, Riccardo Poggi, and Lawrence Lee. Solving combinatorial problems at particle colliders using machine learning. *Phys. Rev. D*, 106:016001, Jul 2022. doi: 10.1103/PhysRevD.106.016001. URL https://link.aps.org/doi/10.1103/PhysRevD.106.016001.

[186] Ashish Vaswani, Noam Shazeer, Niki Parmar, Jakob Uszkoreit, Llion Jones, Aidan N. Gomez, Lukasz Kaiser, and Illia Polosukhin. Attention is all you need, 2017.

[187] Alec Radford and Karthik Narasimhan. Improving language understanding by generative pre-training. 2018.

[188] DeepMind. Highly accurate protein structure prediction with alphafold. *Nature*, 596 (7873):583–589, 2021. doi: 10.1038/s41586-021-03819-2. URL https://doi.org/10.1038/s41586-021-03819-2.

[189] Adam Paszke, Sam Gross, Francisco Massa, Adam Lerer, James Bradbury, Gregory Chanan, Trevor Killeen, Zeming Lin, Natalia Gimelshein, Luca Antiga, Alban Desmaison, Andreas Köpf, Edward Yang, Zach DeVito, Martin Raison, Alykhan Tejani, Sasank Chilamkurthy, Benoit Steiner, Lu Fang, Junjie Bai, and Soumith Chintala. Pytorch: An imperative style, high-performance deep learning library, 2019.

[190] Jimmy Lei Ba, Jamie Ryan Kiros, and Geoffrey E. Hinton. Layer normalization, 2016.

[191] John Nickolls, Ian Buck, Michael Garland, and Kevin Skadron. Scalable parallel programming with cuda. *Queue*, 6:40–53, 03 2008. doi: 10.1145/1401132.1401152.

[192] William Falcon and The PyTorch Lightning team. PyTorch Lightning, mar 2019. URL https://github.com/Lightning-AI/lightning.

[193] Max Jaderberg, Valentin Dalibard, Simon Osindero, Wojciech M. Czarnecki, Jeff Donahue, Ali Razavi, Oriol Vinyals, Tim Green, Iain Dunning, Karen Simonyan, Chrisantha Fernando, and Koray Kavukcuoglu. Population based training of neural networks, 2017.

[194] Richard Liaw, Eric Liang, Robert Nishihara, Philipp Moritz, Joseph E Gonzalez, and Ion Stoica. Tune: A research platform for distributed model selection and training. *arXiv preprint arXiv:1807.05118*, 2018.

[195] ATLAS Collaboration. Atlas flavour-tagging algorithms for the lhc run 2 *pp* collision dataset, 2022.

[196] Glen Cowan, Kyle Cranmer, Eilam Gross, and Ofer Vitells. Asymptotic formulae for likelihood-based tests of new physics. *Eur. Phys. J. C*, 71:1554, 2011. doi: 10.1140/epjc/s10052-011-1554-0.

[197] Alexander L. Read. Presentation of search results: the CL_S technique. *J. Phys. G*, 28:2693, 2002. doi: 10.1088/0954-3899/28/10/313.